Modelling of a Flexible Inflatable Floater

Analysis of the stiffness behaviour of a drop-stitch panel for offshore floating photovoltaics

Cas van Engelen
04-03-2022
Master's thesis

TUDelft

TNO
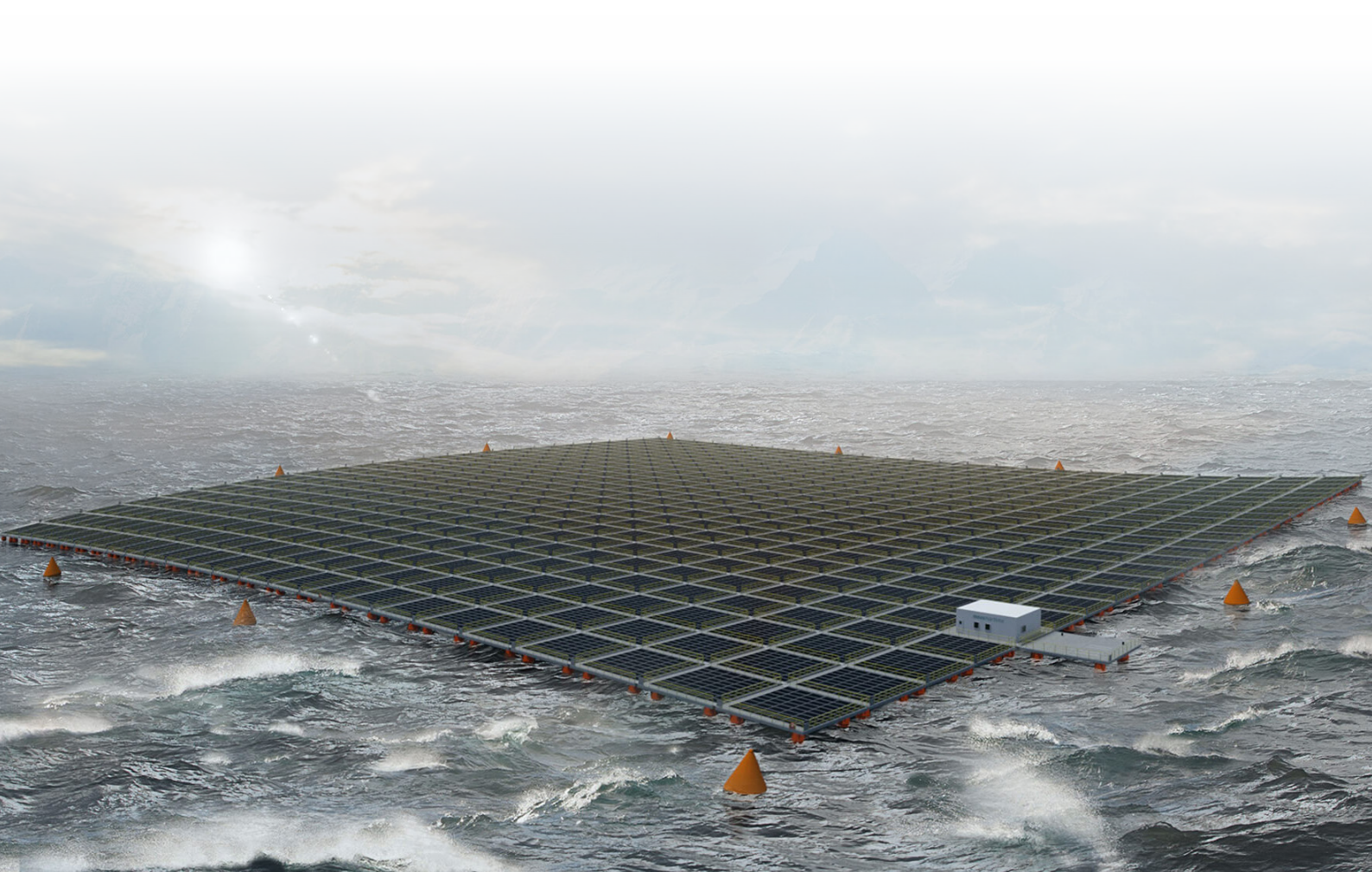
Thesis for the degree of MSc in Marine Technology in the
specialisation of Ship and Offshore Structures

Modelling of a Flexible Inflatable Floater

Analysis of the stiffness behaviour of a drop-stitch panel for offshore floating photovoltaics

By
Cas van Engelen

Performed at
TNO

Date of exam: March 11, 2022

*This thesis (**MT.21/22.021.M.**) is classified as confidential in accordance with the general conditions for projects performed by the TU Delft.*

March 4, 2022

Company supervisors
Responsible supervisor: Ir. A. J. W. van den Brink

Other supervisor: Ir. M. G. Hoogeland

Thesis exam committee
Chair/Responsible professor: Dr. ir. L. Pahlavan
Staff member: H. M. Verhelst, MSc.
Staff member: Dr. C. L. Walters
Staff member: Dr. A. Grammatikopoulos
Company member: Ir. A. J. W. van den Brink
Company member: Ir. M. G. Hoogeland

Author details
Student number: 4465008

The cover page shows a render made by Saipem of an offshore floating photovoltaics, which clearly depicts the rough sea conditions floating photovoltaics should be able to withstand. Image from Saipem [1].

Preface

This thesis on "Modelling of a Flexible Inflatable Floater" has been written for obtaining the master's degree in Marine Technology with the specialisation of Ship and Offshore Structures at the University of Technology Delft in corporation with TNO. The research was performed under supervision of Dr. ir. L. Pahlavan (TU Delft), H. M. Verhelst, MSc. (TU Delft), Ir. A. J. W. van den Brink (TNO) and Ir. M. G. Hoogeland (TNO).

The question TNO imposed to me was quite clear from the beginning:" Investigate and model the essential and relevant aspects of the mechanical behaviour of a drop-stitch floater". Easy as it sounds, I confidently thought:" I just have to model an inflatable panel and analyse the results of that model. This should not be too complicated." It appeared to be more difficult and time consuming than I expected. I have learned a lot during my thesis, especially about FEM modelling.

First and foremost, I would like to thank my supervisors: Pooria, Hugo, Arjan and Martijn. Pooria, I have enjoyed your courses especially about composite materials in maritime structures. It taught me the basics of composite materials, which will be useful for the rest of my engineering career. Hugo, your enthusiasm and knowledge really helped to finalise my master's thesis. You have learned me the basics of wrinkling and also helped me with the theoretical background of FEM. Arjan, you have helped me to step out of the level of details and get a clear picture of what I had done and was working on. This helped me to communicate and present my Master's thesis to others and organise my thoughts. Martijn, I want to thank you for the feedback you gave me throughout my graduation.

Besides my supervisors, I would like to thank Heytex for providing the material of the drop-stitch panels, which is used to perform the uniaxial tensile tests. Additionally, I would like to thank Andre van den Bosch for helping me performing the uniaxial tensile tests. Furthermore, I enjoyed the weekly meetings with the SHM group. Those weekly meetings helped me to get a clear view on what I have had done every week and get a look into other interesting researches mainly focused on structural health monitoring. Also, I would like to thank the Solar@Sea II consortium partners. The Solar@Sea II project is the origin of this master's thesis. I really like the usage of a more unconventional type of offshore structure. My study, Marine Technology, is mostly focused on steel offshore structures, so modelling a flexible inflatable floater made of a polyester fiber coated with PVC was very interesting. Also, I want to thank everyone of TNO with whom I have had interesting conversations about structure related and unrelated topics.

I want to thank my family, girlfriend, friends and roommates for their support and providing breaks to relax. Lastly, I would like to thank my study association S.G. "William Froude" for providing maritime related lectures, excursions and study trips. This created a general interest in the maritime industry.

<div align="right">

C. van Engelen
Delft, February 15, 2022

</div>

Contents

Abstract

Over the past decades, a transition has taken place from fossil fuel towards renewable energy to mitigate the green house gasses and eventually the global warming effect. One type of renewable energy source is solar energy. The conversion of solar energy into electricity is called photovoltaics. Currently, floating photovoltaics (FPVs) generate more interest. For FPVs, an uncommon type of offshore structure is considered, which is very flexible and deforms with the motion of the waves. In this research, the bending characteristics of an drop-stitch floater is analysed, which is an inflatable panel. By inflating the drop-stitch floater to a low air pressure, it obtains a flattened shape and the ability to support the flexible solar panels, while still retaining flexibility to deform with the motion of the waves.

The bending characteristics of a drop-stitch floater are more complex than common offshore structures due to different non-linearities: wrinkling, hyperelastic material behaviour and internal pressure-volume work. Getting a better understanding in the bending response is important to eventually determine the response and limit states in offshore conditions. Most research into drop-stitch panels has been focusing on high pressurised panels. Research into the failure modes of drop-stitch panels has not been conducted yet. In this thesis, an evaluation of the bending characteristics and failure modes has been conducted.

A finite element (FE) model has been developed in ABAQUS to analyse the structural response in a three point bending load case. The effect of wrinkling is incorporated with a perturbation method. The internal air pressure creates an initial deflection, which is sufficient to incorporate wrinkling effects in combination with a fine mesh. The internal air volume is modelled as an ideal gas using a surface based fluid cavity to take into account the pressure-volume work. An uniaxial tensile test with the strip method has been conducted to analyse the material behaviour. The experimental results has been used to fit different material models. The results of the FE model has been compared with a three point bending experiment. Also, a parametric analysis with different yarn distances, face sheet thicknesses and internal air pressures has been analysed. Two FE models are established: a quarter model, which models only a quarter of the drop-stitch panel, and a strip model, which does not include the edges and has the width of one yarn spacing. Good agreement has been found between both models, which suggests that simplifying the drop-stitch panel to a strip suffices for uniaxial load cases.

The polyester fiber coated with PVC was shown the be an orthotropic hyperelastic material. A linear elastic orthotropic, Holzapfel-Gasser-Ogden and Fung orthotropic material model has been fitted. The different material models do have effect on the response of the drop-stitch panel. It appeared to be difficult to describe the hyperelastic orthotropic material behaviour exactly, but it has shown to have little influence on the global response.

Two different failure modes are observed: a local folding and global wrinkling failure mode. For low internal air pressures, small yarn distance and large face sheet thickness the local folding mode is initiated and the global wrinkling mode for high internal air pressures, large yarn distance and small face sheet thickness. This suggests that the bending stiffness in the face sheets and internal air pressure is significant for the failure mode initiation and propagation.

List of Abbreviations

ALS	Accidental Limit State
CLT	Classical Laminate Theory
DoF	Degrees of Freedom
DWF	Double Woven Fabric
FE	Finite Elements
FEA	Finite Element Analysis
FEM	Finite Element Method
FLS	Fatigue Limit State
FO	Fung Orthotropic
FPV	Floating Photovoltaic
GHG	Greenhouse Gasses
HGO	Holzapfel-Gasser-Ogden
IPCC	Intergovernmental Panel on Climate Change
LEO1	Linear Elastic Orthotropic material model 1
LEO2	Linear Elastic Orthotropic material model 1
PV	Photovoltaic
PVC	Polyvinyl Chloride
RE	Renewable Energy
SLS	Serviceability Limit State
ULS	Ultimate Limit State

Chapter 1

Introduction

Since the industrial revolution, the climate has changed rapidly due to global warming. It is essential to limit the global warming to ensure a bright and prosper future for the next generations. The Intergovernmental Panel on Climate Change (IPCC) is a panel of the United Nations, who is working on science related strategies to mitigate global warming [2, 3]. They have shown that the warming of the climate system is unequivocal based on observations. The energy transition to clean and renewable energy (RE) is one of the key elements to reduce the greenhouse gas emissions (GHG) and eventually the global warming. Consequently, there is a huge demand for research and innovative solution to make this transition possible. Different mitigation pathways have been investigated to get to a global warming of 1.5°C pre-industrial level, which is the preferred limit set by the Paris Agreement [4]. These mitigation pathways of the IPCC showed that the share of primary energy sources from renewables should increase in the upcoming years tremendously to reach this global warming limit goal [5]. The parties who have agreed on the Paris Agreement shall aim to limit the global warming to 2°C and preferably to 1.5°C pre-industrial level by 2050. Some parties such as the Netherlands even set more ambitious goals. The Dutch Climate Act aims to have 100% RE and 95% less CO_2 emission by 2050, hence research and innovation is needed to reach these goals. So, it is of utter importance to make this increase of RE sources possible [6].

Bio energy, direct solar energy, geothermal energy, hydro power, ocean energy and wind energy are considered as RE sources [7]. There are multiple benefits of RE besides the decrement of GHG emissions such as: RE is a resource sufficient energy supply, so it creates energy security; The decrement of air pollution is good for health, wildlife, landscape and the ecosystem; It has a positive local employment impact [7]. There is no specific dominant RE source, so a mix of RE developments should be investigated which suits local areas. IPCC considered solar energy as one of the primary RE source, which has the highest technical potential. The technical potential is defined as "the amount of RE output obtainable by full implementation of demonstrated technologies or practices" [7]. Even though, there are some concerns which could limit the technical potential such as the availability of critical metals, it is a topic of high interest for research and is a key element in reaching a global warming limit of 1.5°C pre-industrial level by 2050.
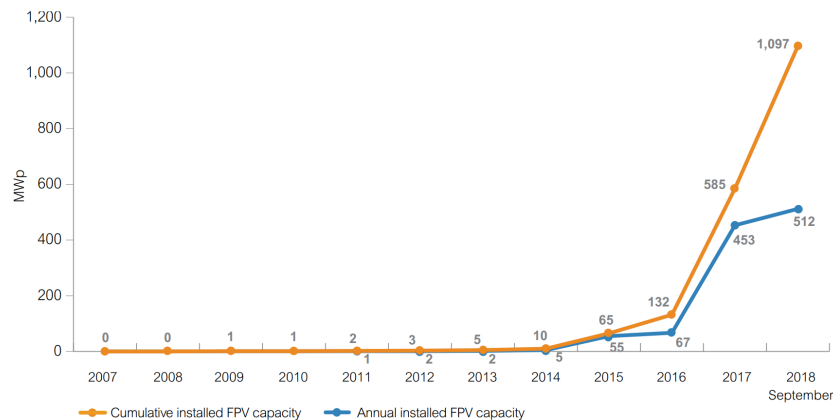
Figure 1.1: Global installed FPV capacity between 2007 and 2018 [8]

Photovoltaics (PV) on land have intense land requirements [9]. Especially in densely populated countries such as the Netherlands, land is scarce and expensive, so offshore floating solar panels is very promising. According to DNV, an offshore floating PV (FPV) energy farm in the North Sea may produce 10GW in 2050, which could potentially supply 10 million households with electricity [10]. Combined with aquatic biomass and wind energy, an energy farm in the North Sea may even reach 22GW. Nowadays, that may still sound like science fiction, but recent efforts by industry leaders have greatly reduced the costs and increased the efficiency and knowledge of PVs [11]. Figure 1.1 clearly shows the increased capacity of FPVs, which are mostly inshore, between 2007 and 2018 [8]. Golroodbari et al. analysed the average annual output energy of PVs at land and sea and showed that the PV at sea have significantly higher energy output than at land due to natural cooling [12]. Also, FPVs and offshore wind are highly complementary [13]. Between offshore wind turbines, there are large open spaces, at which vessels are not allowed to sail. Therefore, it is an ideal location for offshore FPVs. In the summer months, the solar irradiation is higher and the average wind speed is lower, so more solar energy will be produced and less wind energy. In contrary to the summer months, the winter months generally have a higher average wind speed and lower solar irradiation, so more wind energy and less solar energy will be produced. Throughout a year, the RE production will be more stable, if solar and wind energy are combined into one energy farm. The positive and negative impact of FPVs on ecosystems is currently being investigated [14]. Early studies showed that the effect of light deficit on plankton production is negligible [15] and increase water quality by reducing algal blooms and evaporation rate [9, 16].

Recently, multiple large and small scale floating solar farms have been deployed [18–21]. Especially Japan, China and South-Korea are currently leading regarding the amount of MW produced by FPVs. In 2020, a disaster struck at the largest FPV installation of Japan at the Yamakura Dam [22], shown before the accident in figure 1.2. Due to a typhoon, a few mooring lines failed, which caused an uplift of the floaters caused by the wind and the FPVs collapsed. Consequently, an electrical fire occurred and about two third of the solar farm at the Yamakura Dam was damaged. This event showed that floating solar farms are vulnerable and the structural mechanics should be investigated to guarantee the safety of FPVs.

Figure 1.2: A photograph after the completion of the floating solar power plant at the Yamakura Dam, Japan [17]

1.1 Motivation

In the project consortium Solar@Sea II, a detailed design of a flexible inflatable floating configuration is developed to carry PVs [23], figure 1.4. It aims to raise the technology readiness up to the proof of concept for a solar energy farm. The solar energy farm will consist of several FPVs that are partly built onshore, transported to an offshore environment and interconnected with a mooring system. In cooperation with TNO, a structural analysis of the floaters, which carry the flexible PVs, is performed in this thesis. The floaters are made out of drop-stitch panels. To the best of the author's knowledge, limited research has been performed into the stiffness behaviour and finite element analysis (FEA) of low pressurised drop-stitch panels. The internal air pressure of the drop-stitch panel significantly contributes to the bending stiffness. A low internal air pressure and flexible solar panels, result in a flexible drop-stitch panel, which is one of the aims of the Solar@Sea II project.

Figure 1.3: An example of a polyester drop-stitch fabric with coated rubber skins [24]

A drop-stitch panel consist of two cloths made out of double woven fabric coated with PVC, which are connected with vertical threads, figure 1.3. Between those two cloths an internal air pressure is created to obtain bending stiffness. Due to the vertical threads, the panel will maintain its flat shape. These panels have already been used for different applications as shown in figure 1.5. One of the benefits of drop-stitch panels is that if one deflates them, it is possible transport them compactly. So, one can produce them onshore and transport them to offshore/inshore/nearshore. The World Bank Group subdivided [25] FPVs into three applications: above water, on water, and submerged. The FPV of the Solar@Sea II project will be an "above water" application. The "above water" application is currently more common, since "above water" applications such as pontoons are easier to manufacture and maintain than the others. MARIN showed in a preliminary study that the second order wave force decreases for a flexible floater compared to a rigid floater [26]. The second order wave force is a dominant component of the wave loads and has major contribution to the mooring loads. Also, the uplift on the floaters created by wind tends to be lower if the floaters deform with the waves. If the characteristic length of a structure is much smaller than the dominant wave length, the structure can be considered a very flexible floating structure. These type of structures have stronger hydro-elastic interaction between the waves and structure, which has the advantage of transforming wave energy into kinetic and potential energy instead of slamming against a more rigid structure [27]. Assuming a linear bending stiffness would be insufficient at large deformations, since the bending response is non-linear due to different structural aspects: hyperelastic material stiffness properties; wrinkling; the internal air pressure, which exerts a pressure normal to the internal surface; axial forces becoming more dominant at high deflections [24].

Figure 1.4: A photograph of the drop-stitch floaters of the Solar@Sea II project (courtesy of TNO).

(a) An airtrack, which is a low pressure and flexible drop-stitch panel [28]
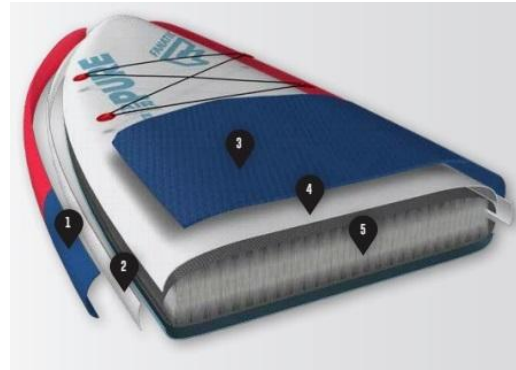
(b) A transverse cross section of a stand up paddling board, which is a high pressure and stiff drop-stitch panel [29]

Figure 1.5: Examples of applications of flexible and stiff drop-stitch panels

1.2 Goal

More insight in the non-linear bending behaviour is needed to properly model the structural response drop-stitch floaters. This research has been performed to get more insight in the bending stiffness and modelling of a flexible drop-stitch panel using FEA and experiments.

To the best of the author's knowledge, there is limited research performed into flexible low pressure drop-stitch panels. Recommendations on the design, development and operation of FPVs have been developed by DNV [30]. DNV considers multiple environmental and site conditions which should be taken into account for FPVs: wind, waves, currents, snow and ice accreation, fouling, ecology et cetera. In their report, they consider inshore/near-shore, high stiffness and linear elastic floaters, so this could be inadequate for drop-stitch floaters in offshore environment. Previous research on drop-stitch panels has performed a modal analysis and four point bending test of a high pressurised drop-stitch panel using an experimental and FEA [24, 31, 32]. For the numerical four point bending test, Davids et al. have considered the drop-stitch panel as a beam. The non-linear approach of Davids et al. has good aggreement between the experiments and numerical model [32]. The numerical modal analysis performed by Hulton et al. has been performed with a 3D FEA [31]. However, the documentation on how to numerically model a drop-stitch panel using a 3D finite element model is limited. Also, the internal air pressure range used in most research is significantly higher compared to what is desired for the application of flexible floaters. The analytical approach of Cavallaro [24] assumes a linear force-deflection relationship and did not take the decay of the bending stiffness into account due to wrinkling. Research into the failure mechanism of drop-stitch panels has not yet been performed.

Getting insight in the bending response is important to eventually determine the limit states of the floater in offshore condition and failure mechanism. Waves will introduce a pressure distribution on the floater, which will among other things bend the floater. For the offshore application of FPVs, the bending characteristics are highly important to evaluate the response due to waves.

The goal of this research is to get more insight in the bending characteristics of low pressurised drop-stitch panels.

1.3 Research questions & Scope

From the goal and knowledge gap, the main research questions are formulated. The main research questions is defined as:

What are the bending characteristics of low pressurised drop-stitch panels using an FEA and experimental analysis?

Only quasi-static bending load cases are considered in this thesis. This means that the kinetic energy is minimised and velocities should be close to zero. A dynamic, buckling and modal analyses are not considered. To answer the main question, different sub-questions are addressed:

1. **How could a drop-stitch panel be modelled using 3D FEM?**

   Drop-stitch panels are complex to model due to its non-linear stiffness behaviour mentioned in section 1.1. The assumptions made during the modelling of a drop-stitch panel could have significant influence on the results of a model and should be handled with care. To develop a proper FE model, several aspects should be investigated using literature and experiments to support the assumptions. A material model should be implemented in the FE model to correctly describe the stress-strain behaviour of the yarns and fabric, shown in figure 1.3. This stress-strain behaviour will be evaluated using experiments. The FE model should also include the influence of wrinkling, since this is expected to be significant. Due to volume changes inside the drop-stitch panel, the internal air pressure changes, which could also influence the bending stiffness and should be evaluated.

2. **What is the influence of internal air pressure, thickness of the face sheet and yarn distance on the bending and wrinkling response of a drop-stitch panel?**

   Since the structural characteristics of drop-stitch panels are relatively unknown compared to other structures used in offshore applications such as steel panels or beams, a study into the influence of the internal air pressure, yarn distance and thickness will be performed. The total thickness of a drop-stitch floater and internal air pressure are expected to be dominant factors in the bending stiffness. Of course, the width and length also influences the structural characteristics significantly, but their influences are not considered in this study. In most steel structures, the bending stiffness is dominated by the thickness of the structure. Drop-stitch floaters are a bit more unique in that sense, since the internal air-pressure also highly influences the bending stiffness.

3. **What is material behaviour of the face sheets?**

   The drop-stitch panel is made out of a polyester fiber coated with PVC. This is a complex material to model, since it is expected to be an orthotropic hyperelastic material. Whether the orthotropy and hyperelasticity is significant, should be investigated. A tensile test is performed to analyse the stress-strain behaviour and different material models are evaluated. The material models are implemented in a FE model of a drop-stitch panel to analyse the difference in response of the drop-stitch panel.

4. **What is the mechanism behind the bending behaviour?**

   Prior research has already shown that wrinkling is an important factor in the non-linear bending stiffness and eventual collapse of the drop-stitch panel. More research should be performed into the initiation and propagation of wrinkling to obtain a better understanding of the bending behaviour and failure mechanism. This can eventually be used to determine limit states of a drop-stitch floater. Also, it could be usable to establish realistic predictions of the structural response of a drop-stitch floater.

1.4   Outline

The performed literature study is evaluated in chapter 2. It gives an overview of the basics and state-of-the-art of research related to the structural characteristics and a basis for all the considerations and assumptions made in this report. Chapter 3 gives the theoretical background of the `ABAQUS` FE model. This shows an evaluation of the procedures used in `ABAQUS`. Only the procedures that are considered during the research, has been mentioned in this chapter. Chapter 4 shows the result of a load controlled three point bending test performed on a drop-stitch floater. It gives insights in the bending characteristics of drop-stitch floaters and is used as validation experiment. The material behaviour is discussed in chapter 5. It discusses the hyperelastic and orthotropic behaviour of the polyester fiber coated with PVC. An uniaxial tensile test has been performed to establish a material model. Chapter 6 shows a description of the 3D FE model of the drop-stitch floater and its results. Different air pressures, material models, yarn distances and face sheet thicknesses are evaluated. The 3D FEM is also compared to the experiments performed in chapter 4. Finally, the conclusion of this research can be found in chapter 7, which gives the answers to the research questions. Further recommendations for research is elaborated in chapter 8.

Chapter 2

Literature

In this chapter, the relevant literature is presented to show the current state of research, give background information and substantiate the methodology. First, an overview of relevant characteristics of the (flexible) drop-stitch panels are presented in section 2.1. The relevant characteristics are the characteristics that have influence on the structural behaviour such as the shape, used materials, air pressure and non-linearities. A brief evaluation of the mechanical characteristics of flexible solar panels can be found in section 2.2. Afterwards, the methodologies to implement wrinkling of a thin membrane in a FE model are discussed in section 2.3. The modelling of pressurised membranes is discussed in section 2.4. Finally, structural models are discussed in section 2.5.

2.1   Drop-Stitch Panels

The idea of drop-stitch panels originates from the aerospace industry. In 1933, Taylor McDaniel had the idea to develop a glider entirely of an air-inflated rubber tubing, which he believed would make aircrafts safer, cheaper and lighter [33], shown in figure 2.1. A few decades later in 1957, Goodyear Aircraft [34] developed an one-place collapsible pneumatic aircraft, which can be considered as one of the earliest documentations of drop-stitch panels to the best of the author's knowledge. Goodyear Tire and Rubber Company developed the "Airmat", which is described as: "A pneumatic structural material consisting of two layers of fabric restrained, when inflated, by continuous tie yarns dropped from one layer of fabric to the other at the time of weaving."[34] With this "Airmat", they have developed the Inflatoplane, shown in figure 2.2. A preliminary study showed that this airplane could also be collapsed into a package, dropped from an airplane by a parachute and prepared for flight by one person. This sounded very promising and it was all possible due to a new structure called the "Airmat".
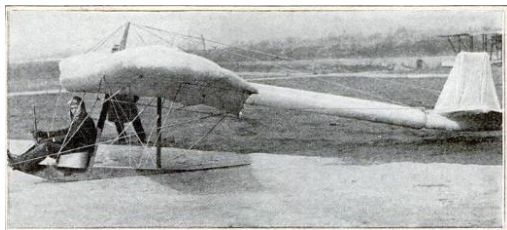
Figure 2.1: A photograph of the rubber glider of Taylor McDaniel [35].

Figure 2.2: A photograph of the Goodyear Inflatoplane [35].

Drop-stitch panels are used for different purposes nowadays in marine structures such as Rigid Inflatable Boats and Stand Up Paddle boards [31, 36]. They basically consists out of two fiber cloths with an internal air pressure and a numerous amount of vertical or diagonal yarns, which connect the upper and lower cloth, figure 2.3. The edges of the panels are round, which creates a transverse cross-section with an obround shape. The internal air pressure contributes to the

7

stiffness and the vertical threads gives the panel a flat shape [34]. Due to the fact that most of the stiffness is established by air pressure, drop-stitch panels are lightweight. By changing the air-pressure, the bending stiffness can be adjusted.
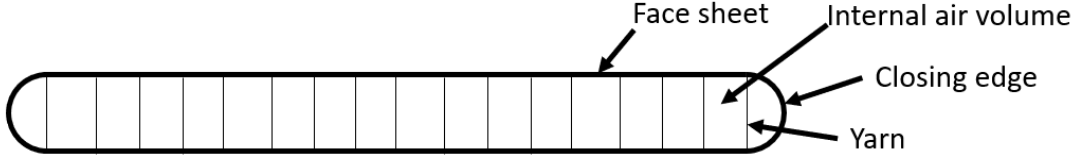
Figure 2.3: Sketch of the transverse cross section of a drop-stitch panel

2.1.1 Research into drop-stitch panels

To the best author's knowledge, few research have been performed on low pressure drop-stitch panels. many research has been focused on the high pressure inflatable beams/plates [24, 31, 32, 37–42]. Cavallaro [24] performed a four point bending test, which gives some insight in the bending stiffness behaviour of a drop-stitch panel at different internal air pressures ranging from 5 - 30 psig, which is roughly 35-207 kPa. The intended drop-stitch panels used as flexible inflatable floater are in the range of 5-20 kPa, so considerably lower. Cavallaro [24] showed that the deflection behaves non-linearly with increasing bending load, so assuming a linear beam/plate model would be insufficient at higher deflections. At the wrinkling onset, which is the bending load at which the cloth starts to wrinkle, the bending stiffness decreases significantly. The wrinkling onset increases for increasing internal air pressures. The internal air pressure creates a pretension as shown in figure 2.6. It will increase due to a loss in a volume at the wrinkling onset [43], so the pressure-volume work should be taken into account [38]. Figures 2.4 and 2.5, shows the results of the four point bending test performed by Cavallaro [24] in which a drop-stitch panel is tested until it reached a mid span deflection of around 6 inches ($\approx$152 mm).
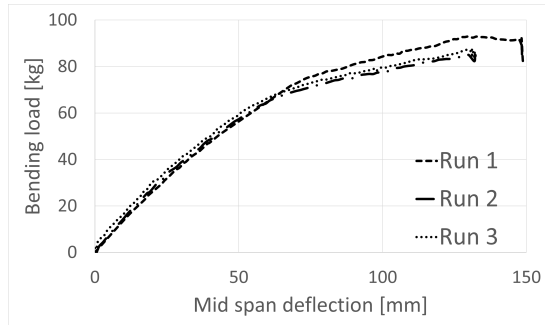
Figure 2.4: Results of 4 point bending tests of Cavallaro [24] converted to SI units using an internal air pressure of 35kPa
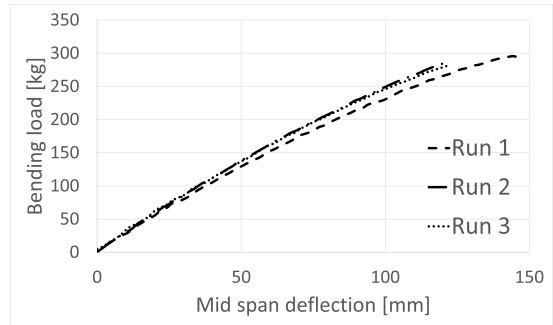
Figure 2.5: Results of 4 point bending tests of Cavallaro [24] converted to SI units using an internal air pressure of 207kPa
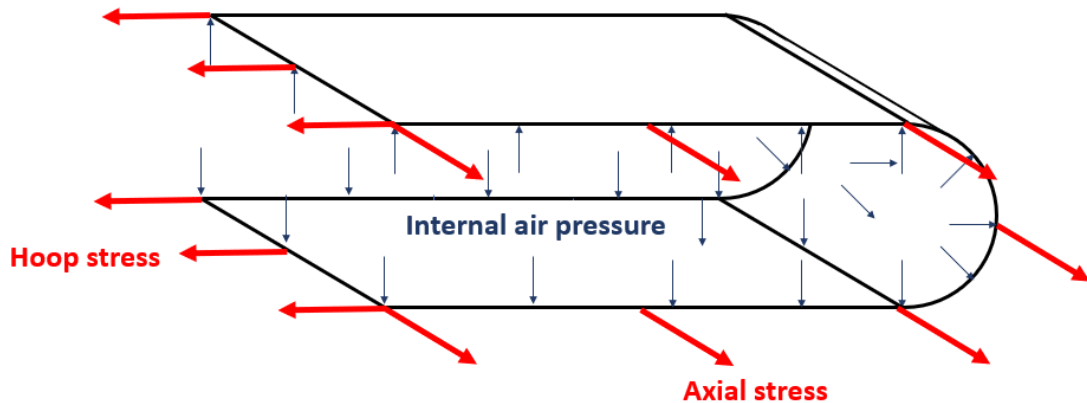
Figure 2.6: A sketch of the pretension (the hoop and axial stresses) created by the internal air pressure. Note that the yarns are not included in this sketch.

There are a couple of non-linearities, which influences the response of a drop-stitch floater. The non-linear components of the stiffness are divided into four types:

- Material: For larger strains, the material stiffness of the double woven fabric (DWF) coated with PVC changes due to mechanical phenomena such as plastic deformation and hyperelasticity. This will be further elaborated in chapter 5.
- Load: The internal air pressure exerts a load normal to the inner surface. Especially with local loads, this could have an influence. Air is a compressible fluid, so if a local load exerts onto the drop-stitch panel, a local indent/outdent could occur. Also, observations of a preliminary experiment of TNO showed that an indentation on one side of the drop-stitch panel, results in an outdent on the opposite side. The pressure-volume work should also be taken into account as load non-linearity. Pressurised membranes are further discussed in section 2.4.
- Geometry: A geometry non-linearity arises due to wrinkling/slack, which is a local buckling phenomenon. It relaxes a thin membrane from compressive stress due to a lack of bending stiffness. A drop-stitch panel is a pretensioned structure. The pretension is developed by the air pressure, which creates hoop stresses within the fiber cloths. If the pretension is nullified, wrinkling might be initiated. Wrinkling is further discussed in section 2.3.

2.1.2 Limit States

Setting limits to the deflection, curvature, strains and stresses, is very important to prevent failure of the structure and ensure its reliability. The types of failures or limits can be divided into four categories from the viewpoint of structural design [44]:

- The serviceability limit state (SLS)
- The ultimate limit state (ULS)
- The fatigue limit state (FLS)
- The accidental limit state (ALS)

FLS and ALS will not be discussed in this report. FLS represents the occurrence of fatigue cracking due to damage accumulation, which is needed to ensure the design life time. ALS ensures that the structure can withstand accidental local loads. FLS and ALS are not further evaluated in this research.

SLS is based on the limits of deflections or vibrations for normal use. The minimum bending radius to avoid plastic deformation of the solar cells, which is discussed in section 2.2, can be considered

as a serviceability limit state. The structure does not collapse yet, when the solar cells are plastic deformed, but it does influence the workability of the solar cells. Cavallaro et al. and Davids et al. showed that wrinkling cause a decrement in bending stiffness. If the wrinkles develop, the bending stiffness decrease and the drop-stitch floater collapses. This reduces the workability of the drop-stitch floater, so this might be an important limit state. The phenomenon wrinkling will be discussed further in section 2.3.

To prevent plastic collapse or surpassing the ultimate strength, an ULS is set as a design criteria. The face sheets can withstand a limited amount of tensile stress. At some point, the face sheets will rupture due to tensile stress. It is expected that wrinkling relaxes the face sheets from compressive stresses, so compressive stresses might not be significant for drop-stitch panels on a local level. This does not imply that global compressive load are insignificant. Global compressive loads can cause local tensile loads due to buckling. Also, it could increase the air pressure within the drop-stitch floater, which could cause rupture. Ultimate limit states are not further investigated in this research.

DNV proposed a comprehensive set of requirements, recommendations and guidelines for the design, development, operation and decommissioning of FPV systems [30]. They considered multiple environmental and site conditions which should be taken into account for FPVs: wind, waves, currents, snow and ice accreation, fouling, ecology. In their report on the design, development and operation of FPVs, they have mostly focused on high stiffness and linear elastic floaters, so this is not fully applicable to flexible and non-linear elastic floaters.
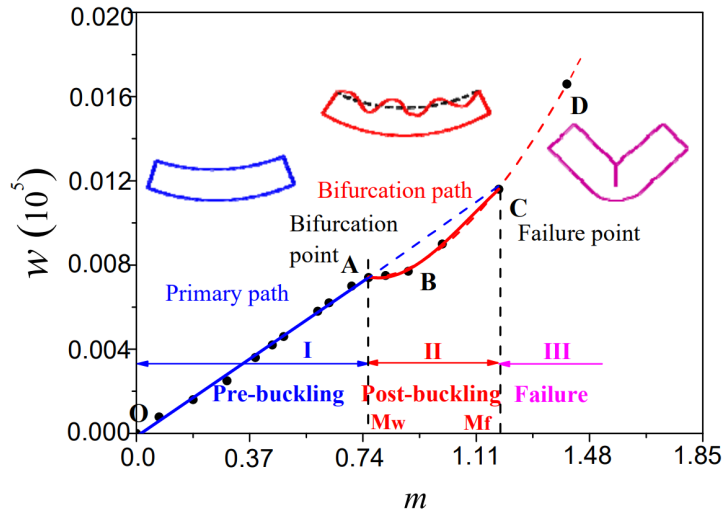
Figure 2.7: The numerical moment-deflection response path of the inflated beam under bending [45].

Few research has been performed on the limit states of drop-stitch panels. Liu et al. has performed research into the bending wrinkling behaviour of an inflated cylindrical beam using a model based on a Fourier series [45]. They divided the bending response into three stages: the pre-buckling, post-buckling and failure stage. This does give some insight in the response path, but it is unknown whether this is also applicable for drop-stitch panels. Drop-stitch panels have a different geometry and contain yarns. Considering the application as FPV, the drop-stitch panel is considered to be failed in the post-buckling region II as shown in figure 2.7, where the bending stiffness is small. The failure region III in figure 2.7 is not considered in this research. Veldman [46] analysed the bending response of different inflatable braided cylindrical beams. Fichter [47] derived the global buckling load for inflatable thin-walled cylindrical beams, which are further evaluated and compared with

a structural model by Davids et al. [38]. However, in this thesis buckling loads are not further investigated.

2.2 Mechanical behaviour of flexible Solar Panels

Over the last decades, thin and flexible solar panels have improved. Thin-film solar cells were first used to power hand-held calculators in the 1970s and now cars are developed, which are powered by thin and flexible solar cells [48]. This indicates the fast development of thin-film solar cells. From a structural perspective, the solar panels could give an additional stiffness contribution to the drop-stitch panels. Also the bending radius of a flexible solar panels is limited, so the curvature of the floaters should be limited accordingly as shown in the brochure of MiaSolé, which is a manufacturer of lightweight, flexible and thin solar cells [49]. Otherwise, plastic deformation or cracks will occur in the solar panels. The flexibility of a solar panel is highly dependent on the substrate used. The types of substrates can be divided into metals, ceramic and plastics. A qualitative review of these substrates is shown in figure 2.8 [48]. It clearly shows that there is not one material which is the best in everything. A proper trade-off should be made to decide which material to use. The definition of the five key material properties are:

- Flexibility: The ability to bend without mechanical failure;
- Portability: The oxygen and water vapour transmission rates, which indicates the ability of oxygen and water vapour to traverse the substrate. A high portability could decrease the efficiency of flexible solar panels. [50];
- Thermal stability: The ability to withstand high temperatures, which depends on the thermal expansion rate;
- Optical stability: The optical transmittance or reflectance;
- Environmental stability: The resistance to environmental chemical attacks.
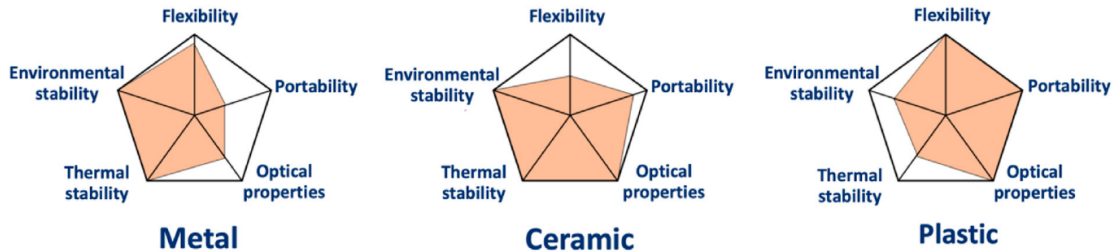
Figure 2.8: A qualitative review of metal, ceramic and plastic substrates and the common five key material properties for flexible solar panels [48]

The nominal structural behaviour of a solar cell depends on the components used within the solar cell, figures 2.9 and 2.10 [51]. This shows that the mechanical behaviour of solar panel is quite complex and difficult to predict and is highly dependent on the components used. The influence of a solar panel on the stiffness of the entire structure will not be evaluated further in this thesis.

2.3 Wrinkling models of membranes

The wrinkling phenomenon affects the stiffness of the drop-stitch panels. It relaxes a shell element from compressive stresses and affects the global bending stiffness [24, 32]. Wrinkling of a membrane can be introduced by different load conditions as long as compressive stresses/strains are introduced. In this thesis the decay of global bending stiffness of a drop-stitch floater due to wrinkling is analysed, so the wrinkled regions and directions need to be taken into account. A local
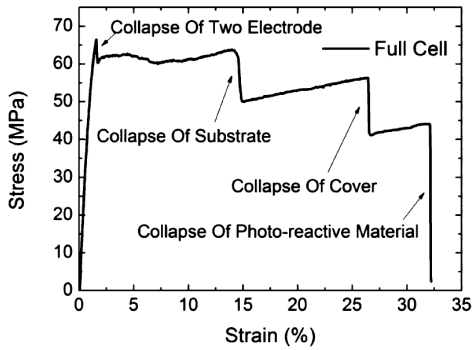
Figure 2.9: An example of a nominal stress-strain curve of full cell packaging [51]
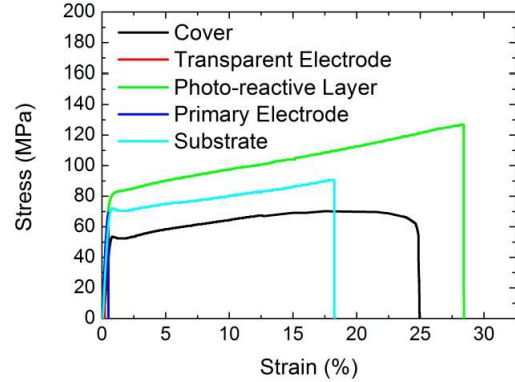
Figure 2.10: An example of a stress-strain curve per component of full cell packaging [51]

decay of bending stiffness due to wrinkling could introduce a hinge at large deflections as shown in figure 2.7. Two types of wrinkling are distinguished: material and structural wrinkles. Material wrinkles are permanent out-of-plane deformations due to imperfections in the manufacturing process and structural wrinkles are caused by localised buckling due to compressive stresses [52]. Material wrinkles will not be evaluated in this report. Also, wrinkles in elastic-plastic sheets are not evaluated, since the wrinkling propagation may differ from (hyper)elastic sheets.

The wrinkling regions and direction are dependent on material properties such as fiber direction and degree of orthotropy [53, 54]. The degree of orthotropy is defined as the ratio between the Young's modulus of the transverse and longitudinal fiber direction. Liu [53] showed that the wrinkling deformation decreased for lower degrees of orthotropy for a hyperelastic membrane loaded in uniaxial tension. Material properties will be further discussed in chapter 5.

Pocivavsek et al. and Jambon-Puillet et al. provided scaling laws for wrinkles and folds of thin elastic membranes supported on a fluid [55, 56]. Their scaling law is based on a balance between internal bending and potential energy generated by fluid. For the face sheets of the drop-stitch floater, the pretension generated by the internal air pressure is something to take into account to develop such scaling laws. Cerda et al. established a scaling law for thin elastic sheets under uniaxial tension [57, 58]. They used an energy minimisation function of the bending and strain energy. Developing such scaling laws for the face sheets of drop-stitch floaters might be a bit more complicated, since multi-axial loads are applied to the face sheets. There are out of plane loads due to the air pressure and yarns and in plane loads due to the pretension and compression.

Two methodologies to include wrinkles in FEM are evaluated further in this section: tension field and perturbations. Also, the determination of the wrinkling onset moment as described by Cavallaro et al. is assessed [24].

2.3.1 Tension field theory

Miller [59] provided an iterative approach to determine the wrinkled/slack regions based on a stress criterion. After a few load increments, they have adjusted the stiffness properties locally with the strain criterium of table 2.1 with σ_n is the stress and ε_n strain in a certain direction. Using this methodology, one will model a fictitious membrane instead of a wrinkled membrane as shown in figure 2.11 in which F_c is a compressive load and ΔL the axial deformation. The fictitious membrane discards the exact wrinkled geometry and represents an averaged smoothed surface. It is also known as the tension field theory. Roddeman [60] proposed a wrinkling model

in which the deformation gradient tensor in wrinkled regions is modified to produce this fictitious membrane as shown in figure 2.11. Kang [61] reported a new iterative scheme, which uses a mixed stress-strain criteria. Wang [62] proposed a new approach for the judgement of wrinkling state shown in table 2.2. This solved a specific judgement error by considering the previous state of the previous iteration, which caused a slack state erroneously be judged as wrinkled state [62]. Table 2.2 shows that if the previous state of a iteration is a taut state, the current state is determined using a principal stress criterion. If the previous state is a wrinkled or slack state, the principal strain criterion is used to judge the current state of a iteration. Note that his methodology assumes that a membrane is very thin and therefore has no compressive stiffness, since it will easily buckle. This will not provide detailed information about wrinkling deformation. However, it is sufficient to analyse the global stiffness behaviour of drop-stitch panels. Performing a post wrinkling analysis, is not necessarily needed to analyse the global deformation of a drop-stitch panel, since it will only assess the local wrinkling deformations and not influence the global deformation as shown in figure 2.11. A few references on post wrinkling analysis of membranes for different load cases include [57, 58, 63, 64]. In these references, they have analysed the wrinkling patterns of a thin membrane due to a shear, uniaxial and biaxial tension load. Nakashino et al. [65] implemented the mixed stress-strain criterion of table 2.2 and the wrinkling model of Roddeman et al. [60]. They have analysed large folds in an airbag type structure. Better mesh convergence rates were observed with the tension field model than the non tension field model. Also, large compressive stresses remain in the non tension field model in some parts of the airbag, which is also mentioned by Iwasa et al. [66]. Iwasa et al. also mentions that it is better to deal with the membrane instead of a plate if the characteristic length to thickness ratio is larger than 1000.
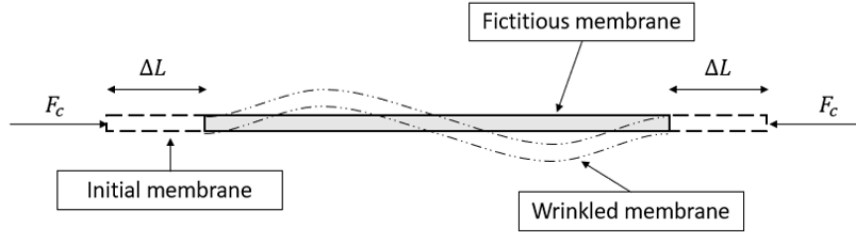
Figure 2.11: Depiction of the initial membrane without compression load, fictitious membrane with compression load and wrinkled membrane.

Table 2.1: Different criteria of the state of a membrane mentioned by Wang et al. [62]

State of membrane	Principal stress criterion	Principal strain criterion	Mixed criterion
Taut	$\sigma_2 > 0$	$\varepsilon_2 > 0$	$\sigma_2 > 0$
Wrinkling	$\sigma_2 \leq 0$ and $\sigma_1 > 0$	$\varepsilon_2 \leq 0$ and $\varepsilon_1 > 0$	$\sigma_2 \leq 0$ and $\sigma_1 > 0$
Slack	$\sigma_1 \leq 0$	$\varepsilon_1 \leq 0$	$\varepsilon_1 \leq 0$

Table 2.2: The judgement approach of wrinkling state proposed by Wang et al. [62]

Case	Previous state	Current state	Conditions	Comments
1	Taut	Taut	$\sigma_2 > 0$	Principal Stress Criterion
2		Wrinkled	$\sigma_2 \leq 0$ and $\sigma_1 > 0$	
3		Slack	$\sigma_1 \leq 0$	
4 (7)	Wrinkled (Slack)	Taut	$\nu\varepsilon_1 + \varepsilon_2 > 0$	Principal Strain Criterion
5 (8)		Wrinkled	$\nu\varepsilon_1 + \varepsilon_2 \leq 0$ and $\varepsilon_1 > 0$	
6 (9)		Slack	$\varepsilon_1 \leq 0$	

`ABAQUS` has the option to apply a no-compression material property for linear elastic and isotropic hyperelastic materials. A no-compression material property is obtained by first solving the principal stresses assuming linear elasticity and then setting the appropriate principal stress values to zero using the principle stress criterion of table 2.2. The associated stiffness matrix components in the wrinkling direction will also be set to zero. The no-compression material property is not history dependent, so the proposed methodology by Wang [62], which takes into account the previous taut/wrinkling/slack-state, is not adopted. Wong et al. [67] observed poor convergence by using the `*NOCOMPRESSION` option of `ABAQUS`. Their observations are not elaborated extensively, so the reason for the poor convergence is unclear.

2.3.2 Initial perturbations

Another methodology to model wrinkling behaviour is to introduce geometrical imperfections or perturbations [67–71]. This method has been used to determine the wrinkles of an airbag [62]. Wong et al. [67] explained this this methodology thoroughly. First the FE model is defined and a small pretension as initial condition is applied. In step II, they have performed a buckling analysis and used the resulting modes as perturbations. In the final step they increased the load and used a stabilisation function to achieve convergence. Lavaerts [72] showed that it could be difficult to obtain the first buckling mode for some geometries and the post-buckling behaviour is highly dependent on the perturbations used. Also, this methodology costs significantly more calculation time than the principal stress/strain criterion methodology.

2.3.3 Wrinkling onset

Cavallaro et al. [24] determined the wrinkling onset moment of a drop-stitch panel with high internal air pressure. They have determined a bending moment needed to nullify the pretension created by the internal air pressure. Equation 2.1 shows the wrinkling onset moment, M_{onset}, with P is the internal air pressure, B width of the panel and H the height. They did not include the mass of the panel, so this might be corrected especially for flexible drop-stitch panels. The maximum moment was predicted with $M_{max} = 2M_{onset}$, which showed good correlation at high internal air pressures. However, at lower internal air pressures (≤ 60 kPa) it became inaccurate.

$$M_{\mathrm{onset}} = \frac{P}{16} H\left(P\right)^2 \frac{\left(4B\left(P\right) - 4H\left(P\right) + \pi H\left(P\right)\right)^2}{\left(2B\left(P\right) - 2H\left(P\right) + \pi H\left(P\right)\right)} \tag{2.1}$$

2.3.4 Concluding remarks

There are two methodologies to take into account wrinkling: initiate perturbations or assume a tension only material property. Initiating a initial perturbation models the full wrinkling pattern, which gives a more detailed description of the wrinkles. It is expected that initial air pressure and yarns initiate sufficient initial perturbations for a bending load case and a modal analysis as Wong et al. did [67] to determine an initial deflection is not needed. A tension only material property models the wrinkles by assuming no compressive stiffness. Both methodologies give accurate predictions for the wrinkling response. The analytical approach used by Cavallaro et al. seems to accurately predict the wrinkling onset moment [24]. The analytical maximum moment formulation is inaccurate for the intended internal air pressure range of this research.

The initial perturbations method requires a finer mesh, since it is expected that the wrinkling pattern is dependent on the yarn distance. If one would model a large panel with a small yarn distance, a large amount of elements are needed, which increases the calculation time. Assuming tension only/no compression material property, could result in convergence issues. However, a coarser mesh could be used, since the full wrinkle deformation does not needed to be modelled. In this research, the perturbation model is used, since it develops a better understanding in the wrinkling initiation and propagation.

2.4 Pressurised membranes

The internal air pressure is a significant variable in the bending stiffness behaviour of the drop-stitch panels [32, 43]. A higher internal air pressure increases the linear bending stiffness and wrinkling onset and also influences the post wrinkling bending stiffness. Hulton et al. [31] assumes the Ideal Gas Law for air 2.2 and the compression cycle of a gas can be treated as a polytropic process. Polytropic processes are thermodynamic processes that obey equation 2.3. For isothermal processes, $n_{heat} = 1$ and equations 2.3 becomes the ideal gas law of equation 2.3. This could be used to formulate an idealised total energy balance for an air-inflated structure, equation 2.4 [43]. In equations 2.2-2.4, P is the internal air pressure, V the volume, R_{gas} the gas constant, N_{gas} the amount of substance of gas in moles, T the temperature, n_{heat} the ratio of specific heats, C a constant value for two states of a polytropic process, F an externally applied force, δ the deflection at point of loading, E_{strain} the sum of the elastic and plastic strain energies, $E_{kinetic}$ kinetic energy of the system mass, $E_{dissipative}$ dissipated energy through damping and viscous effects. The Δ denotes the difference between the initial (after inflation) state and the state after a load has been exerted on a inflatable structure.

$$PV = N_{gas}R_{gas}T \tag{2.2}$$
$$PV^{n_{heat}} = C \tag{2.3}$$

$$\int Fd\delta = \Delta E_{\text{strain}} + \Delta E_{\text{kinetic}} + \Delta E_{\text{dissipative}} + \Delta \int PdV + \Delta \int VdP \tag{2.4}$$

As mentioned, pretension created by the internal air pressure influences the wrinkling onset. The pretension can be separated into transverse hoop stresses and axial stresses as shown in figure 2.6. For thin and isotropic obround shapes, the hoop stresses could be estimated using equation 2.5 at locations A, B and C of figure 2.12 according to the ASME[73]. A Thickness of less than one tenth of the radius is considered to be thin [74]. The parameters of equation 2.5 are shown in figure 2.12. Cavallaro et al. assumes that the pretension is uniformly distributed over the cross sectional area in axial and transverse direction instead of determining a non-uniform pretension as ASME did[24]. Using that assumption, they accurately determined the wrinkling onset moment as discussed in section 2.3. The inflation pressure is multiplied with the longitudinal projected area and divided by the circumferential area of the obround shape, equations 2.6-2.7. However, Hulton et al. [31] showed that the maximum principal stresses in the corners of a drop-stitch panel are non uniform, figure 2.13. Of course, maximum principal stresses and membrane stresses are not the same, but it shows that equation 2.5 should be used carefully. Note that the influence of the yarns on the pretension is not taken into account. Between the yarns, small bumps are introduced by the yarn spacing and internal air pressure, figure 2.14. It is expected that these bumps decreases for smaller yarn spacing.

$$(\sigma_h)_B = PR/t_1 \quad , \quad (\sigma_h)_C = P(R+L_2)/t_1 \quad , \quad \sigma_h = PR/t_2 \tag{2.5}$$

$$\sigma_x = \frac{F_{\text{longitudinal}}}{(2(B-H)+\pi H)t_{\text{face}}} \text{ with } F_{\text{longitudinal}} = P\left((B-H)H + \pi\frac{H^2}{4}\right) \tag{2.6}$$

$$\sigma_y = \frac{F_{\text{hoop}}}{(2(L-H)+\pi H)t_{\text{face}}} \text{ with } F_{\text{hoop}} = P\left((L-H)H + \pi\frac{H^2}{4}\right) \tag{2.7}$$
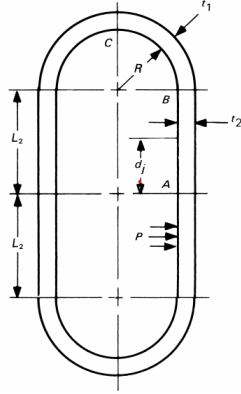
Figure 2.12: Cross section of obround pressure vessel [73]
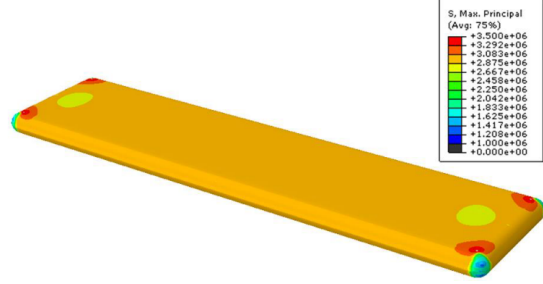
Figure 2.13: Maximum principal stress (in PA) of the drop-stitch panel skin at 20 psi (138 kPA) inflation pressure [31].
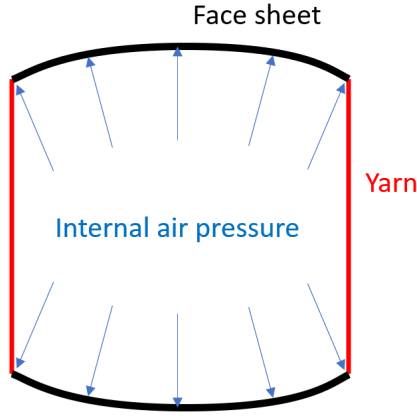
Figure 2.14: The small bumps between each yarn due to the internal air pressure.

Taffetani et al. [75] modelled a pressurised spherical elastic shell in `ABAQUS`. They used a surface based fluid cavity as air chamber. Their simulation was conducted in two steps: first an inflation step to reach the desired pressure with a static solver and afterwards an indentation step to apply a desired indention into the spherical elastic shell using a dynamic implicit solver. By introducing a Rayleigh damping proportional to the mass, the solution was stabilised. Hulton et al. [31] took the adiabatic expansion of the enclosed air volume into account, which Taffetani et al. did not. The Shomate equation is used to determine the molar heat capacity, equation 2.8 with $\tilde{a}$, $\tilde{b}$, $\tilde{c}$, $\tilde{d}$, $\tilde{e}$ are gas constants [76]. The molar heat capacity is the amount of heat needed to add to amount of mass to increase the temperature with a certain amount. Adiabatic means "without heat transfer", so there is no heat transfer with its surroundings [77]. It should be taken into account for rapid volume changes such as the compression in a cylinder of an engine. The internal air pressure of a drop-stitch panel is influenced by wind gusts according to preliminary observations made by TNO, which suggests that the internal temperature is mainly influenced by the environment. Taffetani et al. did not take into account temperature changes due to volume changes and assumed an isothermal process.

$$\tilde{c}_p = \tilde{a} + \tilde{b}\left(T_0 - T_1\right) + \tilde{c}\left(T_0 - T_1\right)^2 + \tilde{d}\left(T_0 - T_1\right)^3 + \frac{\tilde{e}}{\left(T_0 - T_1\right)^2} \tag{2.8}$$

2.4.1 Concluding remarks

There are two options to analytical determine the pretension: an uniform or a non-uniform formulation over the cross sectional area. Cavallaro et al. acquired accurate results for the wrinkling onset using the assumption that the pretension is uniformly distributed over the cross sectional area, so this suggests that it is not necessary to determine a non-uniform pretension to determine the wrinkling onset analytically. For the FEM model, The internal air volume should be modelled as a surface based fluid cavity in `ABAQUS`. The panel should first be inflated and afterwards the load case should be applied. Taking into account the adiabatic heating effect of the enclosed air volume, is not necessarily needed.

2.5 Structural models

Simplifying structures to analyse its response to certain load conditions, is the main purpose of structural models. If certain dimensions are significantly smaller than others, a beam or plate model could be adopted. Beams are one dimensional elements that could be used if the thickness and width are smaller than the length. Plates can be adopted if the thickness is atleast one-tenth smaller than the in-plane dimensions [78].

The governing equations of structural models are stated in section 2.5.1. An evaluation of different beam and plate models are presented in sections 2.5.2 and 2.5.3 respectively. Implementations of structural models on drop-stitch panels are evaluated in section 2.5.4

2.5.1 Governing equations

To preserve a static equilibrium, equation 2.9 should be obeyed at every location in the model with $\mathbf{F}$ is a force and moment tensor, $\mathbf{K}$ a stiffness tensor and $\mathbf{u}$ a DoF tensor. This assumes that there is no velocity in the system.

$$\mathbf{F} = \mathbf{Ku} \tag{2.9}$$

For linear elastic material, the stress $\boldsymbol{\sigma}$ and strain $\boldsymbol{\varepsilon}$ vectors are related with a material stiffness matrix $\mathbf{C}$ [79]:

$$\boldsymbol{\sigma} = \mathbf{C}\boldsymbol{\varepsilon} \quad \text{with} \quad \boldsymbol{\sigma} = \begin{bmatrix} \sigma_x \\ \sigma_y \\ \sigma_z \\ \sigma_{xy} \\ \sigma_{yz} \\ \sigma_{xz} \end{bmatrix} \quad \text{and} \quad \boldsymbol{\varepsilon} = \begin{bmatrix} \varepsilon_x \\ \varepsilon_y \\ \varepsilon_z \\ \gamma_{xy} \\ \gamma_{yz} \\ \gamma_{xz} \end{bmatrix}$$

The normal and shear strains can be determined by the calculating the derivatives of the in its respective directions:

$$\begin{aligned} \varepsilon_x &= \frac{\partial u}{\partial x}, & \varepsilon_y &= \frac{\partial v}{\partial y}, & \varepsilon_z &= \frac{\partial w}{\partial z}, \\ \gamma_{xy} &= \left(\frac{\partial u}{\partial y} + \frac{\partial v}{\partial x}\right), & \gamma_{yz} &= \left(\frac{\partial v}{\partial z} + \frac{\partial w}{\partial y}\right), & \gamma_{xz} &= \left(\frac{\partial u}{\partial z} + \frac{\partial w}{\partial x}\right) \end{aligned}$$

2.5.2 Beam models

One could analyse the response of a structure in two dimensions by adopting a beam theory. Beam theories assume that the displacements in y-direction and rotations in x- and z-direction are zero. The deformations u and w are only described as functions of the x and z coordinates. The Euler-Bernoulli beam theory is considered to be the simplest beam theory. It assumes that shear deformation in xz-plane is negligible, so that u can be described as function of w and z [78]:

$$u(x, z) = -z\frac{dw_0}{dx}, \quad w(x, z) = w_0(x)$$

with w_0 is the mid-thickness deflection as shown in figure 2.15. Note that the deformations described in sections 2.5.2 and 2.5.3 are for pure bending cases without in plane deformations. It implies a displacement u, which can be described as a straight line normal to the midplane deflection w. For thicker beams and larger deflections, shear deformation becomes more significant, so it should be included. Timoshenko [80] included the shear deformation of a beam by adding the angle ϕ:

$$u(x, z) = z\phi(x), \quad w(x, z) = w_0(x)$$

This still assumes u can be described as a straight line to the midplane deflection. However, the straight line is not normal to the midplane deflection as shown in figure 2.15. Higher order shear theories such as a second third order (also known as the Reddy Beam Theory), further relaxes the straightness assumption [78]. The higher order theories adds unknowns, which are difficult to interpret in physical terms. The accuracy gained with higher than 3rd order is little. The second order beam theory is described as:

$$u(x, z) = z\phi(x) + z^2\psi(x), \quad w(x, z) = w_0(x)$$

and the third order as:

$$u(x, z) = z\phi(x) + z^2\psi(x) + z^3 + u_0\theta(x), \quad w(x, z) = w_0(x)$$
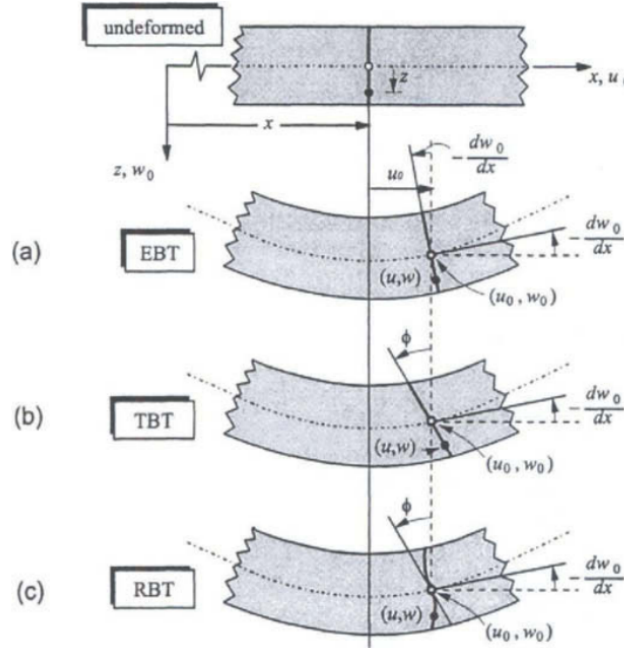
Figure 2.15: Deformation of a typical transverse normal line in various beam theories [78]. EBT is the Euler-Bernoulli Beam Theory, TBT the Timoshenko Beam Theory and RBT the Reddy Beam Theory.

2.5.3 Plate models

Similar to the beam models, plate models also consists of simple models, which neglect shear deformation, and n-order shear deformable plate theories. The difference between plate and beam theories is the deformation in y-direction that is included.

The Classical (Kirchoff) Plate Theory is an extension of the Euler-Bernoulli beam theory to two dimensions [79]. It neglects, similar to the Euler-Bernoulli beam theory, the shear deformation, so:

$$u(x,y,z) = -z\frac{\partial w_0}{\partial x}, \quad v(x,y,z) = -z\frac{\partial w_0}{\partial y}, \quad w(x,y,z) = w_0(x,y)$$

The Mindlin plate theory assumes first-order shear deformation plate theory. It is an extension of the classical plate theory by including transverse shear deformation:

$$u(x,y,z) = z\phi_x(x,y) \quad v(x,y,z) = z\phi_y(x,y) \quad w(x,y,z) = w_0(x,y) \tag{2.10}$$

The higher order plate theories adds additional unknown. The second-order plate theory can be described as:

$$u(x,y,z) = z\phi_x(x,y) + z^2\psi_x(x,y) \quad v(x,y,z) = z\phi_y(x,y) + z^2\psi_y(x,y) \quad w(x,y,z) = w_0(x,y) \tag{2.11}$$

and the third-order plate theory as:

$$u(x,y,z) = z\phi_x(x,y) - \alpha z^3\left(\phi_x + \frac{\partial w_0}{\partial x}\right) \quad v(x,y,z) = z\phi_y(x,y) - \alpha z^3\left(\phi_y + \frac{\partial w_0}{\partial y}\right) \quad w(x,y,z) = w_0(x,y) \tag{2.12}$$

with $\alpha = \frac{4}{3h^2}$. It reduces to the first order shear deformable plate if $\alpha = 0$.

Laminated composites are inhomogeneous in the thickness direction. A common analytical approach used for laminated composites to determine the structural response is the classical laminate theory (CLT) [81]. CLT is based on the classical plate theory [79]. Using CLT, one can analyse the multi-axial responses of structures with direction dependent stiffness properties and loaded by multi-axial loads. CLT makes the following assumptions:

1. The plate consists of orthotropic laminae bonded together with their principal material axes of the orthotropic laminae orientated in the x-y plane.
2. The thickness of the plate is much smaller than any characteristic dimension (the length and the width) (defined by the Kirchhoff hypothesis).
3. The displacements u, v and w are small compared with the thickness (geometrical linearity).
4. The in-plane strains ε_x, ε_y and γ_{xy} are small compared with unity, so each ply obeys Hooke's law (material linearity).
5. Transverse shear is negligible (plane stress in each ply) (defined by the Kirchhoff hypothesis).
6. Displacements u and v are linear functions over the thickness (defined by the Kirchhoff hypothesis).

Using the assumptions of CLT for flexible drop-stitch panels, gives multiple issues. First of all, assumption 3 can not be assumed for a very flexible panel, since large displacements are expected. Assumption 4 should be handled with care, since materials could become non-linear at certain strains. Transverse shear is expected at high deformations, so assumption 5 is invalid. This implies that the CLT can not (directly) be used. If one would be interested in using the CLT for drop-stitch floaters, a modified non-linear CLT should be devised.

The constitutive relation of the CLT is shown in equation 2.13, which relates the forces and moments per unit length to strain and curvature [79, 82]. The stiffness matrix of this equation is referred to as the ABD-matrix. The components of the ABD-matrix can be determined using equations 2.14-2.16 in which k is the ply number, z_k is the outer fiber distance of a ply from a reference axis and z_{k-1} the inner fiber distance of a ply. Equations 2.14-2.16 assumes constant

thickness over the laminate. The reduced stiffness matrix, $\bar{Q}_{ij}^{(k)}$, can be determined using equation 2.17. $[T]^{(k)}$ is the transformation matrix of equation 2.18, which relates the orthogonal fiber directions to the global cartesian coordinate system using the ply direction θ. $[L]$ relates the tensorial shear strain to the engineering shear strain in equation 2.19. The stiffness matrix of one linear elastic orthogonal ply is determined using 2.20, which is based on Hooke's law. ν is the Poisson's ratio, G_{nm} the shear modulus in nm-direction, E the Young's modulus.

$$\left\{ \begin{array}{c} \{N\} \\ \{M\} \end{array} \right\} = \left[\begin{array}{cc} [A] & [B] \\ [B] & [D] \end{array} \right] \left\{ \begin{array}{c} \{\varepsilon^0\} \\ \{\kappa^0\} \end{array} \right\} \tag{2.13}$$

$$A_{ij} = \sum_{k=1}^{N_{\text{plies}}} \left(\bar{Q}_{ij}^{(k)} \left(z_k - z_{k-1} \right) \right) \tag{2.14}$$

$$B_{ij} = \sum_{k=1}^{N_{\text{plies}}} \frac{1}{2} \left(\bar{Q}_{ij}^{(k)} \left(z_k^2 - z_{k-1}^2 \right) \right) \tag{2.15}$$

$$D_{ij} = \sum_{k=1}^{N_{\text{plies}}} \frac{1}{3} \left(\bar{Q}_{ij}^{(k)} \left(z_k^3 - z_{k-1}^3 \right) \right) \tag{2.16}$$

$$\bar{Q}_{ij}^{(k)} = \left([T]^{(k)} \right)^{-1} [Q]^{(k)} [L] [T]^{(k)} [L]^{-1} \tag{2.17}$$

$$[T]^{(k)} = \left[\begin{array}{ccc} c^2 & s^2 & 2cs \\ s^2 & c^2 & -2cs \\ -cs & cs & c^2 - s^2 \end{array} \right]^{(k)} \quad \text{with} \quad \begin{cases} c = cos(\theta) \\ s = sin(\theta) \end{cases} \tag{2.18}$$

$$[L] = \left[\begin{array}{ccc} 1 & 0 & 0 \\ 0 & 1 & 0 \\ 0 & 0 & 2 \end{array} \right] \tag{2.19}$$

$$[Q]^{(k)} = \left[\begin{array}{ccc} \frac{E_1}{1-\nu_{12}\nu_{21}} & \frac{\nu_{12}E_2}{1-\nu_{12}\nu_{21}} & 0 \\ \frac{\nu_{12}E_2}{1-\nu_{12}\nu_{21}} & \frac{E_2}{1-\nu_{12}\nu_{21}} & 0 \\ 0 & 0 & G_{12} \end{array} \right]^{(k)} \tag{2.20}$$

A methodology to determine the ABD-matrix could be to analyse the stress-strain and moment-curvature diagrams of the drop-stitch panel in different directions at different locations. Liew et al. [83], have analysed moment-curvature-thrust relationships for inelastic and geometrically non-linear structural problems involving a combined axial load and bending. The thrust is the axial load. They described the relation between external applied moment M and internal resting moment $\bar{E}I\kappa$ by the differential equation 2.21. In this equation $\bar{E}$ is the effective Young's modulus, which is described by adopting a bi-linear material model, κ_n the large deflection curvature and I the moment of inertia. Although this model is meant for concrete beams, two dimensional beam models and a different load case, the methodology to use an effective Young's modulus could be adopted to include wrinkling. Due to wrinkling, the bending stiffness decreases, which could be done by decreasing the effective Young's modulus. The effective Young's modulus needs to be determined by establishing a relationship between curvature, strain and Young's

modulus. Ibrahim et al.[84] has used an effective moment of inertia instead of a effective Young's modulus to describe non-linear bending behaviour of cracked concrete walls. A local crack in a concrete beam would decrease the effective thickness that could be used to take stresses. Wrinkling, which is expected to be one of the main non-linear components of the moment-curvature-diagram, influences the local material properties in the wrinkling direction. It would be incorrect physically to implement an effective thickness in the stiffness matrix, since the thickness that could take stresses does not decrease. Using an effective Young's modulus would be more appropriate than an effective moment of inertia.

$$\bar{E}I\kappa = \bar{E}I\frac{\frac{\mathrm{d}^2 v}{\mathrm{d}x^2}}{\left[1 + \left(\frac{\mathrm{d}v}{\mathrm{d}x}\right)^2\right]^{\frac{3}{2}}} = -M \tag{2.21}$$

Wang [85, 86] has analysed the bending modulus of carbon nanotubes taking into account rippling deformations. Using a ninth-order polynomial, discrete points are fitted in the moment curvature diagram to capture the non-linear bending stiffness behaviour [86]. If a higher order polynomial would be implemented in the constitutive relation of the CLT (equation 2.13), it would change to a higher order polynomial as shown in equation 2.22 with i is the polynomial order.

$$\left\{ \begin{array}{c} \{N\} \\ \{M\} \end{array} \right\} = \left[\begin{array}{cc} [A_1] & [B_1] \\ [B_1] & [D_1] \end{array} \right] \left\{ \begin{array}{c} \{\varepsilon\} \\ \{\kappa\} \end{array} \right\} + \left[\begin{array}{cc} [A_2] & [B_2] \\ [B_2] & [D_2] \end{array} \right] \left\{ \begin{array}{c} \{\varepsilon^2\} \\ \{\kappa^2\} \end{array} \right\} + \\ \left[\begin{array}{cc} [A_3] & [B_3] \\ [B_3] & [D_3] \end{array} \right] \left\{ \begin{array}{c} \{\varepsilon^3\} \\ \{\kappa^3\} \end{array} \right\} + ... + \left[\begin{array}{cc} [A_i] & [B_i] \\ [B_i] & [D_i] \end{array} \right] \left\{ \begin{array}{c} \{\varepsilon^i\} \\ \{\kappa^i\} \end{array} \right\} \tag{2.22}$$

The internal air pressure generates pretension in the fiber cloth. This pretension effect should be included as a residual stress/strain in the classical laminate theory, since it does affect the through thickness stress distribution and the wrinkling onset of the drop-stitch floater. Shokrieh et al. [81] mentioned a modified CLT, equation 2.23, which takes into account the residual strain ε^{res}. The total strains at any point may be related to laminate reference plane and curvature as equation 2.23. This formulation could be used to incorporate the prestrain caused by the internal air pressure.

$$\left\{ \begin{array}{c} \varepsilon_x^{(k)} \\ \varepsilon_y^{(k)} \\ \gamma_{xy}^{(k)} \end{array} \right\} = \left\{ \begin{array}{c} \varepsilon_x^0 \\ \varepsilon_y^0 \\ \gamma_{xy}^0 \end{array} \right\} + z \left\{ \begin{array}{c} \kappa_x \\ \kappa_y \\ \kappa_{xy} \end{array} \right\} - \left\{ \begin{array}{c} \varepsilon_x^{res} \\ \varepsilon_y^{res} \\ \gamma_{xy}^{res} \end{array} \right\} \tag{2.23}$$

2.5.4 Implementation of structural models on drop-stitch panels

The research that has been performed on implementing structural models on drop-stitch panels is limited. Structural models for high pressure, isotropic and linear tensile elastic inflatable panels have been derived using a Timoshenko beam model. Cavallaro et al. and Wielogsz et al. assumed a linear relation between bending load and deflection, so post-wrinkling deflections cannot be analysed with these structural models [24, 87]. Wielogz et al. [87] only studied low deflections (maximum is 8 cm) and linear deformations. Cavallaro et al. [24] used a simple approach, which effectively estimates the wrinkling loads. Cavallaro and Wielogz did not take into account the following influences: pressure volume work, wrinkling and the effect of the yarns. Davids et al. has included these influence using the Timoshenko beam model for a bending only load case [32, 88]. Each of these influences Davids et al. included are evaluated separately. They have assumed a linear elastic pure bending case, where the cross sectional area remains constant over the length of the beam. Also, small deformations and shear angles are assumed. The general virtual work equilibrium statement is given by:

$$\int M\delta\kappa\mathrm{d}x + GA_s \int \gamma\delta\gamma\mathrm{d}x + p \int \mathrm{d}(\delta\Delta V) = \int q\delta v \; \mathrm{d}x$$

The first two terms are the work due to bending and shear. The third term is the work done by the pressure-volume relation. The last term is the external work introduced by an external distributed load q. A brief description of how wrinkling, pressure-volume work and the yarns are implemented in the model of Davids et al., is described in the continuation of this section.

Wrinkling

Wrinkling has been included by assuming the beam as a tension only structure. A tension only structure that it cannot withstand compressive stresses, which is implemented by assuming for $\varepsilon > 0$ $\sigma = E\varepsilon$ and for $\varepsilon \leq 0$ $\sigma = 0$. The total strain at any point in the beam for a certain curvature κ can be determined by:

$$\varepsilon = \varepsilon_0 + \kappa(\bar{y} - y)$$

with $\bar{y}$ is the neutral axis as depicted in figure 2.16.
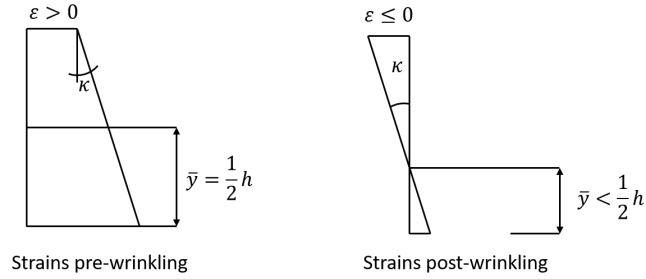
Figure 2.16: The through thickness strains at a certain curvature and pretension (adapted and reproduced) [88]

The force equilibrium can be used to determine $\bar{y}$ numerically by using a solver such as the Newton-Raphson solver. The horizontal force equilibrium is as follows:

$$\sum F = \int_A \sigma \mathrm{d}A - P = 0$$

with A is the cross sectional area and P is the force generated by the internal air pressure, which is $P = p\pi r^2$ for a cylinder and $P = p\left(\pi\left(\frac{h}{2}\right)^2 + hB\right)$ for an obround shape. If the $\bar{y}$ is known, the internal bending moment can be determined by:

$$M = \int_A \sigma(y - \bar{y})\mathrm{d}A$$

This internal bending moment does not include the bending moment the internal air pressure can withstand. So, the effective internal bending moment is determined by:

$$M_e = M + P(y - \bar{y})$$

Now the moments are known and a moment curvature relation can be established, which shows the influence of wrinkling in a pure bending load case, figure 2.17.

Pressure-volume work

It has been assumed that the pressure remains constant and the volume changes due to shear and bending rotations, which results in a pressure-volume work due to the changing volume. The total pressure volume work is the summation of the volume change due to shear and bending. Due to shear, the virtual volume change for small shear angles can be described as:

$$d(\Delta V)^s = Adx\left(\cos\left(\gamma\right) - 1\right) \approx -\frac{\gamma^2}{2}Adx$$
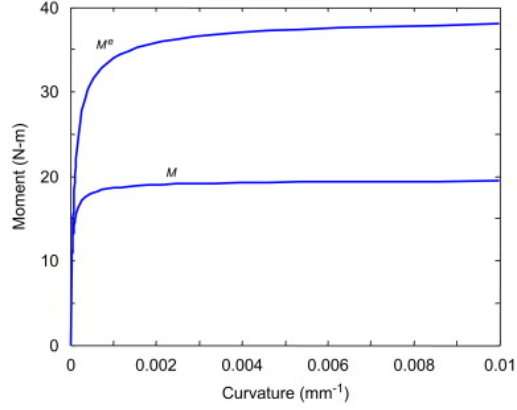
Figure 2.17: Moment curvature relation for an inflatable cylindrical tube with $p = 50$ kPa, $r = 50$ mm, $E = 0.625$ N/m [32]

The volume change as a result of the curvature is determined by:

$$d(\Delta V)^f = -A(y - \bar{y})\kappa dx$$

The total virtual pressure-volume work can now be expressed as a summation of the shear and curvature components:

$$d(\partial \Delta V) = d(\partial \Delta V)^f + d(\partial \Delta V)^s = -A(y - \bar{y}\partial \kappa + \gamma \partial \gamma)dx$$

Influence of the yarns

The yarns provide an additional shear stiffness besides retaining a flat shape. Figure 2.18 shows a sketch of the influence of the drop yarns, which is used to formulate a force equilibrium:

$$T \cos \gamma = PBdx$$

Using the force equilibrium statement, coupling between shear moment and amount of shear can be determined, which is used to define the additional shear stiffness generated by the yarns.

$$\frac{dM_\gamma}{dx} = PBh\gamma$$
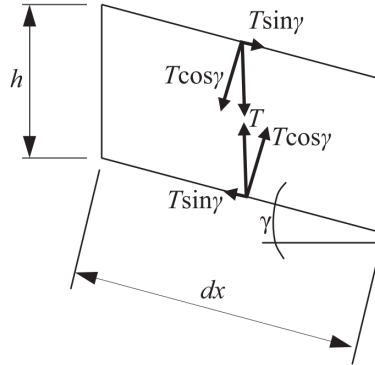
Figure 2.18: Kinematics of the yarns under shear deformation [32]

2.5.5 Concluding remarks

Different structural models could be adopted to model a drop-stitch panel. Most models of drop-stitch panels used a Timoshenko beam model. Davids et al. included the non-linear bending behaviour of drop-stitch panels. This gives some insight in the characteristics of drop-stitch panels, which are significant for the response. Davids et al. developed a structural model, which takes into account the non-linear bending response. The face sheets are assumed to be a tension only material, so it can not withstand compressive stresses due to wrinkling. Volume changes due to shear and curvature is taken into account in the total energy balance. The yarns add shear stiffness besides retaining a flat shape.

Chapter 3

Background of FE model

In this chapter, the theoretical background is given of the procedures and governing equations used in the `ABAQUS` FE model of the drop-stitch floater. This will provide a basic understanding of the procedures and their assumptions. Also the considerations of the procedures used in this research are evaluated. Only the governing equations of different procedures used in this research are discussed.[1] Unless otherwise mentioned, the equations stated in this chapter are from the `ABAQUS` manual [76]. Note that material models are discussed in chapter 5.

This chapter is subdivided into five sections: Section 3.1 elaborates on the used element and its assumptions; The implementation of the yarns is discussed in section 3.2; Section 3.3 discusses the modelling of the internal air pressure; The contact procedure used to model the three point bending load case is discussed in section 3.4; Section 3.5 evaluates the solver used for time integration.

3.1 Element

Keeping in mind the small thickness of the fabric, two element types are considered: shell and membrane elements. Shell elements can be used to model structures in which one dimension, the thickness, is significantly smaller than the other dimensions [76]. Membrane elements are used to represent thin elements that offer strength in the plane of the element, but have no bending stiffness. The bending stiffness of the fabric is small due to its thickness, so it might be neglected. Hulton et al used membrane elements to model a drop-stitch panel to perform a modal analysis [31]. However, they did not take into account wrinkling. It is expected that the bending stiffness can not be neglected for the wrinkling initiation and propagation [89, 90], so shell elements are adopted. The effect of bending stiffness on the wrinkling initiation and propagation is further evaluated in chapter 6. Quadratic shell elements might cause slower convergence rates in models involving contact than linear shell elements [76]. To prevent slow convergence rates, linear elements are adopted.

Linear shell elements are three dimensional elements with a plane stress conditions, $\sigma_{33} = 0$. For linear elastic isotropic shell elements the change in thickness is a function of the Poisson's ratio ν and the in-plane strain:

$$\varepsilon_{33} = -\frac{\nu}{1-\nu} \left(\varepsilon_{11} + \varepsilon_{22} \right) \tag{3.1}$$

For hyperelastic materials, `ABAQUS` assumes the material is incompressible, which implies that the multiplication of the principal stretches in the three directions should be equal to 1, $\lambda_1 \lambda_2 \lambda_3 = 1$. In the through thickness direction, two integration method are considered: the Simpson rule or the Gauss quadrature integration method. Gauss quadrature integration requires less integration points than the Simpson rule for a certain polynomial order of integration and is therefore chosen. To integrate linearly over the through thickness direction, two integration points for the Gauss quadrature method and three for the Simpson rule are needed.

---

[1]For the readers interested in the numerical implementation or the derivation of the mentioned equations, it is suggested to read the `ABAQUS` theory guide [76] or the references mentioned in this chapter.

(a) S4R element   (b) S4 element

Figure 3.1: A depiction of the integration points of fully integrated linear shell element (S4) and reduced integrated shell element (S4R) [76].

Shell elements in the in-plane direction can be fully or reduced integrated as shown in figure 3.1. Reduced integration reduces the amount of integration points. However, this could result in hourglassing. Hourglassing is a phenomenon where a shell element fails to detect strain [91]. It remains strainless in certain deformation modes as shown in figure 3.2. This results in a sort of zigzag pattern, which has the length of one element. Fully integrated linear shell elements on the other hand could have issues with a phenomenon known as shear-locking. The straightness assumption of the edges of a linear elements assumes an element does not have any curvature [92]. It tends to model a linear element subjected by a bending moment too stiff as shown in figure 3.3. Reduced integrated shell elements are chosen in this research to reduce the amount of DoF and computational time. This does imply that hourglassing effects should be kept in mind.
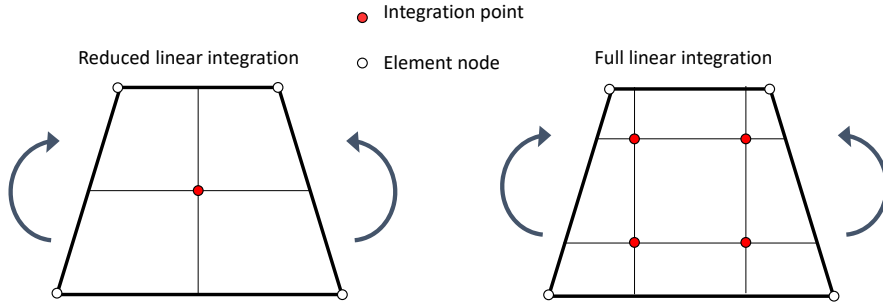
Figure 3.2: A depiction of a fully and reduced integrated shell element subjected by a moment. The reduced integrated shell element fails to notice a shear strain, since the change in length of the line from the integration point to the edge is zero. This phenomenon is called hourglassing.
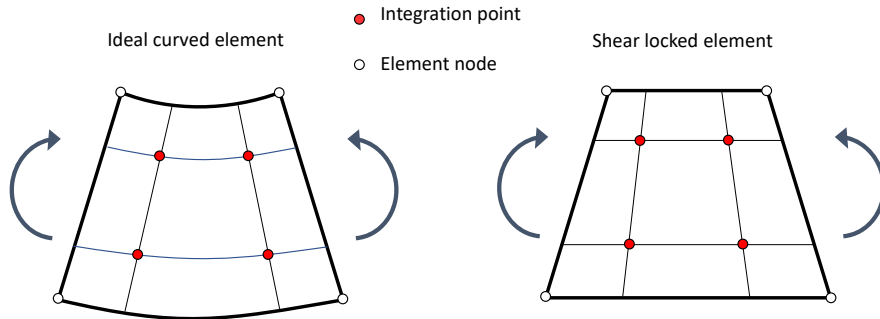
Figure 3.3: A depiction of a fully shell element subjected by a moment. Due to the straightness assumption of the edges, the element tends to be too stiffly modelled. This is called shear locking.

3.2 Yarns

For the yarns, two procedures can be used: mesh (in)dependent fasteners with axial connector elements; truss elements as Hulton et al did [31]. Both can only translate in the axial direction and do not have any bending stiffness. Truss elements need to be meshed, though axial connectors do not. In this research axial connectors are used to model the yarns. Axial connectors are connectors with a single degree of freedom, 3.4. The length of the axial connectors with $\mathbf{x}_a$ and $\mathbf{x}_b$ are the nodal coordinates is defined as:

$$l = \|\mathbf{x}_b - \mathbf{x}_a\|$$

The current length l is subtracted by the reference length l_{ref}, which is the initial length, to determine the displacement:

$$u_1 = l - l_{ref}$$

The axial force in one axial connector is defined as:

$$\mathbf{f}_{axial} = f_1 \mathbf{q}, \quad \text{where} \quad \mathbf{q} = \frac{1}{\|\mathbf{x}_b - \mathbf{x}_a\|} (\mathbf{x}_b - \mathbf{x}_a)$$

The force and displacement are assumed to be linearly related, which assumes a linear isotropic material for the yarns.

$$f_{axial} = D_{11} u_1 \text{ where } D_{11} = \frac{EA}{l_1^{ref}} \tag{3.2}$$

where E is the Young's modulus of the yarns and A the cross-sectional area of the yarns. The hyperelastic behaviour of the polyester yarns is not taken into account. The material stiffness of the yarns mainly affect the eventual thickness of the drop-stitch panel and shear stiffness [32]. Hyperelasticity could influence the eventual thickness, since a constant Young's modulus can not be assumed. However, if the yarn spacing is small, the strain within the yarns will decrease, which reduces the influence of the hyperelasticity. One yarn can easily buckle, so the compressive stiffness is expected to be negligible.

If one would use axial connector elements, one could use a mesh dependent or independent grid for the attachment points of the axial connector elements. The attachment points connects the axial connector elements to the face sheets. It could coincide with the nodes of the mesh or not. If one would use a mesh independent fastener, a grid of attachment points are projected on the upper and lower face sheets of the drop-stitch floater, which results in fastening points as shown in figure 3.5. Between those projected attachment points, an axial connector element is modelled. A linear weighting method is used to smear out the coupling constraints of the mesh independent fastener. It couples the nodes of the shell elements with the attachment points. Hourglassing issues arised when imposing a mesh dependent attachment grid, which could be due to the fact that the coupling between the axial connector and a shell element is strictly at one node. By smearing the coupling out over multiple nodes, hourglassing issues might be solved.
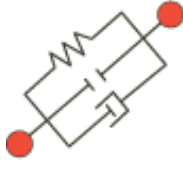
Figure 3.4: Depiction of an axial connector element between two points a and b [76].
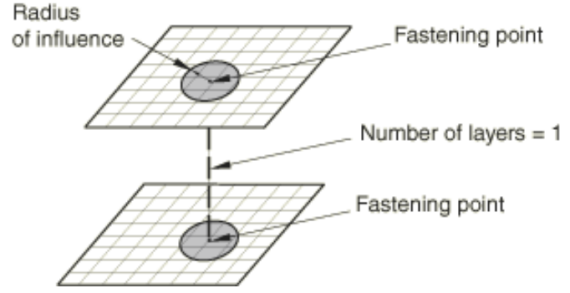
Figure 3.5: The fastener configuration [76].

3.3 Internal air pressure

The surface based hydrostatic fluid cavity models the air chamber within a drop-stitch panel. An ideal isothermal gas has been assumed. ABAQUS' fluid cavity procedure creates hydrostatic fluid elements, also named F3D4/F3D3 elements, between the cavity reference node and shell elements as shown in figure 3.6 assuming a pyramid shape between an shell element and the fluid cavity reference node. The ideal gas equation is given as:

$$P + P_A = \rho R_{gas} \left(T - T^Z \right) \tag{3.3}$$

where P is the gauge pressure, P_A the atmospheric pressure, ρ the density of the fluid, R_{gas} the gas constant, T the current temperature and T^Z the absolute zero temperature. The gas constant is defined as:

$$R_{gas} = \frac{\widetilde{R}}{MW}$$

with $\widetilde{R}$ is the universal gas constant and MW the molecular weight. The actual volume of the fluid cavity V should be equal to the volume derived from the pressure, temperature and mass $\overline{V}$:

$$V - \overline{V}\left(P, T, m \right) = 0$$

From equation 3.3, the volume pressure relation is derived:

$$\frac{d\overline{V}}{dP} = -\frac{m}{\rho^2}\frac{d\rho}{dP} = -\frac{mR_{gas}\left(T - T^Z \right)}{\left(P + P_A \right)^2}$$

Fluid mass can be inserted into or extracted out of the fluid cavity, which is used to describe the volume changes:

$$\Delta \overline{V}(P, T) = \Delta m / \rho(P, T)$$

The actual volume V is the summation of the volume of the hydrostatic fluid elements (F3D4/F3D3 elements), figure 3.6. From the cavity reference node, an F3D4/F3D3 is projected on a shell element facet. It has pyramid shape, which is used in the actual volume integration of the fluid cavity. The volume of one F3D4 element becomes:

$$V^e = \int_{V^e} dV = \int_{-1}^{+1} \int_{-1}^{+1} \frac{1}{3} \left(\mathbf{x}_R - \mathbf{x} \right) \cdot \left(\frac{\partial \mathbf{x}}{\partial g} \times \frac{\partial \mathbf{x}}{\partial h} \right) dg dh$$

with $\mathbf{x}_R$ is the position of the fluid cavity reference node, $\mathbf{x}$ the nodal coordinates and g and h are the parametric coordinates. $\left(\frac{\partial \mathbf{x}}{\partial g} \times \frac{\partial \mathbf{x}}{\partial h} \right)$ is the normal direction of the base of the F3D4 element. The pressure-volume work is then included in the virtual work equilibrium.
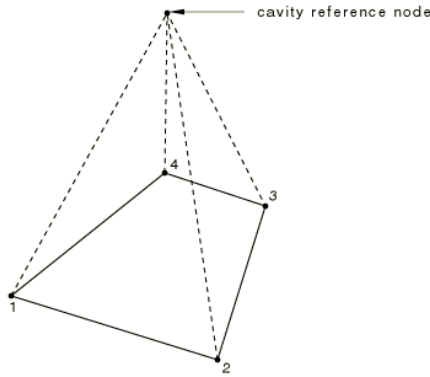
Figure 3.6: Hydrostatic fluid element (F3D4) [76]

3.4 Contact

A hard contact between the drop-stitch floater and the support/load beam has been defined with finite sliding. A contact interaction procedure is chosen instead of a line load/displacement, since the contact area due to compression of the drop-stitch panel and low bending stiffness of the fabric changes. Defining a line load/displacement on the face sheet would introduce a singularity at the transition region from fabric to closing edge. The pressure on the beams $p_{contact}$ is a function of the overclosure h_{oc}, which is the interpenetration of the beams and the drop-stitch floater. If there is a distance between the beam and the floater, h_{oc} is less than zero, so the following conditions are used:

$$p_{contact} = 0 \quad for \quad h_{oc} < 0 \quad (open), \quad and$$
$$p_{contact} > 0 \quad for \quad h_{oc} = 0 \quad (closed).$$

A surface-to-surface contact discretisation has been used to determine the locations and conditions of the contact between the analytical rigid beams of the load/support beam and shell elements of the drop-stitch floater. It improves the contact pressure accuracy in some cases compared to node to surface discretisation by averaging the contact conditions over regions of the nearby slave nodes. A node-to-surface discretisation procedure enforces the contact conditions at individual nodes.

The state-based tracking algorithm is used, since it is the only tracking algorithm available for finite sliding contact interaction with analytical rigid surfaces in `ABAQUS`. Tracking algorithms are needed to calculate the relative motion between different bodies and determine whether a slave element is in contact with the master surface. The contact pressure interpenetration work is included in the virtual work equilibrium.

3.5 Solver

For the three point bending load case, a static or a quasi-static dynamic solver could be adopted. In static solvers, the kinetic energy is assumed to be zero and in quasi-static dynamic solvers the kinetic energy is minimised. It might be difficult to obtain a static solution if there is a sudden shift in stiffness due to wrinkling. A quasi-static dynamic solver is therefore chosen in this research.

Dynamic solvers can be divided in explicit and implicit solvers. Explicit determine values at $t + \Delta t$ solely based on the values at t in which t is a time and Δt a time increment [76]. Implicit solvers obtain values at $t + \Delta t$ based on quantities at t and $t + \Delta t$. Explicit solvers generally need smaller time increments to obtain a stable result than implicit solvers and are conditionally stable, which

means that there are certain conditions for time increments. In `ABAQUS`, the stable time increment is determined by dividing the characteristic element length L_e with the dilatational wave speed c_d [76]:

$$\Delta t = \min\left(\frac{L_e}{c_d}\right) \tag{3.4}$$

The dilatational wave speed per element is determined by:

$$c_d = \sqrt{\frac{(\hat{\lambda} + 2\hat{\mu})}{\rho}} \tag{3.5}$$

with $\hat{\lambda}$ and $\hat{\mu}$ are the effective Lamé's constants and ρ is the density. $\hat{\lambda}$ and $\hat{\mu}$ are determined each user defined increment. Since the stiffness is strain-dependent for hyperelastic materials, it should be done multiple times within the simulation. If a material has a higher density or less stiffness, the dilatational wave speed decrease, which increases the stable time increment. Also, if one would use a coarser grid, the stable time increment decreases. This is a conservative estimate of the stable time increment, since boundary conditions and contact interaction can affect the the stiffness of the model and eventually the stable time increment.

Implicit solvers can use larger time increments and are unconditionally stable. They need to invert the global stiffness matrix [93], which can become computational intensive depending on the amount of DoF's. In this research `ABAQUS`' dynamic implicit solver is chosen. Generally, for static and low-frequency dynamic analysis a implicit solver is recommended [93, 94]. The quasi-static procedure of `ABAQUS` is adopted.

The main focus of `ABAQUS`' quasi-static dynamic implicit solver is a final static response by regularising unstable behaviour by introducing inertia effects. If possible, large time increments are taken to minimise computation time. Every iteration, the half increment residuals are checked to determine whether a cutback in time increment needs to be performed or not. It is checked a posteriori that the kinetic energy is insignificant compared to the total energy to ensure the solution is quasi-static. As rule of thumb, the amount of kinetic energy should be atleast less than 10% of the strain energy [75]. The dynamic implicit solver of `ABAQUS` is based on methodologies introduced by Hibbit and Karlsson [95] and Hilber et al [96, 97].

Three Point Bending Test

A three point bending test has been conducted to get insights in the bending characteristics of a drop-stitch floater and the maximum load that could be applied at low internal air pressures. The maximum load is the load at which the structure fails to resist the applied load and collapses. At the failure load, the bending stiffness is too small to resist the exerted load.

The test setup is discussed in section 4.1. In section 4.2, the performed measurements and results are evaluated. The conclusion of these experiments is shown in section 4.3. Note that in appendix A, a table with the performed measurements and measured deflections are shown.

4.1 Test setup

A drop-stitch floater is placed on two supports, which are placed with a 3.05 m offset from the edges and has a height of 0.903 m as shown in figure 4.1. Its dimensions are $13 \times 7.1 \times 0.335$ m (L×B×H). For the support and load lines, trusses are used. The truss weights 51 kg and the drop-stitch floater itself 346 kg. On top of the load truss, an equal number of weights are placed on both sides of the floater. The deflection is measured using a gauge rods every metre between 0.5 and 12.5 m as shown in figure A.1. The internal air pressure is regulated and checked every measurement with a pump and pressure gauge. The effect of hysteresis is measured by performing one load and unloading measurement to evaluate the difference between both pathways.
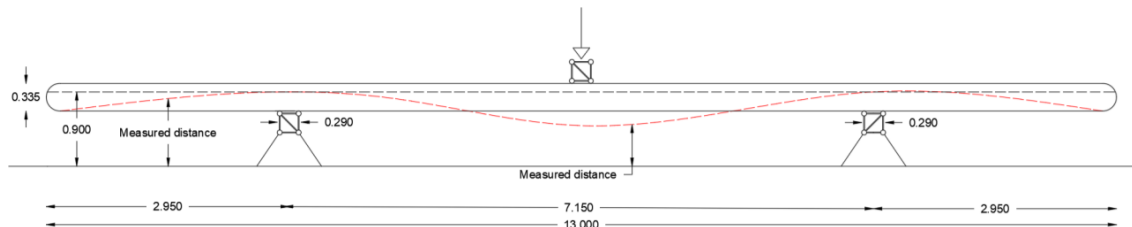
Figure 4.1: A schematic drawing of the three point bending tests setup. The floater is supported by two trusses over the entire width. The mid span load is also exerted over the entire width by adding weights on top of the mid span truss. (courtesy of TNO).

For five different internal air pressure, the deflections are measured, which are shown in table A.1 in appendix A. As the internal air pressure increases, the floater became stiffer due to an increased pretension, which is in correspondence with prior research [24, 32, 38, 88]. So, more weight needs to be applied to analyse the deflections around the maximum load. The measured weights are also shown in table A.1. The panel is unloaded from the largest load to zero load. Note that all the loads including zero load consists of a gravity and support load.

4.2   Results

The measured deflection over the length of the drop-stitch floater at different air pressures and loads is shown in appendix A. The midspan force displacement curves for different air pressures is shown in figure 4.2. The measurements were performed until the panel collapsed except for the 20 kPa internal air pressure load case. So, the experimental maximum load of the 20 kPa load case is unknown. Figure 4.2 also shows that the initial deflection due to gravity decreases with higher internal air pressure. Also, the stiffness at higher internal air pressures increases. At the maximum applied load, a clear wrinkle over the full width was observed as shown in figure 4.4. The measuring point of P=7 kPa at 500 N shows different behaviour. The difference in deflection between a load 500 N and 0 N is much smaller compared to higher internal air pressures, which can also be seen in figure A.2. This behaviour could be due to measuring inaccuracy or the tangential friction of the supports. The tangential friction is larger at lower air pressures, since the panel becomes more flexible. This results in a larger contact area at the supports, which increases the tangential friction eventually.
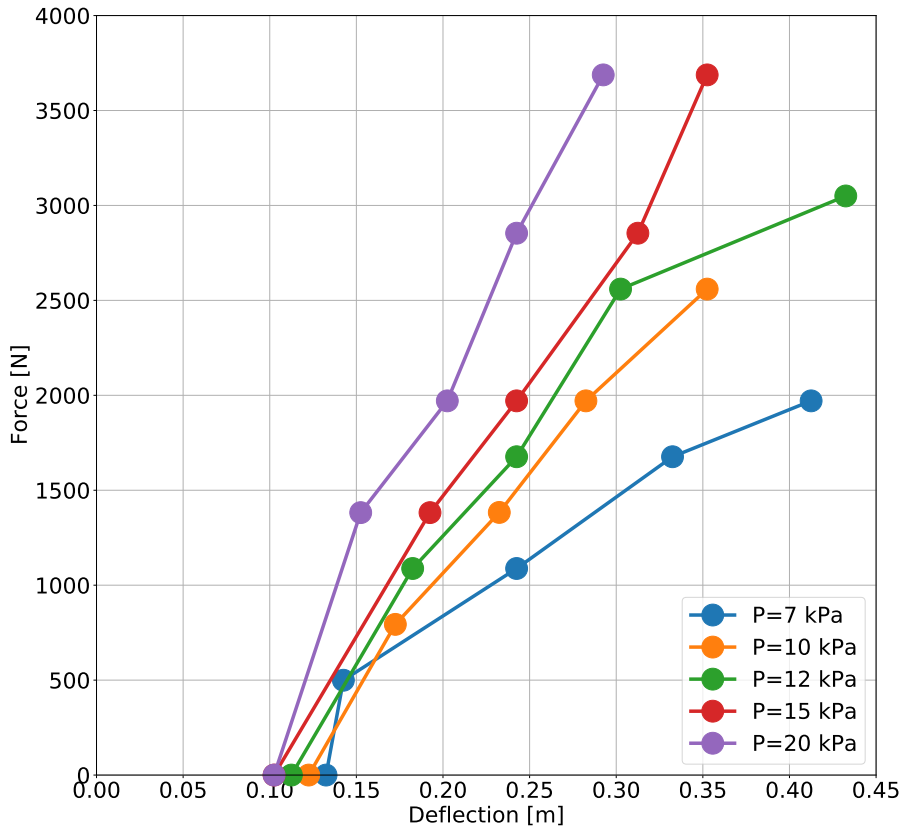
Figure 4.2: The force deflection curves for the load controlled three point bending experiment with 7, 10, 12, 15 and 20 kPa air pressure. The deflection is measured midspan. An initial deflection is caused by the gravity load.

Figure 4.3 shows the loading and unloading path. The loading and unloading path of the three point bending test is not the same, which suggests that there is a hysteresis effect, figure 4.3. It is expected that the tangential friction between the trusses and panel causes a hysteresis effect. The maximum difference between the loading and unloading path is 4 cm, which is at 260.9 kN in the middle of the panel.
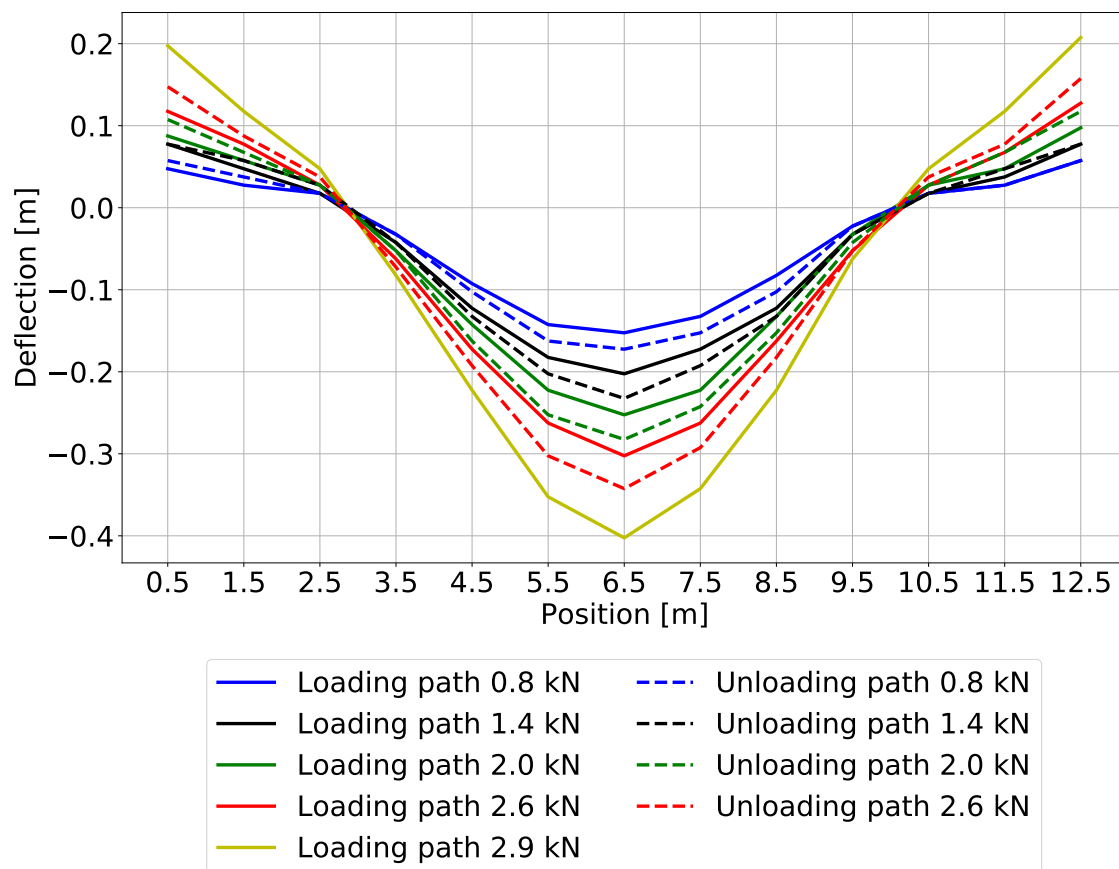
Figure 4.3: Hysteresis effect of loading and unloading path for an internal air pressure of 10kPa

4.3 Conclusions

A decrement in bending stiffness at high deflections is observed, which is in accordance with the expectations based on prior research. For increasing air pressure, the bending stiffness and maximum load increases of the drop-stitch panel. Also, at large deflections a clear wrinkling pattern can be distinguished over the full width as shown in figure 4.4. A local change in curvature is observed in figure 4.4 due to a local change in stiffness, which suggests that the the bending stiffness of the face sheets can not be neglected for the post wrinkling behaviour. Assuming membrane elements, which neglects the bending stiffness, as Hulton et al [31] used in their drop-stitch FEM model to perform a modal analysis, is insufficient for analysing the post wrinkling structural response of drop-stitch panels subjected to a load case. Note that this does not imply that membrane elements are incorrect for the modal analysis performed by Hulton et al [31], since their research was in the pre-wrinkling phase. The performed experiments will be used to validate the FEM model of chapter 6. There are some remarks on these experiments:

- The effect of hysteresis affects the response of the drop-stitch floater. A maximum difference in deflection between the unloading and loading path of 4 cm was observed, which is quite significant compared to a maximum deflection 35-40 cm. To minimise the effects of hysteresis, roller supports should be used or a lubricant to reduce the tangential friction of the supports on the floater. For the validation of the simulations of the drop-stitch panel, the tangential friction of the support and loads should be taken into account.

- A displacement controlled three point bending experiment could be used to analyse the wrinkling behaviour more thoroughly. It would give data for a larger set of displacements,

which could be used to get more insight in the post-wrinkling phase and eventual failure mechanism. Due to the size of the panel, a load controlled three point bending test has been performed, since it required a smaller test setup than a displacement controlled three point bending test.

- The deflections are measured by using gauge rods which resulted in a measuring accuracy of ± 1 cm. Using a distance measurer or digital image correlation could give better results. Due to the size of the floater, digital image correlation might be difficult, since it could introduce 3D effects. On the other hand, DIC gives the possibility to analyse the full displacement field including the wrinkles, which might be interesting for further analyses of the failing mechanism.
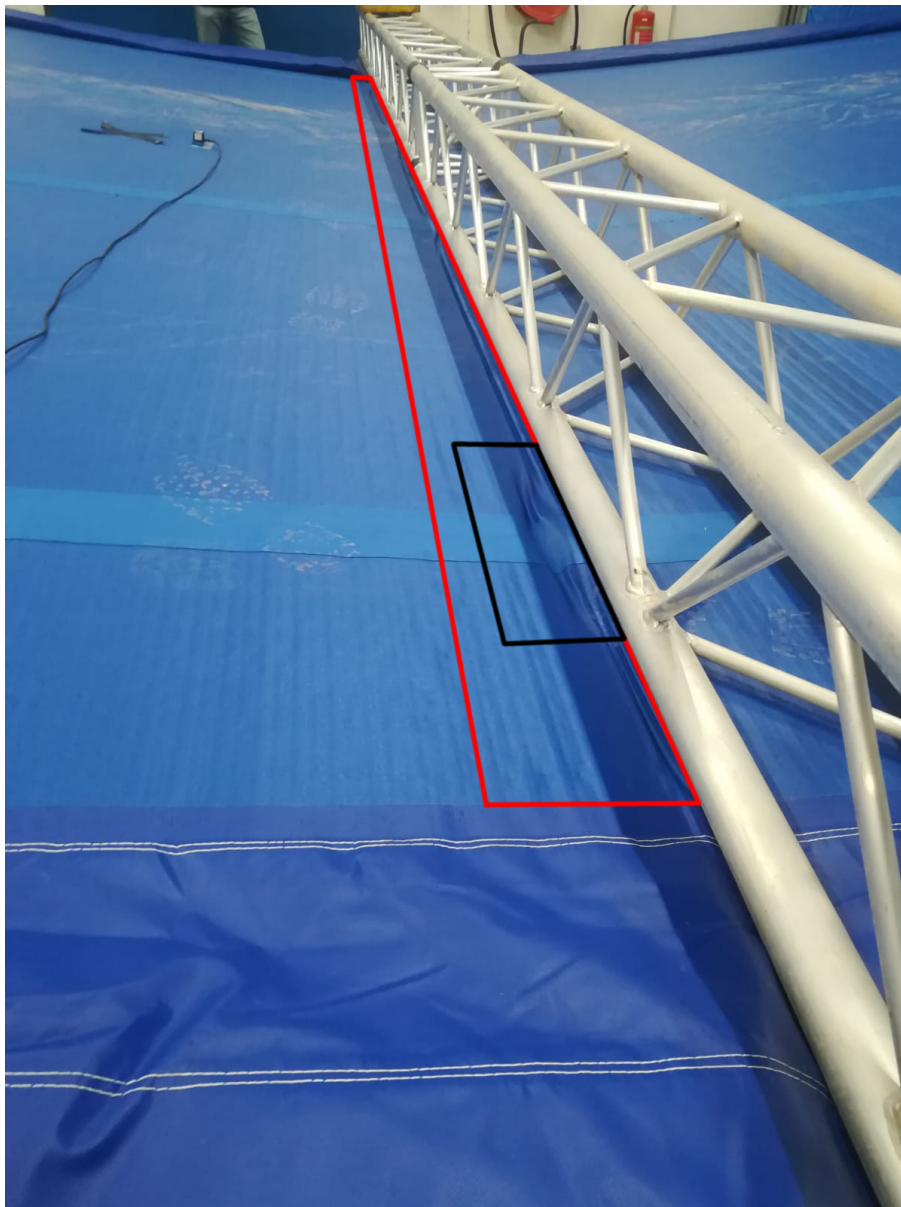
Figure 4.4: A photograph of the wrinkles that arose over the width of the drop-stitch panel. The red boxed area marks the wrinkles. The black boxed area shows a change in wrinkling induced curvature due to a strip, which locally increases the bending stiffness of the face sheets.

Material model

As mentioned in section 2.1, there are multiple non-linearities that influence the structural response in drop-stitch floaters of which the material non-linearity could be one. Describing the material elasticity correctly of polyester fiber coated with PVC could be more complex, if hyperelasticity is significant for the global response of a drop-stitch panel. The influence of hyperelasticity has not been investigated yet in prior researches on drop-stitch panels.

The effect of material hysteresis is not taken into account, since it is strain rate dependent. For (quasi-)static load cases, the strain rate is (close to) zero and the effect of material hysteresis is negligible. If one would perform dynamic simulations, material hysteresis might be considered. The asymmetric layup of the face sheets causes an out of plane deformation. If a tensile load is applied on a composite with an asymmetric layup, shear deformations occur. The out-of-plane deformations of the drop-stitch panel's face sheets are influenced by: the external loads, vertical threads, air pressure and out of plane shear deformation introduced by the asymmetric layup. For the global response of the drop-stitch panel, shear deformations due to a asymmetric layup are expected to have negligible influence on the response. The other out-of-plane deformation components of the face sheets cause significantly higher out-of-plane deformations. For the quasi-static calculations of this thesis, low strains are expected around 2.5%, which is comparable with the strain range considered by Davids et al. [32]. This expectancy is evaluated in chapter 6. This will be within the elastic region, so plastic deformations are not examined.

An uniaxial tensile test in different specimen direction for the face and edge fabric using the strip method following the ASTM standard D 3039/D 3039M and D3518 /D3518M has been performed [98, 99]. The yarns or the vertical threads are cutted of the face sheets to disconnect the upper and lower face sheet. Different hyperelastic material models are evaluated. A least-square fitting approach is used to determine the variables of the hyperelastic material model.

The setup and results of the uniaxial tensile tests are discussed in section 5.1. Different material models are evaluated and fitted using the measurement data in section 5.2.

5.1   Uniaxial tensile tests

The goal of these experiments is to establish the force-displacement curves of the polyester fabric coated with PVC, which can be used to determine the material properties of a hyperelastic material model. Biaxial/uniaxial tensile, grab and bursting tests are common procedures [100] to determine the material properties of a composite/fabric. Also more innovative methodologies such as ultrasonic guided waves might be an option to determine the material properties [101].

In this thesis an uniaxial tensile test using the strip method has been performed due to the availability of an uniaxial tensile machine. The tests will be performed following the ASTM standard D 3039/D 3039M [98] for the in-plane principal tensile properties and D3518 /D3518M [99] for in-plane shear properties. HEYtex provided material samples of the face sheets and closing edges, figures 5.1 and 5.2. The face sheet has an average thickness of 0.7 mm and the closing edge 0.6mm. Note that the double weave creates an irregular surface, so the thickness differs slightly over the surface, but that has not been evaluated in this research.

Polyester fiber coated with PVC is a composite material consisting of: a polyester fiber layer, which has a weave, weft and yarn direction, and a PVC layer. The face sheets and closing edge as depicted in figure 2.3 are fabricated from two different types of layup: The face sheets are coated with PVC on a single side and the closing edges on both sides. The fiber material of the face sheets and closing edges used in this research are shown in figures 5.1 and 5.2. The PVC layers are used to keep the drop-stitch floater airtight.

The test methodology is discussed in section 5.1.1. The results of the experiments are shown in section 5.1.2. Finally, the conclusion of the experiments is evaluated in section 5.1.3

Figure 5.1: Sample material of the face sheets
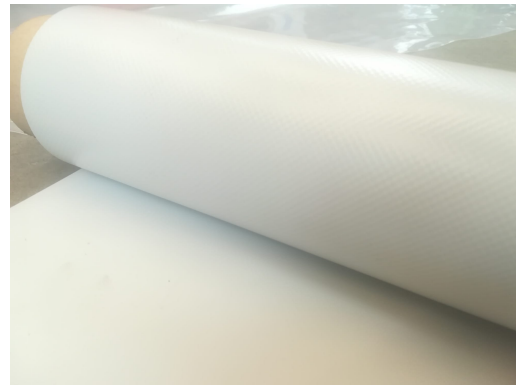
Figure 5.2: Sample material of the closing edges

5.1.1 Methodology

An Instron 8854i MT 250 kN/2000 Nm axial/torsion apparatus is used. Rectangular strips of 250 mm × 25 mm are used as specimens. The remnants of the yarns in the face sheets are left within the specimens of the face sheet. Since the minimum gripping thickness was larger than the specimen thickness, aluminium plates were placed between the grips and the specimens, figure 5.3. The lower grips remained static and the upper grips moved upwards. The distance between the grips was 155mm. According to the ASTM standard D 3039/D 3039M a tensile test should take between 1 to 10 minutes from start to failure of specimen to ensure the experiments are within the quasi-static regime. A displacement rate of 0.2 mm/s is used to ensure the testing time is within that range. Five specimens are tested for each specimen direction (0, 45, 90 degrees) and each material type (face sheet/edge). The specimens are cut by hand with scissors. A list of the specimen numbers and their respective specimen direction and material type is shown in table B.1 in appendix B.
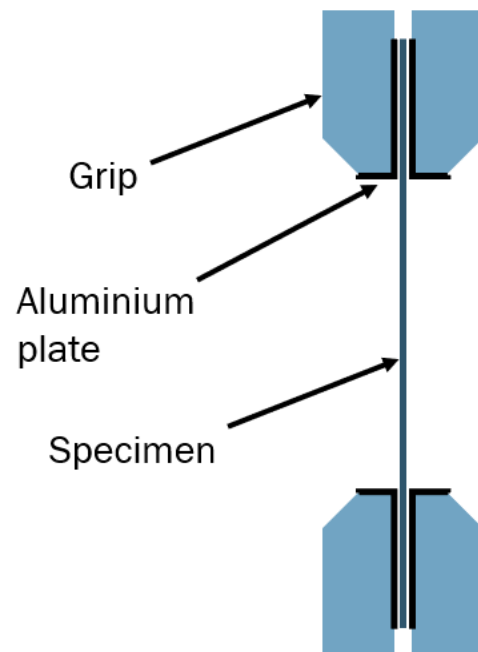
Figure 5.3: Sketch of test setup of the uniaxial tensile test.

5.1.2 Results

The raw data of the experiments is shown in figures B.1-B.6 in appendix B. This already shows that the force-displacement behaviour is non-linear. The raw data contains noise, which needs to be reduced to determine an average force-displacement curve per specimen direction for the face sheets and closing edges to fit the material models. Also, the raw data is translated to filter the region where the specimen is slack and set at 0 kN as initial condition.

The Savitsky-Golay filter of the `Python Scipy` package has been used to reduce the noise of the output signals [102]. It fits a polynomial curve within a window range using a least-square procedure [103]. The force values of all the specimens per specimen direction and edge/face material are averaged at every displacement value to get an average force-displacement curve.

The results of the specimens are shown in figure 5.4. Figures 5.4a-5.4c shows the filtered results of the face sheet material and 5.4d-5.4f of the edge. It clearly shows that within the aforementioned strain range of 2.5%, which is around 4 mm displacement assuming a gauge length of 155mm, the stress-strain behaviour in the 0° and 90° specimen direction are non-linear. In the 45° specimen direction, the stress-strain behaviour is close to linear for the face sheets and closing edges. Also, the force observed in the 45° specimen direction for the face sheets and closing edges is relatively low in the strain range considered in figures 5.4a-5.4f compared to the 0° and 90° specimen direction. This indicates that the in-plane shear stiffness might be low. Specimen 9 showed different behaviour in the 90° specimen direction of the face sheet than other specimens in the respective direction and fabric.
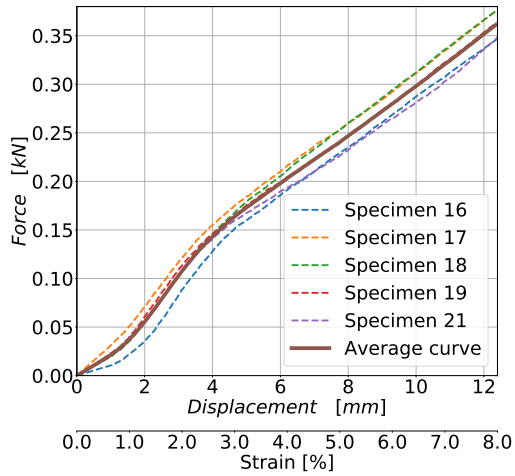
(a) Force-displacement results for face sheet fabric in 0° specimen direction. The dashed lines are the filtered curves of each specimen and the solid line is the average of the specimens.
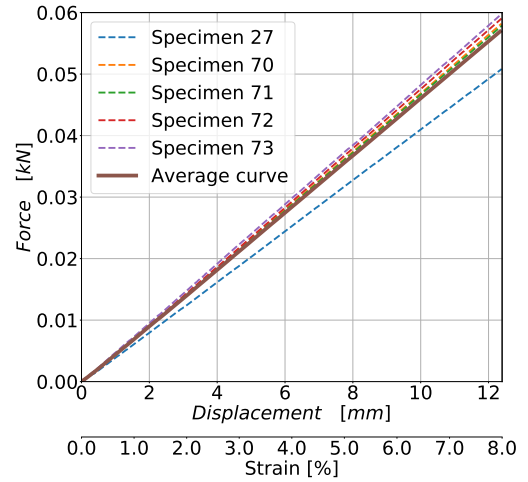
(b) Force-displacement results for face sheet fabric in 45° specimen direction. The dashed lines are the filtered curves of each specimen and the solid line is the average of the specimens.
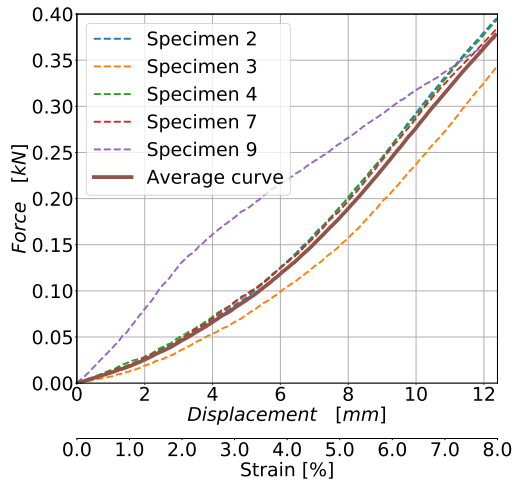
(c) Force-displacement results for face sheet fabric in 90° specimen direction. The dashed lines are the filtered curves of each specimen and the solid line is the average of the specimens. Note that specimen 9 showed completely force-displacement behaviour than the other four specimens, which suggests that it is an outlier and it is not taken into account for the average curve. The reason for the difference in stress-strain behaviour is unknown.
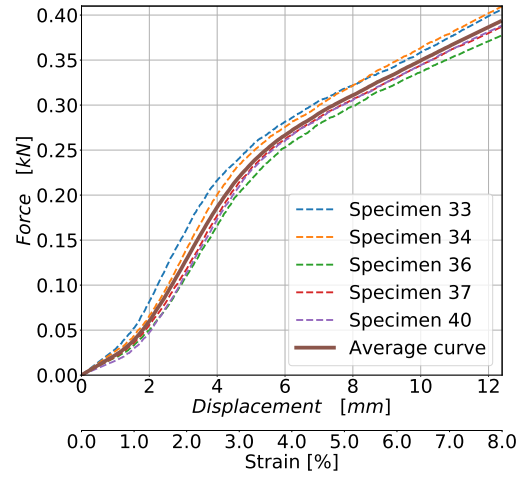
(d) Force-displacement results for edge sheet fabric in 0° specimen direction. The dashed lines are the filtered curves of each specimen and the solid line is the average of the specimens.
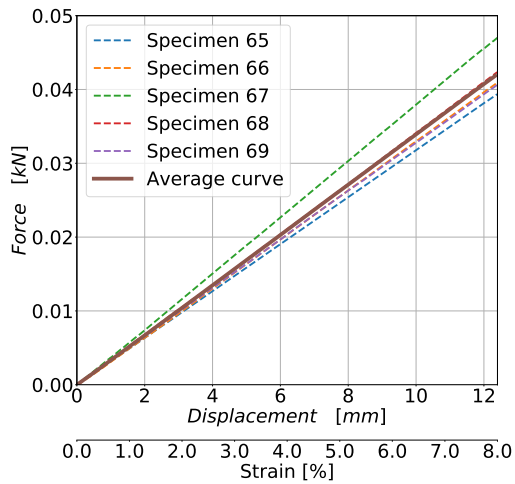
(e) Force-displacement results for edge sheet fabric in 45° specimen direction. The dashed lines are the filtered curves of each specimen and the solid line is the average of the specimens.
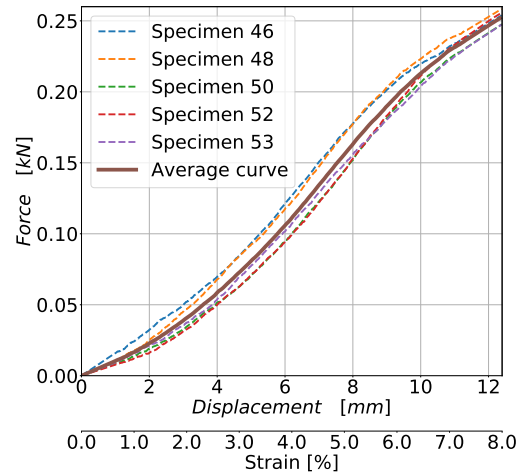
(f) Force-displacement results for edge sheet fabric in 90° specimen direction. The dashed lines are the filtered curves of each specimen and the solid line is the average of the specimens.

Figure 5.4: The filtered force-displacement curves per specimen direction for the face sheets and closing edges. The (nominal) strain is determined by $\varepsilon = u/L_0$ with u is the displacement and L_0 the gauge length.

5.1.3 Conclusion

The goal of these experiments to get more insight in the force-displacement of the polyester fiber coated with PVC and establish a force-displacement curve, which can be used to fit material models. Rectangular strips are cut out of the face sheet and closing edge material in different specimen directions and an uniaxial tensile test has been performed. The force-displacement clearly shows that the face sheets and closing edges are hyperelastic and anisotropic. Since the fibers have a double woven orthotropic weaving pattern, orthotropic behaviour is assumed. The influence of hyperelasticity on the response of drop-stitch floaters should be investigated further. Low forces are observed in the 45° specimen direction, which suggest that the in plane shear stiffness is low compared to the in-plane stiffness in the weave and weft direction. There are some remarks on these results:

- The Instron 8854 MT 250 kN/2000 Nm axial/torsion apparatus is meant for larger steel specimens, which withstand much larger forces in the order of kilonewtons. It is harder to measure small load differences due to the sensitivity of the sensor. Especially in the 45° specimen direction, low forces are observed, which resulted relatively more noise compared to the other specimen directions. A smaller tensile machine meant for lower axial forces would be more appropriate to analyse the force-displacement behaviour in the order of newtons.

- It appeared to be difficult to properly align a flexible fabric vertically between the grips. This introduced out of plane deformations. The misalignment does influence the force-displacement behaviour. Usually, the procedure of a uniaxial tensile test for stiff specimens is to first clamp the specimen with lower grips and afterwards in the upper. This made alignment more difficult due to the flexibility of the fabric. Therefore, the specimen was clamped with upper grip and thereupon the lower grip. This solved some of the alignment issues, but not all of them as shown for an excessive misalignment case in figure 5.7. A lot of specimens broke near the grips, figure 5.6, which could indicate an alignment issues, too high grip forces or sharp edges at the grip according to ASTM standard D 3039/D 3039M [98]. Due to safety regulations, it was not possible to adjust the alignment by hand during the clamping procedure. A different type test setup could solve the misalignment issues. Another testing setup that is less prone to misalignment than an uniaxial tensile test is advised to use.

- According to Becarelli et al. [100] and Cavallaro et al. [24], a biaxial tensile test machine is preferred to characterise the biaxial material response due to biaxial loads. Such machine was not available during this research.

- The toe region (< 3 mm displacement) of the force displacement curve is difficult to describe for polyester fibers with a double weaving pattern. In the first few percentages of strain, the slack and alignment of the specimen is taken up and there are crimp effects. The initial curvature of the double weaving pattern of the polyester fiber is crimp as shown in figure 5.5 [104]. Due to a loading, the yarns will straighten and the curvature will decrease, which results in a higher stiffness. Quantifying the influence of crimp and slack/alignment taken up is difficult and is important to investigate to get a more accurate representation of the force-displacement curves at small displacements. A toe region compensation, as described in ASTM standard D638-14 meant for plastics, might be used, if it appears that the effect of crimp is negligible [105].
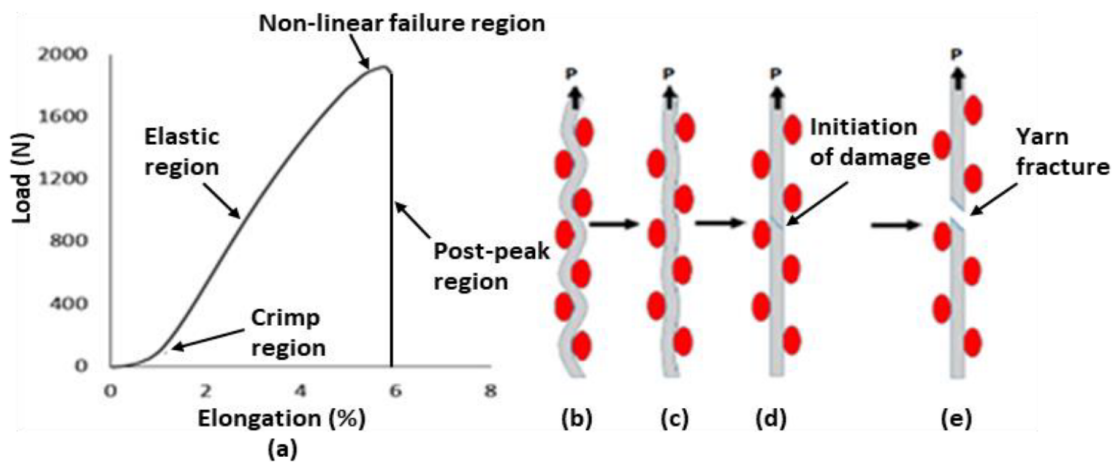
Figure 5.5: Depiction of a load-elongation curve during an uniaxial tensile loading with (b) is the crimp region, (c) the elastic region, (d) the non-linear failure region and (e) the post-peak region [106]. Note that this the force-elongation curve is for a double layer woven fabric made of basalt and glass yarns and is only shown in this report to show the effect of crimp. The load-elongation behaviour for the elastic, non-linear failure and post-peak region is not representative for polyester fabric coated with PVC.

Figure 5.6: An example of a specimen broken near the grips
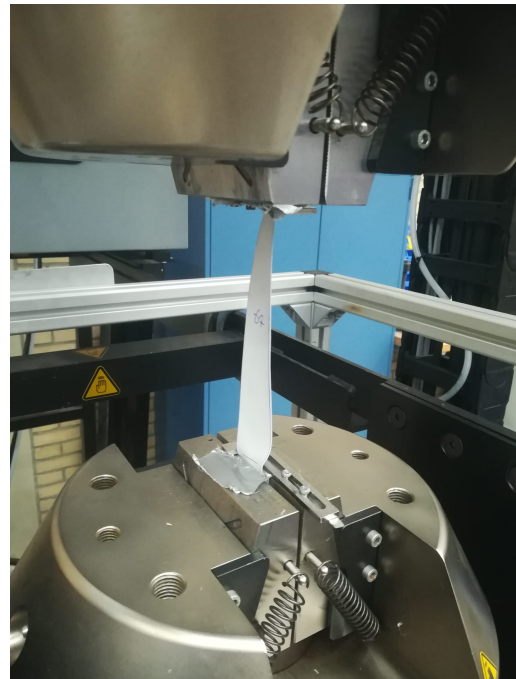
Figure 5.7: A severe case of misalignment issues during the experiments. Note that this an extreme case and that it was adjusted before performing the tensile test of this specific specimen.

5.2   Material models

Depending on the material type and strain range of the structure, different material models could be used. In this research, orthotropic linear elastic and hyperelastic material models are evaluated. A least square fitting procedure on the average measurement data of section 5.1 is performed to fit the material model variables. The result of the different material models is compared to analyse the difference between the models. In chapter 6, the material models are implemented in the FE model of the drop-stitch panel.

First, the considered material models and their assumptions are evaluated in section 5.2.1. Afterwards, the fitting procedure is shown in section 5.2.2 and the results in section 5.2.3. Section 5.2.4 concludes obtained results.

5.2.1   Evaluation of material models

This section gives a brief description of the governing equations of the material models and their assumptions. It will set a basis for the limitations of the material models, which should be taken into account. In this research, only material models implemented in `ABAQUS` 2022 are considered. A lot of hyperelastic material models originates from research into the stress-strain behaviour of biological tissues. Biological tissues are complex heterogeneous composite materials made of different media such as epithelial, connective, muscular, neuronal etcetera. This results in a non-linear and anisotropic material behaviour. Chagnon et al. [107] gave an excessive review of different hyperelastic material models used for biological tissue. For isotropic hyperelastic material, the following models could be used among others ranging from low strain and low complexity to high strain high complexity [108]:

- Saint-Venant Kirchoff
- Neo-Hookean
- Mooney-Rivlin
- Ogden

Reference works for these models include [109–112]. Peele [113] reviewed the Mooney-Rivlin model, Ogden and a bi-linear model for fiber reinforced elastomers. The six-coefficient Ogden model was chosen to represent the non-linear stiffening and softening stiffnesses. Note that Peele did not include anisotropic material models, which should be taken into account as discussed in section 5.1.3. Two types anisotropic hyperelastic material models are implemented in `ABAQUS`: the Holzapfel-Gasser-Ogden (HGO) and the Fung orthotropic (FO) model. Following, the governing equations and assumptions of the linear elastic orthotropic, Linear elastic orthotropic, FO and HGO models are evaluated.

Linear Elastic Orthotropic Model

The linear elastic orthotropic material model assumes a linear stress-strain relation, which might be acceptable within a certain strain range. At larger strains, the stress-strain behaviour becomes non-linear as shown in section 5.1.2. The linear elastic orthotropic material model also assumes that the tensile stiffness is equal to the compressive stiffness. For plane stress elements such as the shell elements, it is assumed that $\sigma_{33} = 0$ and ε_{33} is a function of the Poisson's ratio ν_{12} and in-plane Young's moduli E_1 and E_2, equation 3.1. The constitutive equation is stated as:

$$
\begin{Bmatrix} \varepsilon_{11} \\ \varepsilon_{22} \\ \gamma_{12} \\ \gamma_{13} \\ \gamma_{23} \end{Bmatrix} = \begin{bmatrix} 1/E_1 & -\nu_{21}/E_2 & 0 & 0 & 0 \\ -\nu_{12}/E_1 & 1/E_2 & 0 & 0 & 0 \\ 0 & 0 & 1/G_{12} & 0 & 0 \\ 0 & 0 & 0 & 1/G_{13} & 0 \\ 0 & 0 & 0 & 0 & 1/G_{23} \end{bmatrix} \begin{Bmatrix} \sigma_{11} \\ \sigma_{22} \\ \sigma_{12} \\ \sigma_{13} \\ \sigma_{23} \end{Bmatrix}.
$$

For material stability, the stiffness matrix needs to be positive definite, so it needs to be symmetric and have positive eigenvalues. This results in the following constraints for the variables:

$$E_1, E_2, G_{12}, G_{13}, G_{23} > 0$$

$$|\nu_{12}| < (E_1/E_2)^{1/2}$$

Fung Orthotropic Model

The FO model is purely phenomenological and strain based [76, 114]. The generalised Fung form has the form of equation 5.1 with U is the strain energy, c and D are temperature dependent material parameters and $J^{e\ell}$ is the elastic volume ratio. The red boxed part of equation 5.1 is the compressibility term, which is neglected for incompressible materials. $J^{e\ell}$ becomes 1 according to equation 5.2 for incompressible materials assuming the thermal volume ratio, J_{th}, is 1 for an isothermal load cases. For shell elements, the compressibility term is neglected. $\mathbf{Q}$ is defined as equation 5.3, where $\mathbf{b}$ is a dimensionless symmetric stiffness tensor of the anisotropic material and $\bar{\varepsilon}^{\mathbf{G}}$ is the modified Green strain tensor.

$$U = \frac{c}{2}(\exp(\mathbf{Q}) - 1) + \boxed{\frac{1}{D}\left(\frac{\left(J^{e\ell}\right)^2 - 1}{2} - \ln J^{e\ell}\right)} \tag{5.1}$$

$$J^{e\ell} = \frac{J}{J^{th}} = \lambda_1 \lambda_2 \lambda_3 = 1 \tag{5.2}$$

$$\mathbf{Q} = \bar{\varepsilon}^{\mathbf{G}} : \mathbf{b} : \bar{\varepsilon}^{\mathbf{G}} = \bar{\varepsilon}_{ij}^G b_{ijkl} \bar{\varepsilon}_{kl}^G \tag{5.3}$$

To obtain numerical stability, the initial deviatoric elasticity tensor $\overline{\mathbf{D}}_0$ in equation 5.4 should be positive definite in unloaded configuration [76, 115]. This implies that constraints 5.5-5.7 should be satisfied. Since plane stress elements are used in the FEM model, the influence of the b_{ijkl} terms in the thickness direction are neglected (encircled with red in equation 5.4).

$$\overline{\mathbf{D}}_0 = \frac{c}{2}\begin{bmatrix} b_{1111} & b_{1122} & \boxed{b_{1133}} & 0 & 0 & 0 \\ b_{1122} & b_{2222} & \boxed{b_{2233}} & 0 & 0 & 0 \\ \boxed{b_{1133}} & \boxed{b_{2233}} & \boxed{b_{3333}} & 0 & 0 & 0 \\ 0 & 0 & 0 & b_{1212} & 0 & 0 \\ 0 & 0 & 0 & 0 & b_{1313} & 0 \\ 0 & 0 & 0 & 0 & 0 & b_{2323} \end{bmatrix} \tag{5.4}$$

$$b_{1111}b_{2222} - b_{1122}^2 > 0 \tag{5.5}$$

$$\left(b_{1111}b_{2222} - b_{1122}^2\right)b_{3333} - b_{1111}b_{2233}^2 + 2b_{1122}b_{2233}b_{1133} - b_{2222}b_{1133}^2 > 0 \tag{5.6}$$

$$c > 0, b_{1111} > 0, b_{2222} > 0, b_{3333} > 0, b_{1212} > 0, b_{1313} > 0, b_{2323} > 0 \tag{5.7}$$

Holzapfel-Gasser-Ogden Model

The HGO model is meant for transverse isotropic material [116–118]. A laminate with plies consisting of transverse isotropic material stacked with a $[0, 90]_S$ stacking sequence, could model the stress strain behaviour of an orthotropic material. The strain energy formulation is invariant based instead of strain based, equation 5.8. It consists of three terms. The blue boxed term is the isotropic matrix term, which is based on the Neo-hookean strain energy formulation. For shell elements, the compressibility term boxed with red in equation 5.8 is neglected in ABAQUS. The contribution by the fiber reinforcement is captured inside the black box. Since the strain energy component $\bar{E}_\alpha$ is surrounded by Macauley brackets, the fibers do not have any contribution to the strain energy function if the strain is zero or negative. The Macaulay brackets are implemented as $\langle x \rangle = \frac{1}{2}(|x| + x)$. Note that the Macauley brackets are not implemented originally in HGO model as described by Holzapfel et al. [116]. C_{10}, D, k_1, k_2 and κ are temperature-dependent

material variables, which need to be fit for each ply. N is the amount of fiber families and C_{10} can be used to tune the matrix stiffness and compressive stiffness of the material. If one would model a tension only material, C_{10} should be close to zero. The Fung orthotropic/anisotropic material model can not model tension only materials. k_1 and k_2 are the stiffness components of the fibers. κ $(0 \leq \kappa \leq \frac{1}{3})$ describes the dispersion of the fibers as shown in figure 5.8. For $\kappa = 0$, the fibers are unidirectional, so there is no dispersion. For $\kappa = 1/3$, the fibers are randomly distributed, so the material becomes isotropic.

$$U = \boxed{C_{10}\left(\bar{I}_1 - 3\right)} + \boxed{\frac{1}{D}\left(\frac{\left(J^{e\ell}\right)^2 - 1}{2} - \ln J^{e\ell}\right)} + \boxed{\frac{k_1}{2k_2}\sum_{\alpha=1}^{N}\left\{\exp\left[k_2\left\langle\bar{E}_\alpha\right\rangle^2\right] - 1\right\}} \tag{5.8}$$

with

$$\bar{E}_\alpha = \kappa\left(\bar{I}_1 - 3\right) + (1 - 3\kappa)\left(\bar{I}_{4(\alpha\alpha)} - 1\right)$$

$\bar{I}_1$ and $\bar{I}_{4(\alpha\alpha)}$ are the first strain invariant and the fourth strain pseudo-invariant respectively. Strain invariants are used to describe inhomogeneous deformation without consideration of the principal directions of the geometry [119]. $\bar{I}_1$ is a function of all principal stretches and $\bar{I}_{4(\alpha\alpha)}$ is dependent on the principal stretches in the fiber direction.
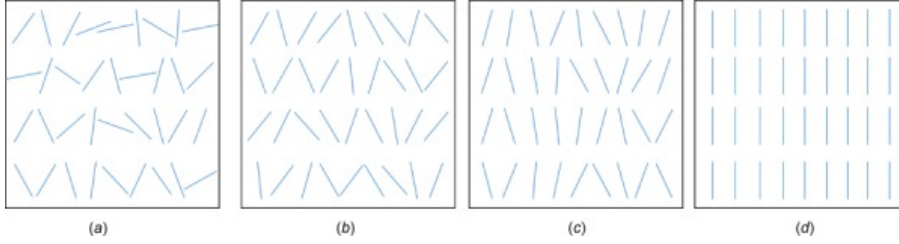
Figure 5.8: A sketch of the dispersion parameter κ in a 2D domain ranging from no preferred fiber direction to a single fiber direction ($\kappa = 1/3$)(a), ($\kappa = 1/6$)(b), ($\kappa = 1/12$)(c), ($\kappa = 0$)(d) [120]

5.2.2 Fitting procedure

To fit material models, a least squares fitting approach has been used. The governing minimisation equation is shown in equation 5.9 with $J(\theta)$ is the cost function (the function that will be minimised), $r_n\left(y_n, f\left(x_n, \theta\right)\right)$ is the residuals function. The residuals function is as described in equation 5.10 with θ is an array containing the unknown variables of a material model and y_n and x_n are the force and displacement measurement data points respectively. The function $f\left(x_n, \theta\right)$ is the resulting force function of an `ABAQUS` FE model.

$$J(\theta) = \frac{1}{2}\sum_{n=1}^{N} r_n\left(y_n, f\left(x_n, \theta\right)\right)^2 \tag{5.9}$$

$$r_n\left(y_n, f\left(x_n, \theta\right)\right) = f\left(x_n, \theta\right) - y_n \tag{5.10}$$

An FE model in `ABAQUS` of the strip specimens as described in section 5.1 is built. A rectangular strip has been modelled of 155x25 mm consisting of shell elements, S4R, with a global element size of 2.5 mm, figure 5.9. A displacement control has been used to increase the load exerted on the strip with a static solver.

Figure 5.10 shows a flowchart of the fitting procedure. The material models parameters has been adjusted in an `ABAQUS` input file by the `least_squares` function of the Python package Scipy [121]. The default tolerances of this `least_squares` function has been used.
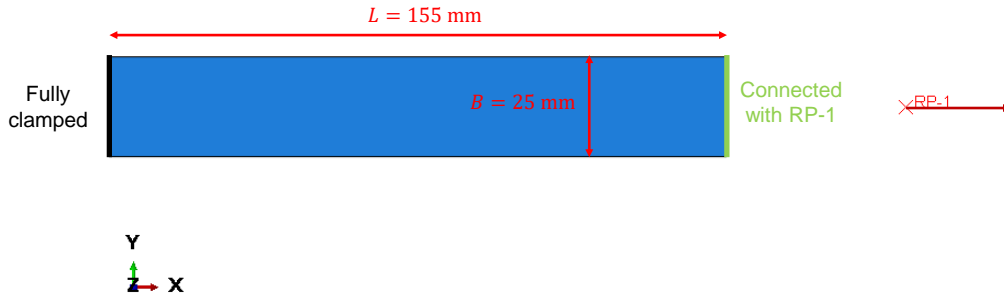
Figure 5.9: A visualisation of the FE model used to fit the material models. A strip is modelled with a length of 155 mm and width of 25 mm. The left edge of the strip is fully clamped and the right edge is connected to a reference point (RP-1) with rigid beam connectors. RP-1 is translated to tension the strip.
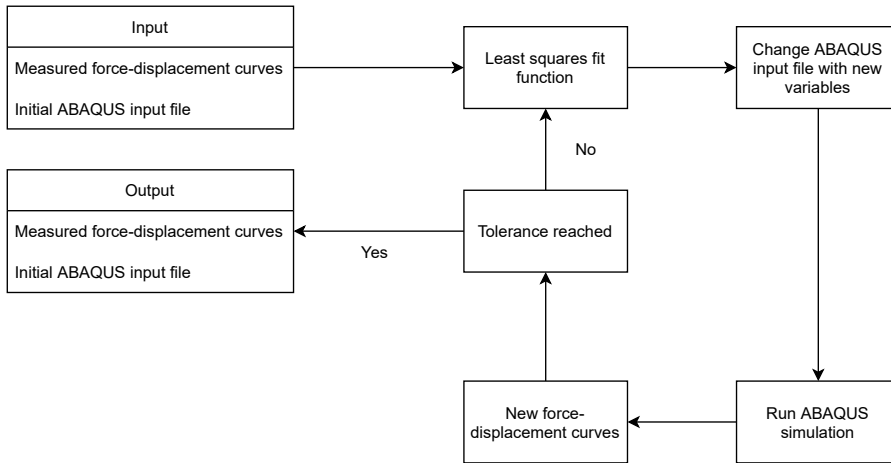
Figure 5.10: Flowchart of the least squares fitting procedure

5.2.3 Results

The fitted material models are shown in figure 5.11. Figures 5.11 only depicts 5 mm displacement, which corresponds to 3.2% strain assuming $\varepsilon = u/L_0$ with u is the displacement and L_0 the gauge length. The variables resulted from the fitting procedure are shown in appendix B.2.

Two linear elastic orthotropic material models are fitted. The linear elastic orthotropic 1 (LEO 1) material model is fitted in the toe region (until 1.3% strain) and linear elastic orthotropic 2 (LEO 2) material model is fitted for larger strains (until 3.2% strain). It can be noticed that the LEO 1 material model underestimates the material stiffness in the 0° and 90° at strains larger than approximately 1%, but provide an accurate estimate at strains smaller than 1%. LEO 2 provides a more averaged stiffness representation until 3.2% strain. The stiffness of the FO material model is lower than the measurements in the 90° direction. Furthermore, the FO model simulates the material stiffness in the 0° lower until around 2.7% strain and higher at strains above 2.7% strain. The HGO model has a better fit in the 90° specimen direction than the FO model. It has a slightly higher stiffness than the FO model in the 0° specimen direction. A significant difference can be observed in the force displacement behaviour in the 45° direction. The HGO model does not model the material stiffness in the 45° direction correctly, since it has no stiffness in that

44

direction. All the anisotropic hyperelastic material models, which are implemented in ABAQUS, are not able to model the S-shape in the 0° specimen direction. Due to the fact the strain energy formulations are exponential functions as shown in equation 5.1 for the FO model and 5.8 for the HGO model, it will not be possible to model the S-shape.
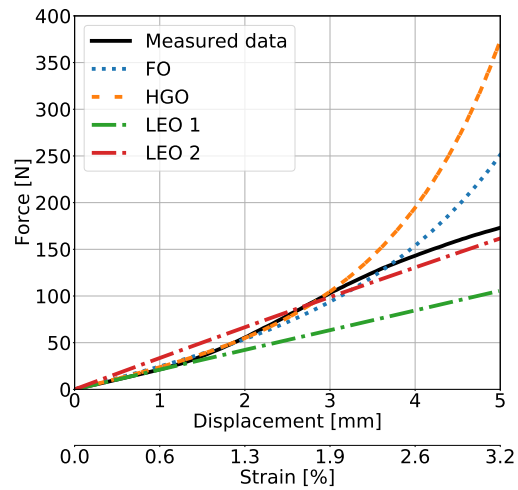
(a) The force-displacement curves of the face sheets in the 0° specimen direction for the material models and measurements.
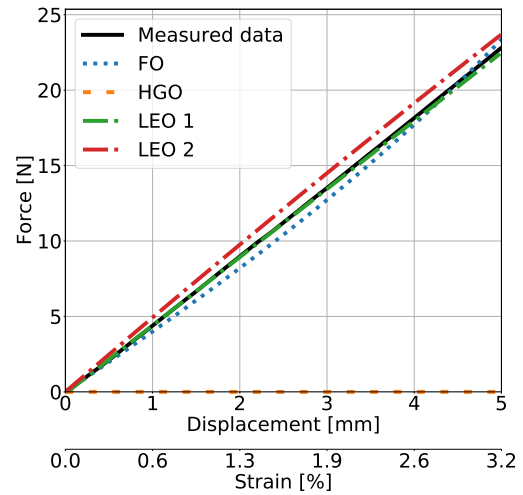
(b) The force-displacement curves of the face sheets in the 45° specimen direction for the material models and measurements.
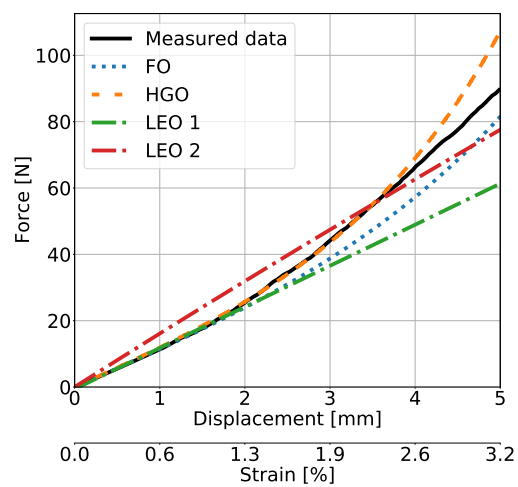
(c) The force-displacement curves of the face sheets in the 90° specimen direction for the material models and measurements.
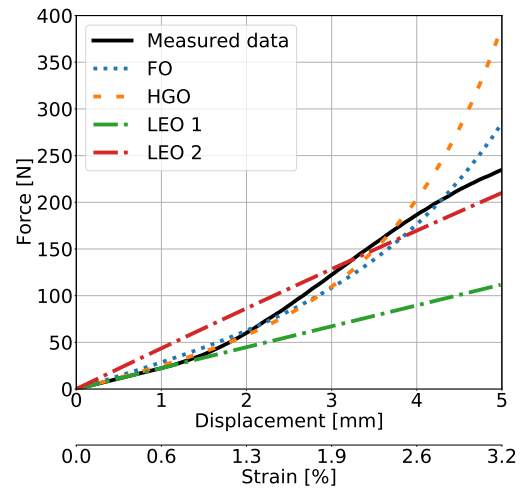
(d) The force-displacement curves of the edges in the 0° specimen direction for the material models and measurements.
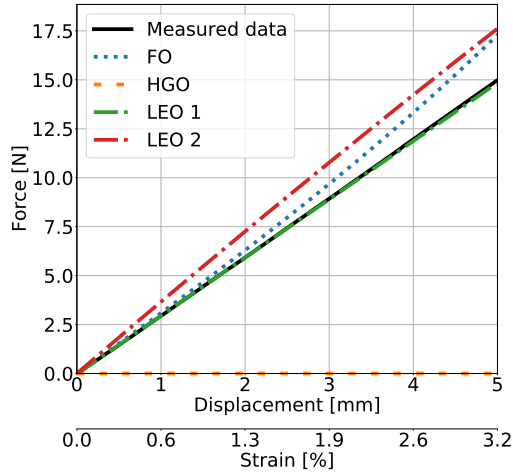
(e) The force-displacement curves of the edges in the 45° specimen direction for the material models and measurements.
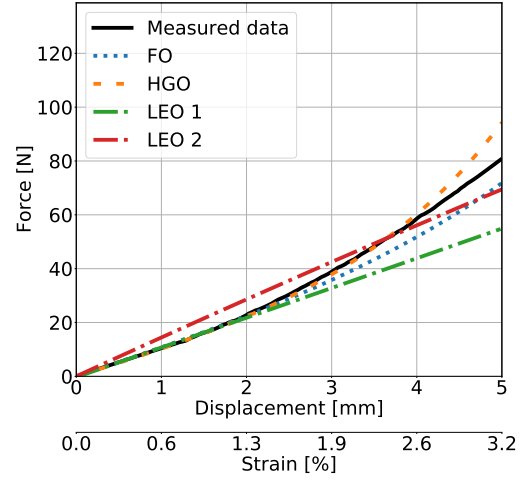
(f) The force-displacement curves of the edges in the 90° specimen direction for the material models and measurements.

Figure 5.11: The force-displacement curves of the fitted material models compared with the measurements.

5.2.4 Conclusions

The FO, HGO and linear elastic orthotropic material models are fitted using the `SciPy least_squares` function. The uniaxial tensile test of section 5.1 is modelled in a `ABAQUS` FE model to fit the variables of the material models. The force-displacement behaviour of the different models is compared with the measurement data.

All the material models are not able to exactly model the material stiffness. LEO 1 and LEO 2 provides a linear estimate of the material stiffness, which might suffice within a certain strain range. LEO 1 provides an accurate estimate of the material stiffness for strains lower than 1% and LEO 2 a more averaged estimate of the strains lower than 3.2%.

The stiffness in the 45° of the HGO model is negligible small. Due to the assumption that the material stiffness is solely provided by the fibers within the polyester fibers coated with PVC, the in-plane shear stiffness is too small. Relaxing this assumption by increasing the values of C_{10} and/or κ, would increase the matrix stiffness and result in more realistic results. The HGO model is not further used in this research, since it is expected to result in low convergence rates due to the small matrix stiffness.

The FO uses an exponential function to model the material stiffness. In most specimen directions it provides a more accurate estimate representation than the LEO 1 and 2 model for a 3.2%. However at the face sheet in the 0° it overestimates the stiffness. The FO model's variables are dependent. This implies that changing a parameter might result in a better fit in one direction, but worsens the fit in other directions. The fits may be further optimised. The influence of the different material models on the structural response is further evaluated in chapter 6.

Depending on the strain range found in chapter 6, a material model is adopted for the validation of the FE model of the drop-stitch panel. The strain range and influence of the material models on the global structural response of the drop-stitch panel is further discussed in section 5.2.1.

There are some remarks on the results of:

- Getting an exact fit using the considered material models is difficult, since the S-shape in 0° specimen direction can not be described with an exponential strain energy function or a linear stress-strain relation. Moreover, due to the exponential function, the stiffness goes to infinity, which creates an unrealistic high stiffness and convergence issues for high strains. A different kind of function to describe the non-linear stress-strain behaviour of the anisotropic hyperelastic material model should be established. Implementing discontinuous stress-strain functions as Chen et al. [122] proposed for Uretek3216A fabric, a polyester fiber coated with polyvinyl fluoride (PVF), might be used. It divides the stress-strain curve in five distinct regions as shown in 5.12. In regions OA, BC and DE a linear function is adopted, AB a logarithmic and CD an exponential function. By subdividing the stress-strain curve into regions, a discontinuous stress-strain function is formulated, which could cause issues with convergence.

- The HGO model does not model the material stiffness in the 45° direction correctly. This is due to the fact that it is assumed that only unidirectional fibers contribute to the stiffness and the isotropic matrix does not. This assumption is too strict. If one would use this model, the isotropic matrix stiffness should be taken into account to provide shear stiffness. The HGO model is not further considered in this research.

- The `SciPy` least square function is meant for independent variables. As mentioned, the variables are dependent of the FO and HGO models. This implies that there are multiple local minima for the cost function 5.9 and that finding the global minimum is difficult using the `SciPy` least squares function. The local minimum found by the least squares function is affected by the initial guess and the boundaries of the variables. A different solver is advised to investigate, whether the resulting minimum is the global minimum.
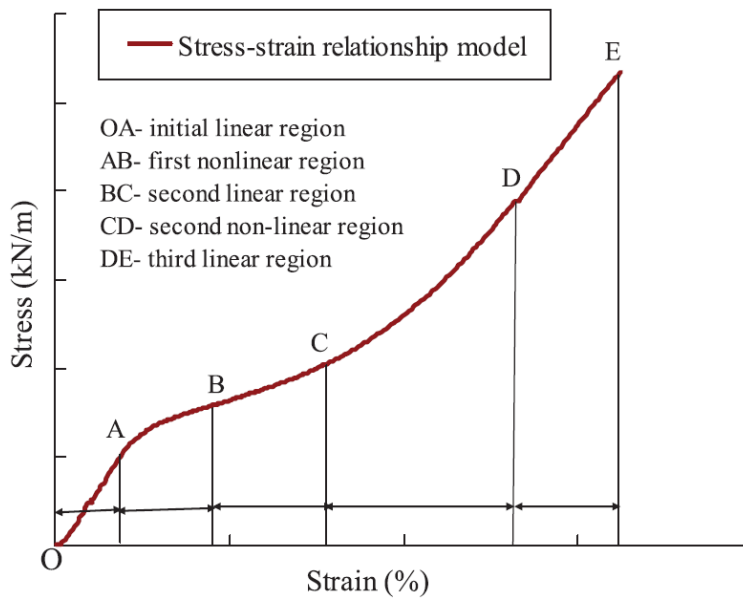
Figure 5.12: The five distinct regions Chen et al. used to describe the stress-strain behaviour of Uretek3216A fabric [122].

<div align="right">

Chapter **6**

</div>

Drop-stitch Panel Model

To get more insight in the bending characteristics of a drop-stitch panel, a three point bending load case is modelled using a three-dimensional finite element model. The FEM model is build in `ABAQUS` 2022. It will give a better understanding in the failure mechanism of a drop-stitch panel and wrinkling initiation and propagation. Note that if the drop-stitch has negligible bending stiffness, the drop-stitch panel is considered to be failed.

The wrinkling onset load is the load from which wrinkling occurs and the force-displacement curve of the load beam becomes non-linear. This gives some insight in the wrinkling onset load, which is the minimum load from which wrinkling occurs and the bending stiffness becomes non-linear. Section 6.1 gives a description of the geometry and parameters used to model drop-stitch panel. Note that the assumptions and background theory of the procedures in `ABAQUS` are discussed in chapter 3. The results of the FEM model are assessed in section 6.2. Section 6.3 concludes and discusses the results of the FEM model. Note that the appendices contains the following supplementary material: In appendix C an analytical model based on the method of Cavallaro et al. [43] is derived, which is used to estimate the wrinkling onset load; In appendix D the stress in xx-direction for 20 and 30 mm yarn distance is shown using the quarter model; and in appendix E the analytical perturbation model is derived.

6.1   FE Model

The FEM model should give insight in the bending characteristics and failure mechanism of a drop-stitch panel subjected by a three point bending load case. Two drop-stitch models are generated and compared with each other as shown in figure 6.1: a quarter model and strip model. Since the drop-stitch panel is subjected by a three point bending load case, two symmetry planes can be used, so only modelling a quarter of the drop-stitch panel should suffice. The response the drop-stitch panel seemed uniform over the width for the three point bending test, so it is expected that a strip model should suffice as further discussed in section 6.2.2. The drop-stitch panel is also modelled as a strip, which assumes the structural characteristics are solely influenced by the face sheets and are uniform over the width.

The geometry of the quarter and strip model are discussed in section 6.1.1. The material, fluid cavity and other properties of the FEM model are discussed in section 6.1.2. The loads and boundary conditions used in the FEM model are discussed in 6.1.3. Finally the mesh and the mesh convergence analysis is evaluated in section 6.1.4.

6.1.1   Geometry

A smaller panel than the experiments performed in chapter 4 has been modelled comparable to the dimensions used by Davids et al. [32]. As shown in figure 6.1, the quarter and strip models are simplifications of the full drops-stitch panel to reduce computational time.
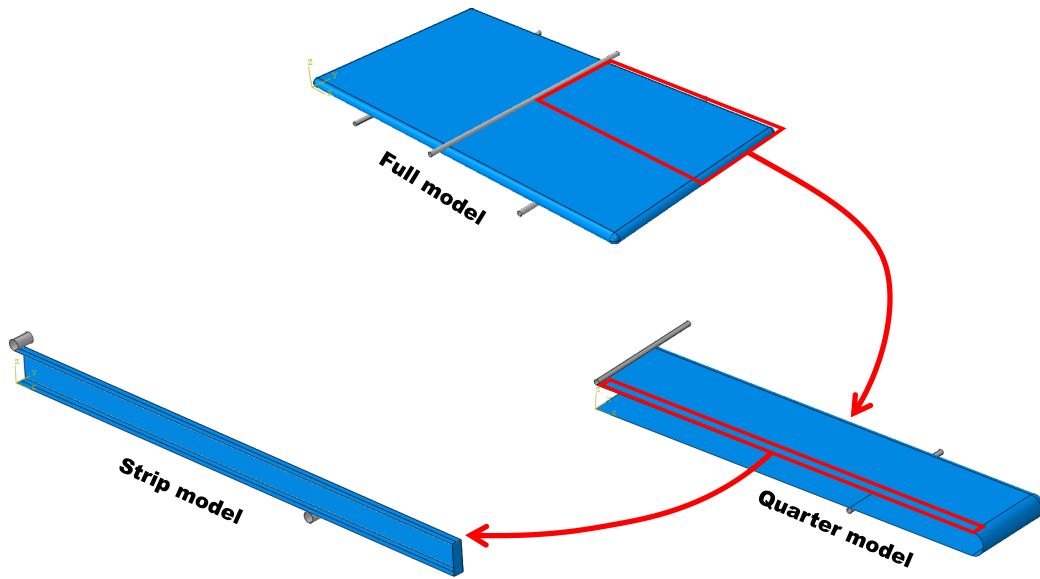
Figure 6.1: A depiction of the full quarter and strip models of the drop-stitch panel.

Quarter model

In figure 6.2, the geometry, origin and symmetry planes are depicted. The quarter model has a length of 3.05 m, width of 0.72 m and height of 0.174 m. Note that these are dimensions of the quarter panel including the closing edges. The cross sectional area has a half obround shape. The support beam is placed at 1.1 m offset of the edge and load beam at $x = 0$. The support and load have a cylindrical shape with a radius of 2 cm and is assumed to be rigid. The face sheets are 0.7 mm thick and the closing edges 0.6 mm based on information provided by the manufacturer of the drop-stitch panels of chapter 4. Two symmetry planes are are defined as shown in figure 6.2 to impose boundary conditions, which will be further discussed in section 6.1.3.
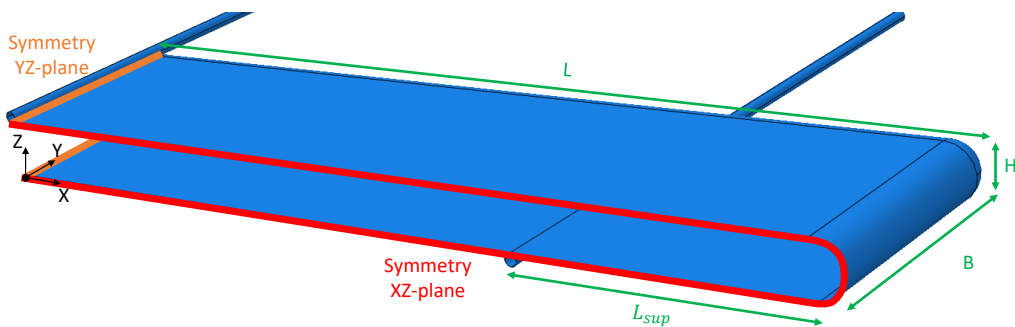
Figure 6.2: A depiction of the geometry of the quarter model. The length, L, and width, B, include the closing edges. The radius of the edges is equal to halve of height of the panel, H. On the lower face sheet at the intersection of the XZ- and YZ-symmetry planes, the origin of the model is located. Coloured with red and orange, the XZ- and YZ-symmetry planes are marked respectively. Note that the symmetry YZ-plane is over the full with, so it also includes the circular closing edge. L_{sup} is the support offset, which is defined from the end of the panel including the closing edge to the middle of the support beam.

Strip model

The strip model is a simplification of the quarter model, which does not include the full width and the edges of the panel. Depending on the yarn distance, the width of the strip model is changed as shown in figure 6.3. The length of the model is 3.05, which is equal to the full length of the quarter model including the closing edges. The length of the closing edges is not excluded to ensure the mass of the strip model does not deviate too much from the quarter model, which would cause differences in the initial deflection due to the gravity. To enclose the fluid cavity, shell elements with a low Young's modulus and thickness are used. For the enclosing edges, an isotropic material is assumed with a Young's modulus of 100 Pa, Poisson's ratio of 0 and thickness of 0.6 mm. Their contribution to the global bending stiffness is insignificant compared to the face sheets, since the Young's modulus of the edges is much smaller than Young's modulus of the face sheets. It is ensured that the edges stay flattened by using a coarse mesh with a length equal to the height of the panel and width equal to the mesh size of the face sheets. The displacements of the face sheets' nodes are coupled with the edges' nodes. So, the displacements of the edges are mostly affected by the displacements of the nodes of the face sheets. The face sheets' thickness is 0.7 mm and L_{sup} is 1.1 m.
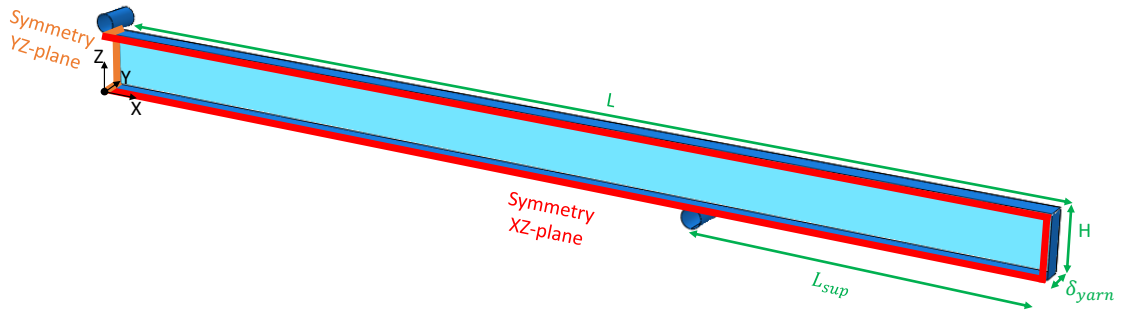
Figure 6.3: A depiction of the strip model with L is the length, δ_{yarn} the yarn distance, which is equal to the width of the model and H the height. The origin of the model is located on the lower face sheet at the intersection of the XZ- and YZ-symmetry planes. The XZ- and YZ-symmetry planes are coloured with red and orange respectively. Note that length L does not include the closing edge.

6.1.2   Material, yarn and fluid cavity properties

Three types of properties are defined: the material, yarn and fluid cavity properties. The material properties are discussed in chapter 5. The fluid cavity is assumed to be an ideal gas. Its properties are based on the properties of air as shown in table 6.1 [77].

Table 6.1: Properties of fluid cavity [77].

Variable	Definition	Value
p_A	Ambient pressure	101325 Pa
θ	Temperature	$20°$
θ^Z	Absolute zero temperature	$-273.15°$
MW	Ideal gas molecular weight	$0.02896 \frac{kg}{mol}$
$\widetilde{R}$	Universal gas constant	$8.314 \frac{J}{K \cdot mol}$

The yarn properties are based on the yarn properties used by Hulton et al. [31]. An evaluation of the yarn properties has not been performed in this research. It is assumed that the yarns

have a negligible small buckling load, so the compressive stiffness is neglected. Two axial force-displacement data points are used as input in `ABAQUS` with constant extrapolation and linear interpolation to model the linear elastic stiffness and tension only material properties. Figure 6.4 shows a sketch of the force displacement behaviour with the two data axial force-displacement data points. It is ensured that the strain of the yarns is equal for different yarn distances.
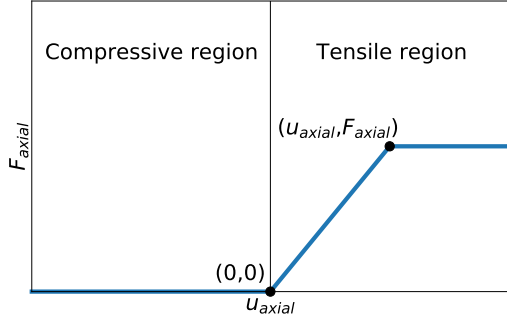
Figure 6.4: A sketch of the axial force deformation curve for the yarns. In the left region, the yarn is under compression and in the right under tensile. Two data points at $(0,0)$ and (u_{axial}, F_{axial}) with linear interpolation and constant extrapolation are used.
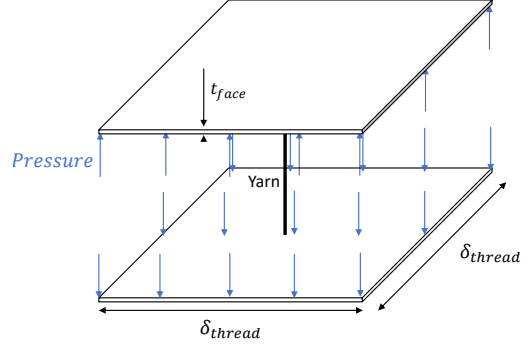
Figure 6.5: A section of the face sheet with the size of one yarn spacing. The internal air pressure is depicted with blue arrows. A yarn is depicted vertically in the middle of the segment with a black line between the upper and lower face sheet.

The cross sectional area of the yarns has been scaled for different yarn distances assuming the section depicted in figure 6.5. This result in the following equation:

$$F_{axial} = \frac{EA}{L_0} U_{axial} \text{ with } F_{axial} = P\delta_{yarn}^2$$

The axial strain of the yarn is set equal for all yarn distances:

$$\frac{U_{axial}}{L_0} = \frac{U_{axial,ref}}{L_{0,ref}} \tag{6.1}$$

$U_{axial,ref}$ and $L_{0,ref}$ are the reference axial deformation and initial length of the yarn respectively, which are the values of Hulton et al. [31]. This results in the scaling law for the cross sectional area of the yarns

$$A = \frac{\delta_{yarn}^2}{\delta_{yarn,ref}^2} A_{ref}$$

with $\delta_{yarn,ref} = 6.35$ mm, $A_{ref} = 0.00167$ mm^2 and $E = 7.24$ GPa based on the values of Hulton et al. [31]. For different yarn spacings, the force at a certain displacement can now be determined. For $U_{axial} = 0.02$ m and $L_0 = 0.174$ m, results in the F_{axial} values of figure 6.6 for different yarn spacings, which is used as input data in `ABAQUS`.
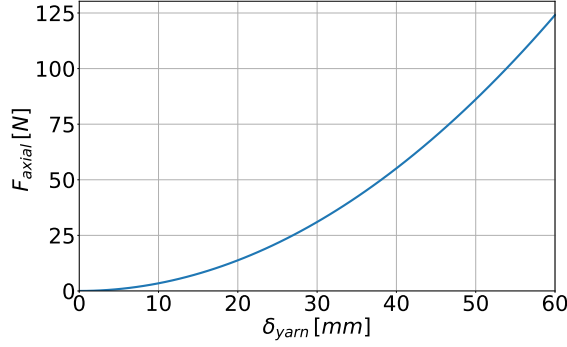
Figure 6.6: Axial force exerted by the yarns for different yarn distances with $E = 7.24$ GPa, $L_0 = 0.174$ m, $\delta_{yarn,ref} = 6.35$ mm, $A_{ref} = 0.00167$ mm^2 for an axial displacement of 2 cm.

6.1.3 Loads and boundary conditions

The FEM simulation is divided into four load steps as shown in figure 6.7: the initial, inflation, gravity and three point bending load step. During each of these loads steps loads, contact interactions and boundary conditions are changed.
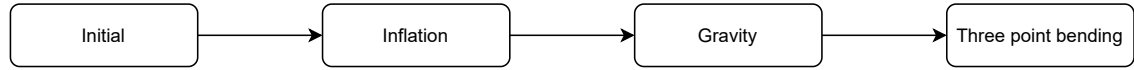
Figure 6.7: A flowchart of the load steps of the FE model.

In the initial step, the initial conditions of the drop-stitch panel are defined. Two symmetry boundary conditions in the XY- and YZ-plane are applied at x=0 and y=0 as shown in figures 6.2 and 6.3. The translations in the z-direction are constrained at the origin (x,y,z)=(0,0,0). The load and support beams are fully clamped. The contact interactions between the load and support beams and the drop-stitch panel are not activated yet during the initial step.

During the inflation step, the fluid cavity is inflated to a desired initial air pressure. All the boundary conditions set in the initial step are propagated during this step.

Afterwards, the weight is added during the gravity step. A gravity load is added to the face sheets and closing edges. Note that it is assumed that the yarns do not have any mass. The contact interactions for the support on the drop-stitch panel is added during this step. The z-constraint and fluid cavity boundary conditions are inactivated. The z-constraint is not needed anymore during this step, since the drop-stitch panel is constrained in the Z-direction by the support beam. The fluid cavity boundary condition is inactivated to initiate pressure-volume work.

Finally, the three point bending test is performed. The contact interaction between the load beam and the drop-stitch panel is activated and the load beam is translated in the z-direction downwards to a desired translation. Table 6.2 gives a visualisation of the boundary conditions per load step.

6.1.4 Mesh

As discussed in 3.1, S4R/S3R elements are used. Figure 4.4 shows that the bending stiffness might be significant for the wrinkling response of the face sheets, so membrane elements are not considered further in this research. It is expected that the element length is dependent on the wrinkles and bumps due to the internal air pressure that arise, as sketched in figure 2.14. The face sheets edges need to be able to develop wrinkles. A coarse mesh could lead to an inaccurate prediction of local stress concentrations, which develop due to the yarns and wrinkling. It is

Table 6.2: A visualisation of the boundary conditions which are activated, inactivated or modified during each load step. The green cells means the boundary condition is activated, red cells inactivated and yellow cells modified.

Boundary condition	Step			
	Initial	Inflation	Gravity	Three point bending
Symmetry XZ-plane	green	green	green	green
Symmetry YZ-plane	green	green	green	green
z-constraint	green	green	red	red
Fluid cavity	red	green	red	red
Load beam	green	green	green	yellow
Support beam	green	green	green	green
Gravity load	red	red	green	green

expected that the length of the wrinkles/bumps is approximately equal to the yarn distance, so the mesh convergence study is performed by dividing the yarn distance with the global element length:

$$\tau_{global} = \frac{\delta_{yarn}}{h_{global}}$$

with τ_{global} is the non-dimensionlised element length, h_{global} the global element length and δ_{yarn} the yarn distance. τ_{global} gives an indication of the amount of elements between each yarn distance. The quarter model with a $\delta_{yarn} = 60$ mm, linear elastic orthotropic material model 1 and $P = 15$ kPa has been used for the mesh convergence. The force displacement of the load beam has been compared for different global element lengths, figure 6.8 for $\tau = [5, 10, 15]$. $\tau = 5$ is a bit stiffer than $\tau = 10$ and $\tau = 15$ at larger deflections. Also, the simulation did not converge for large deflection that might be caused by a local stress concentrations as shown in figure 6.9, which suggests that $\tau = 5$ is too coarse. $\tau = 10$ and $\tau = 15$ resulted in similar force displacement curves, so $\tau = 10$ is considered to be a sufficient element length and will be used in this research. Local mesh refinements at the wrinkled region(s) to reduce the amount of elements, has not been investigated thoroughly, since it is difficult to predict the region affected by wrinkles beforehand. The tension field theory might able the usage of a coarser mesh, but as mentioned in 2.3 it is not considered.
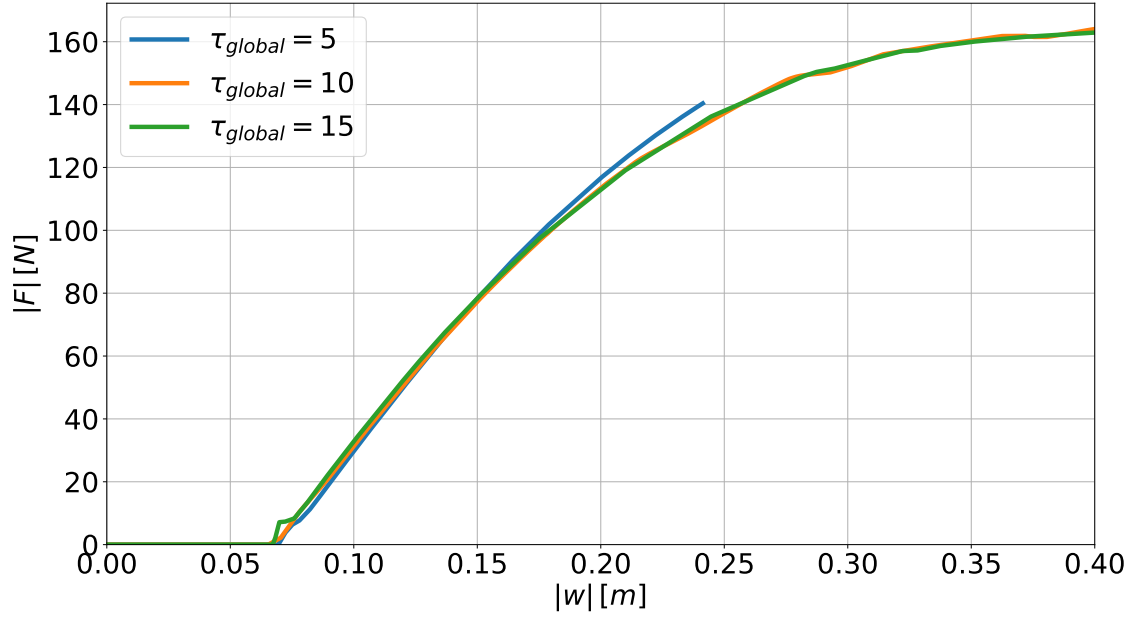
Figure 6.8: Force displacement curves for $\tau_{global} = [5, 10, 15]$ using the quarter model, $\delta_{yarn} = 60$ mm, LEO1 and $P = 15$ kPa. It shows that $\tau_{global} = 5$ did not fully converge and is slightly stiffer than $\tau_{global} = [10, 15]$. $\tau_{global} = 10$ and $\tau_{global} = 15$ seems to result in similar results. The initial deflection is due to the gravity load. Note that a small discontinuity in the force-displacement curve is observed at the initial deflection due to the impact of the load beam on the drop-stitch floater.

(a) $\tau_{global} = 5$

(b) $\tau_{global} = 10$
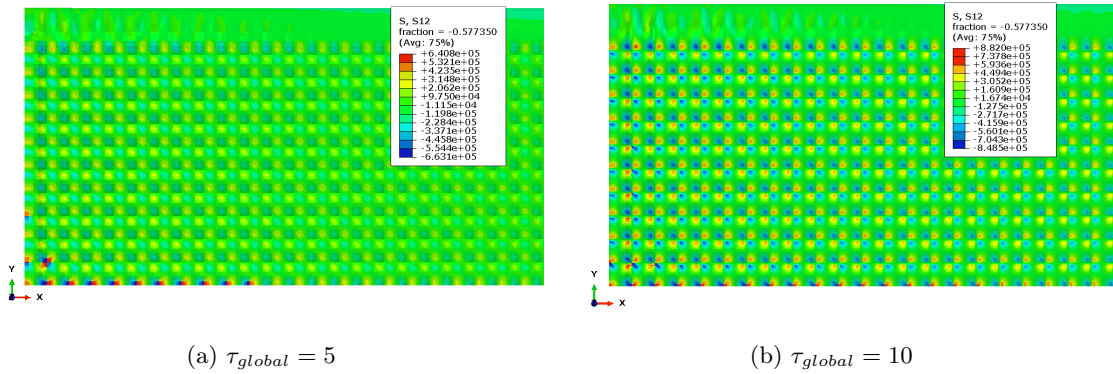
Figure 6.9: A local stress concentration in the XY-direction in the load region is observed at $\tau_{global} = 5$. A top view of the XY-plane is shown in figures (a) and (b). The left edge of the panels is the region where the load beam is located in the quarter model as depicted in figure 6.2. The figures shows the drop-stitch panel with a $\delta_{yarn} = 60$ mm, linear elastic orthotropic material model 1 and $P = 15$ kPa around a displacement of 0.23 m. At $\tau_{global} = 10$ a more uniform pattern over the load region is observed.

6.2 Results

Two different failure modes with distinct behaviour has been observed: a global wrinkling and a local folding failure mode. Both have distinct behaviour. More insight in the initiation of these failure modes and distinct characteristics is obtained by performing a parametric analysis. Three parametric analyses have been performed to get more insight in the bending characteristics and wrinkling behaviour of drop-stitch panels. For different yarn distances, face sheet thicknesses, air pressures FEA are performed, which provides a better understanding in their influences. Also, the global response of the different material models are evaluated.

First, a description of the failure modes is given in section 6.2.1. The influence of the yarn distance has been evaluated in section 6.2.2. This also provides an evaluation of the difference between the strip and quarter model. the influence of the face sheet thickness, internal air pressure and material model has been evaluated in section 6.2.3, 6.2.4 and 6.2.5 respectively. Finally, the strip model is validated using the results of the three point bending test of chapter 4.

6.2.1 Failure modes

A local folding and a global wrinkling mode are observed during the FE analysis. In the local fold failure mode, a downwards deflection is generated as shown in figure 6.10a. The initial deflection as shown in figure 2.14 generated by the air pressure has vanished locally and downwards fold is initiated. In the global wrinkling mode, an upwards deflection is generated as shown in figure 6.10b. The initial deflection generated by the internal air pressure is intensified locally. In the folding failure mode, one or multiple yarns in the region in contact with the load beam get compressed, whereas in the global wrinkling mode they stay tensioned.

(a) The local folding failure mode with a yarn spacing of 20 mm.

(b) The global wrinkling failure mode with a yarn spacing of 30 mm.
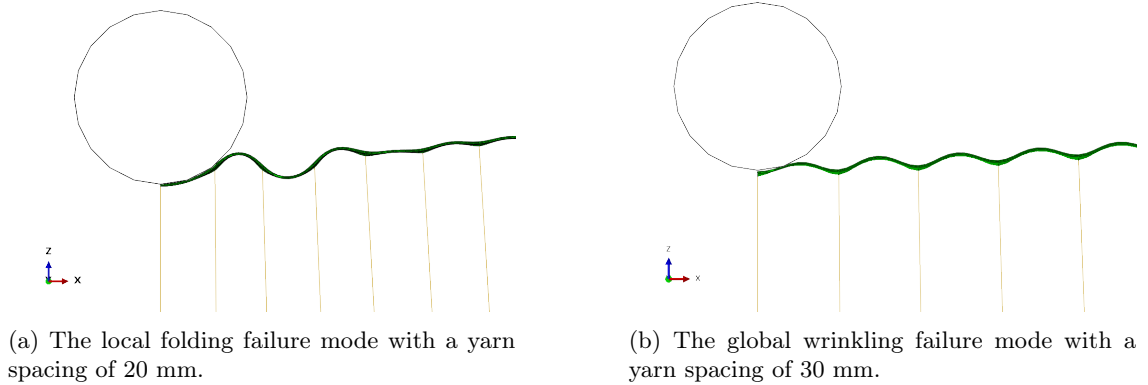
Figure 6.10: Depiction of the failure modes using the strip model with an internal air pressure of 15 kPa, LEO1 material model and face sheet thickness of 0.7 mm at an displacement of 0.4 m. The upper face sheet at the region near the load beam is shown.

6.2.2 Influence of the yarn distance

The strip and quarter model has been used with LEO 1 material model of chapter 5, an internal air pressure of 15 kPa and different yarn distances. Due to the reduction of width in the strip model, the bending stiffness is smaller compared to the quarter model, which results in a lower force output. N_{ratio} is a correction for the reduction in bending stiffness. The force output of the strip model has been corrected with a factor N_{ratio} to coincide with the quarter model:

$$F_{cor} = N_{ratio}F_{strip} \tag{6.2}$$

Figure 6.11 shows the force displacement curves of the load beam for the strip and quarter model with different yarn spacings. It clearly shows that the yarn distance affects the bending stiffness. The initial deflection due to gravity does not differ significantly for the different yarn distances. At the initial deflection, a small peak is observed due to the impact force of the drop-stitch panel on the load beam. Due to issues with computational power, the quarter model for $\delta_{yarn} < 20$ mm has not been evaluated.
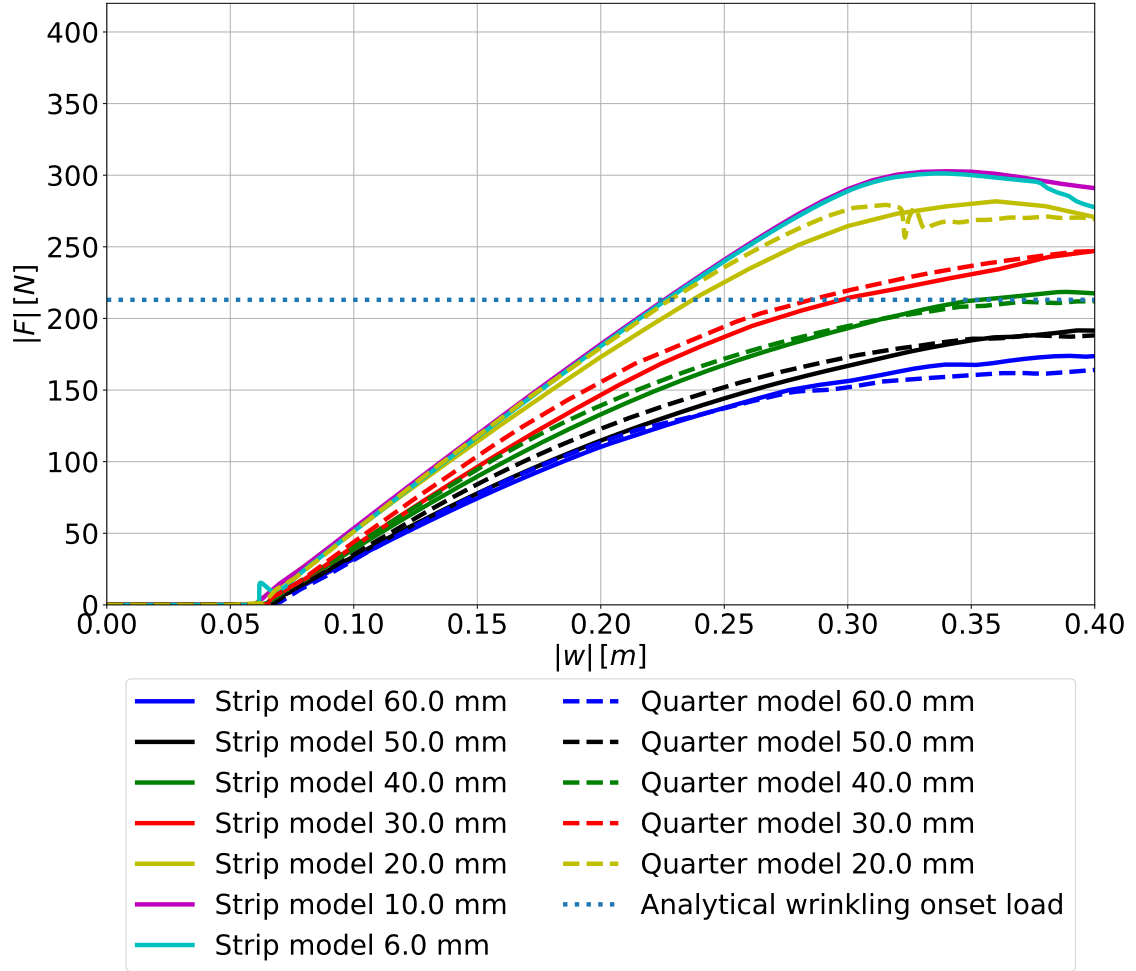
Figure 6.11: Force displacement curves of the strip and quarter model for different yarn. The x-axis shows the absolute displacement and the y-axis the absolute load of the load beam. The initial displacement is due to the gravity load. The analytical wrinkling onset load is determined as described in section C.

A transition between failure modes is observed between 20 and 30 mm yarn spacing. In figure 6.11, $\delta_{yarn} \geq 30$mm are of the global wrinkling failure mode and $\delta_{yarn} < 30$mm local folding failure mode as shown in figure 6.10. For both of these failure modes different formulations of N_{ratio} were needed to correlate the results of the strip model to the quarter model:

$$N_{ratio} = \frac{I_{\text{yy,face}}}{I_{\text{yy,strip}}} \qquad \rightarrow \text{Global wrinkling failure mode}$$

$$N_{ratio} = \frac{E_{\text{xx,face}}I_{\text{yy,face}} + E_{\text{xx,edge}}I_{\text{yy,edge}}}{E_{\text{xx,face}}I_{\text{yy,strip}}} \qquad \rightarrow \text{Local folding mode}$$

with $I_{\text{yy,face}} = 2(B - \frac{h}{2})t_{face}(\frac{h}{2})^2$, $I_{\text{yy,strip}} = 2t_{face}(\delta_{yarn} - \frac{h}{2})(\frac{h}{2})^2$ and $I_{\text{yy,edge}} = \pi t_{edge}(\frac{h}{2})^3$. As shown in figure 6.1-6.3, the strip model only models the face sheet with a width equal to the yarn spacing. This results in a lower force output compared to the quarter model, which should be corrected to be able to compare both models.

A slight difference in the force-displacement behaviour at 20 mm between the strip and quarter model is observed, which might be due to the difference in contact area. For smaller yarn spacings, the initial deflection due to the pressurisation decreases. Figure 6.13 shows the initial perturbation of the face sheets due to pressurisation for different yarn distances for the FEA and analytical perturbation model, which is derived in appendix E. The displacement of the analytical uniaxial tensile model is based on the following equation:
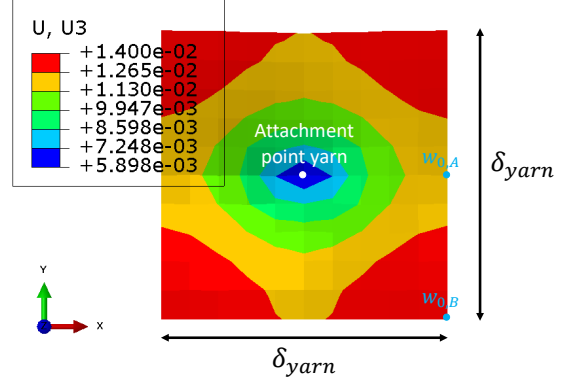
Figure 6.12: The locations at which $w_{0,A}$ and $w_{0,B}$ are evaluated in the FE model.

$$\frac{2u_x}{\delta_{yarn}} = \frac{PH}{t_{face}E_{xx}}$$

$w_{0,A}$ is determined at a distance of halve a yarn distance from the yarn attachment point as shown in figure 6.12 and $w_{0,B}$ is the maximum perturbation measured at $1/2\sqrt{2}\delta_{yarn}$ distance. The decrement of the initial perturbation results in a more flattened panel. Also, a change in longitudinal tension is observed for different yarn spacings. The analytical perturbation model shows comparable perturbation with the FE model for small yarn spacings. At large yarn spacings, the perturbation is overestimated by the analytical perturbation model, which is probably due to an underestimation of the longitudinal displacement. For large yarn spacings, the length of the panel decreases due to inflation, since the distributed pressure load on the face sheet causes a negative displacement, and for small yarn distances vice versa in the analytical perturbation model. This decrement in longitudinal displacement can also be observed in the FEA, but it is overestimated in the analytical perturbation model. This might be due to the assumption of an 1D model, which neglects the Poisson's effect and the pretension generated in the transverse direction.
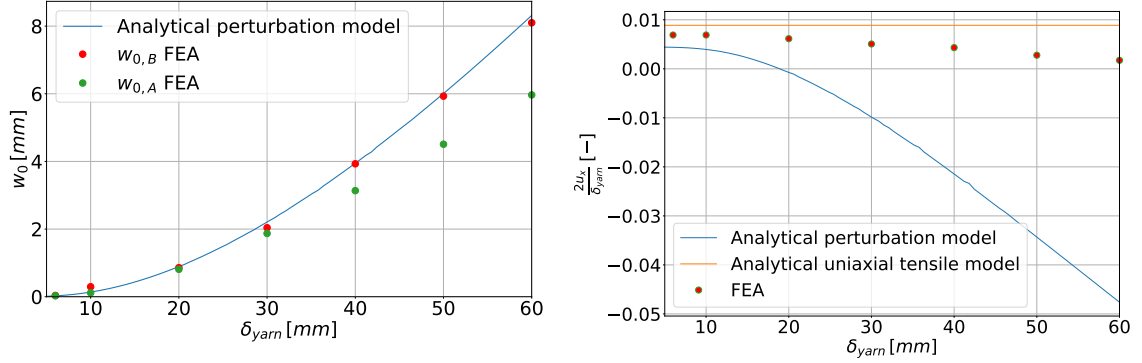
(a) The initial perturbation of the analytical and FEA model with $w_{0,A}$ is the maximum perturbation and $w_{0,B}$ the perturbation between two yarns.

(b) The longitudinal displacement over one yarn distance of the analytical perturbation model

Figure 6.13: The initial perturbation w_0 and longitudinal strain over one yarn distance $\frac{2u_x}{\delta_{yarn}}$ after inflation for different yarn spacings using the analytical perturbation model and FEA of the strip model with an internal air pressure of 15 kPa, $t_{face} = 0.7$ mm and LEO1 material model. The derivation of the analytical perturbation model can be found in appendix E.

At a yarn distance of ≤ 20 mm, the edges have a higher initial deflection than the face sheets, which results in a different contact pressure, which is less uniform over the width as can be seen in figure 6.14. The assumption of the geometry of the cross sectional area probably influences this contact area. For this research an obround shape is assumed. This does not fully correspond to the edges of the drop-stitch panel in the experiments performed in chapter 4. The edges of the drop-stitch panel used in the experiments are flatter. The strip model neglects the effect of the non-uniform contact pressure over the width. Note that contact areas similar to figure 6.14a were observed for yarn spacing above 30 mm for the quarter panel. This could be one of the reasons that the slight difference in force-displacement response between the quarter and strip model as shown in figure 6.11.

(a) 30 mm yarn spacing
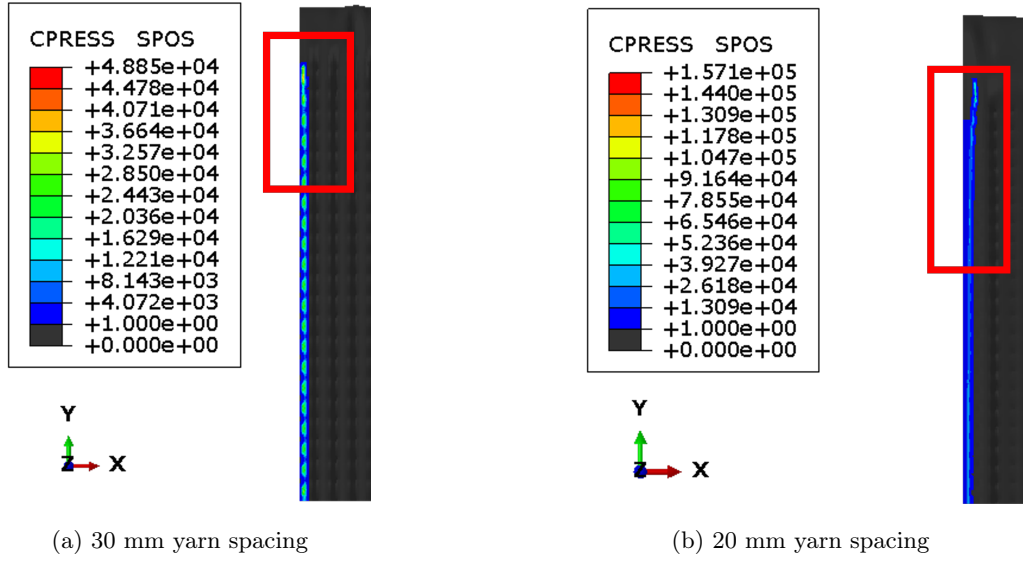
(b) 20 mm yarn spacing

Figure 6.14: Contact area of quarter model with yarn spacings of 20 and 30 mm around 0.3 m displacement.

In appendix D, the stresses in the xx-direction are shown at the load region of the quarter model for δ_{yarn} is 20 and 30 mm. At the folding failure mechanism, a downwards fold is at larger displacements generated. This can also seen in figures D.1-D.4. At some deflection, an almost uniform compressive stress over the width in the xx-direction appears, which is the upward fold left of the downward fold in figure 6.10a. The downwards fold does not arise at a yarn spacing of 30 mm as shown in figures D.5-D.8, which illustrates a significant difference between the local folding and global wrinkling failure mode clearly.

The force-displacement curves for $\delta_{yarn} = [6, 10]$ mm are similar. It is expected that this is due to the fact that the initiation and propagation of the fold is comparable. Figure 6.15 shows that the folding pattern is comparable. This folds are probably affected by the scaling method used for the yarn properties as discussed in section 6.1.2.

(a) $\delta_{yarn} = 6$ mm

(b) $\delta_{yarn} = 10$ mm
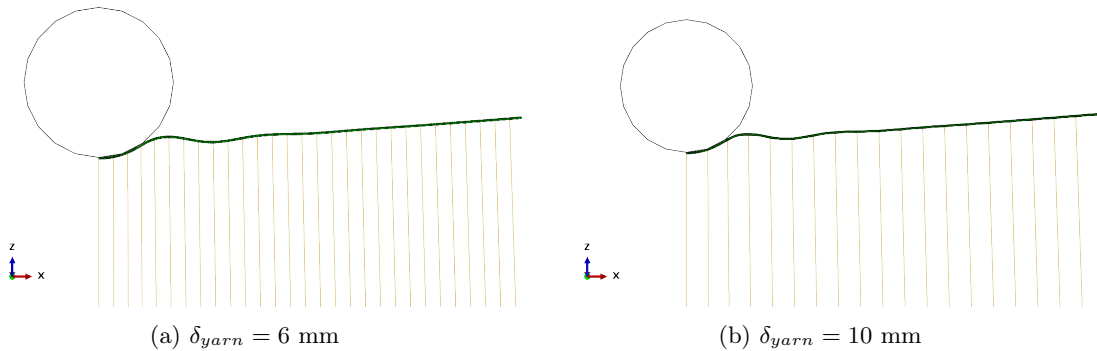
Figure 6.15: The folds generated in the load region using the strip model with LEO 1 material model, $P = 15$ kPa, $t_{face} = 0.0007$ and $\delta_{yarn} = [6, 10]$ mm. It shows that the wrinkling length is quite similar, which could be the reason that 6 and 10 mm force-displacement curves are corresponding in figure 6.11.

6.2.3 Influence of the face sheet thickness

To evaluate the influence of the face sheet's thickness on the global bending stiffness and failure modes, a set of face sheet thickness has been evaluated with the strip model. In section 6.2.2, a transition has been observed between a yarn distances 20 and 30 mm, so in this section a yarn distance of 20 and 30 mm will be used to evaluate whether the face sheet thickness has influence on the failure mode. Note that only the face sheet's thickness and yarn distance have been changed and that the rest of the parameters are as in section 6.2.2. This will give insight in the influence of the face sheet thickness on the bending stiffness and failure mechanism. The force displacement curves are shown in figure 6.16 and 6.17.

A difference in failure mode is observed for different face sheet thicknesses. In figure 6.16, the 1 and 0.7 mm thick face sheets has a folding failure mode and the 0.7 and 0.5 a global wrinkling failure mode. In figure 6.17, the 1 mm thick face sheets has a folding failure and the 0.7 and 0.5 global failure mode. This suggests that the face sheet thickness does influence the failure mode, since it increases the bending stiffness of the face sheet. The initial displacements differs for different thicknesses, since the mass is changed by changing the thickness of the face sheet. The density has not been adjusted for different face sheet thicknesses.
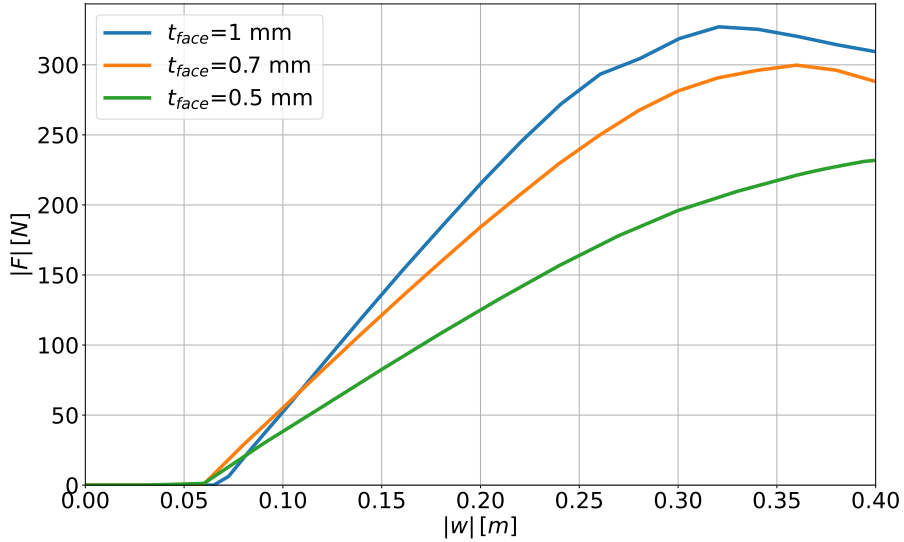
Figure 6.16: Force-displacement curves of strip model's load beam with $\delta_{yarn} = 20$ mm, $P = 15$ kPa and LEO1 material model for different face sheet thicknesses.
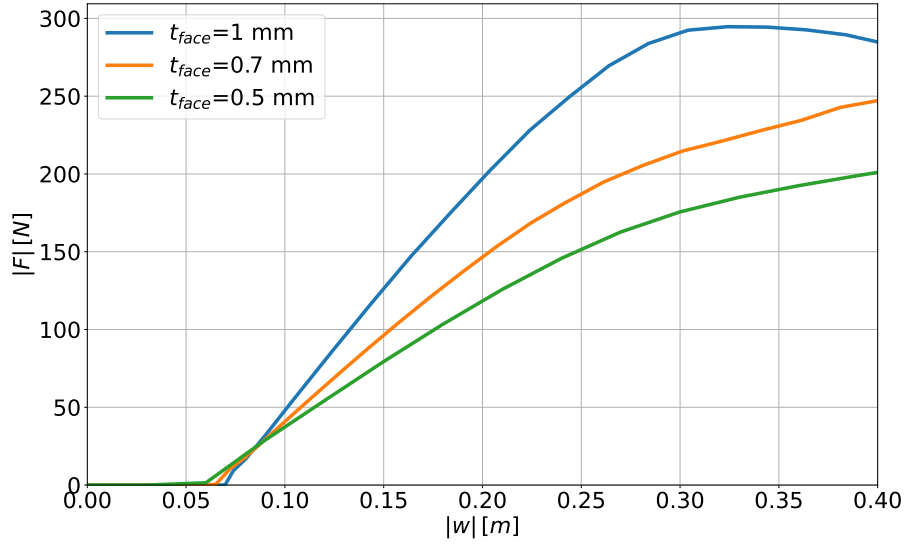
Figure 6.17: Force-displacement curves of strip model's load beam with $\delta_{yarn} = 30$ mm, $P = 15$ kPa and LEO1 material model for different face sheet thicknesses.

6.2.4 Influence of the internal air pressure

A set of internal air pressures has been evaluated for the 20 and 30 mm yarn distance strip models. This gives a better understanding in their influence on the structural response and failure modes. Note that only the internal air pressure and yarn distance have been changed and that the rest of the parameters are as described in section 6.2.2. An internal air pressure of 7, 15 an 30 kPa has been evaluated. This resulted in the force displacement curves as shown in figure 6.18 and 6.19.

It clearly depicts that the internal air pressure influences the bending stiffness. At low internal air pressures, the folding failure mode is initiated as can be observed in the 7 and 15 kPa for the 20 mm yarn spacing and 7 kPa for the 30 mm yarn spacing models. The global wrinkling mode is initiated at higher internal air pressures, whereas the local folding failure mode is initiated at lower internal air pressures.
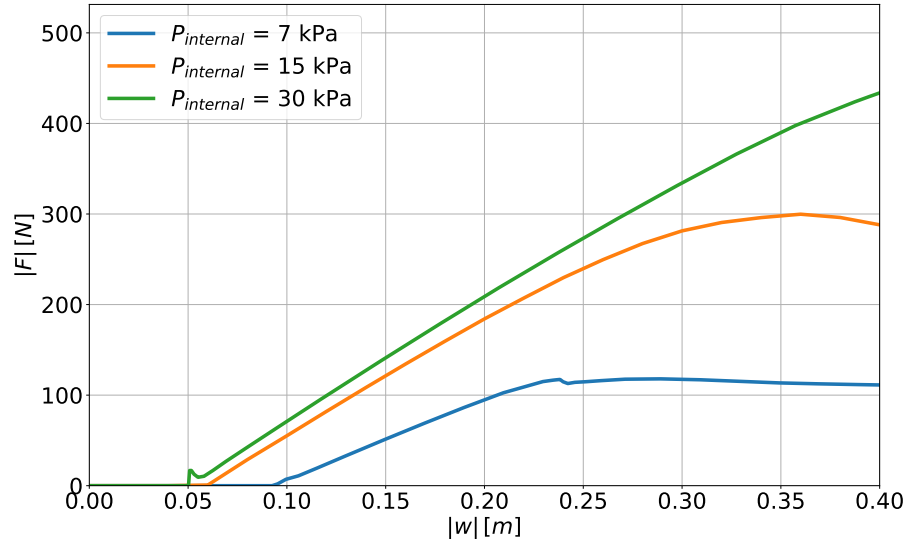
Figure 6.18: Force-displacement curves of strip model's load beam with $\delta_{yarn} = 20$ mm, $t_{face} = 0.7$ mm and LEO1 material model for different internal air pressures.
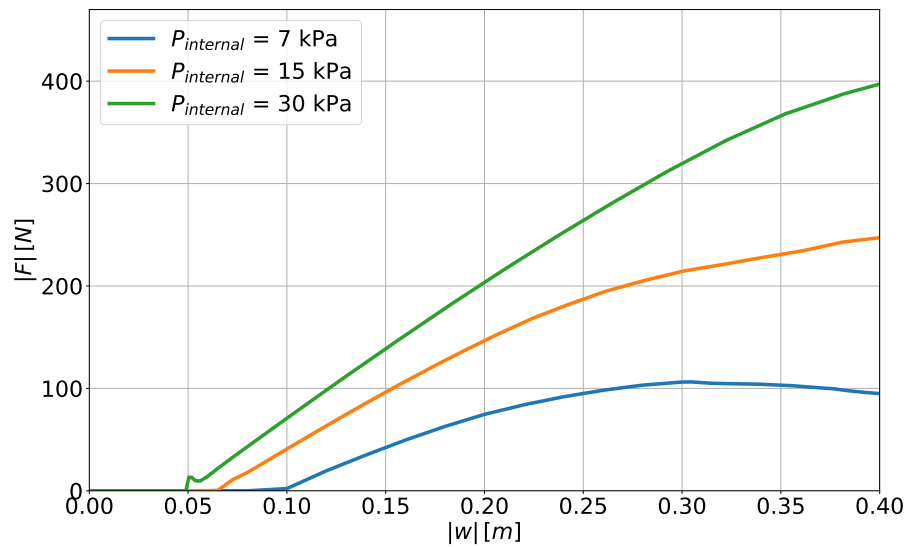
Figure 6.19: Force-displacement curves of strip model's load beam with $\delta_{yarn} = 30$ mm, $t_{face} = 0.7$ mm and LEO1 material model for different internal air pressures.

6.2.5 Influence of the material model

The influence of the orthotropic linear elastic material models 1 and 2 and FO model of chapters 5 on the structural response has been compared for an internal air pressure of 15 kPa and yarn distances of 20 and 30 mm. The other parameters of the strip model are as described in section 6.1. The force-displacement results are shown in figure 6.20 and 6.21. It shows that the bending stiffness is highly dependent on the material model. A change in failure mode is not observed for these material models. This does not imply that the initiation of a failure mode is independent of the material model. The linear elastic orthotropic material model 1 is significantly stiffer than linear elastic orthotropic material model 2. Strains around 3.4% are observed, which is slightly higher than expected in chapter 5. So, LEO1, which is fitted in the toe region, does not suffice for validation, since it underestimates the material stiffness.

The FO model with a yarn spacing of 20 mm is a less stiff than the linear elastic orthotropic 2 material model, but slightly stiffer after the maximum load has been applied. Probably due to the exponential behaviour of the FO model, the face material stiffness becomes stiffer than the linear elastic orthotropic 2 material model due to an increase in strain the wrinkled region. Convergence issues arose for the Fung Orthotropic material model with a yarn spacing of 30 mm. The local strains are slightly higher than the expected strain range of chapter 5, which was 2.5%. The maximum observed nominal strain in the simulations with the Fung Orthotropic material model and a yarn distance of 30 mm is 2.8% in the x-direction and 3.2% in the y-direction. For 20 mm yarn spacing, the maximum nominal strain is 2.6% in the x-direction and 3.2% in the y-direction. This still seems reasonable, so high strains are not the reason for the convergence issue. The exact reason for the convergence issue is unknown.
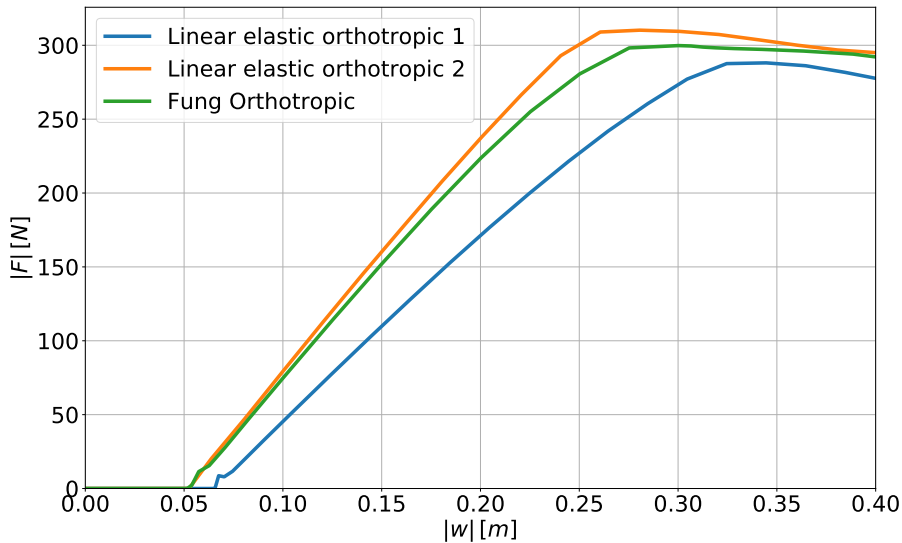
Figure 6.20: Force-displacement curves of strip model's load beam with a $\delta_{yarn} = 20$ mm, $t_{face} = 0.7$ mm and $P = 15$ kPa for different material models.
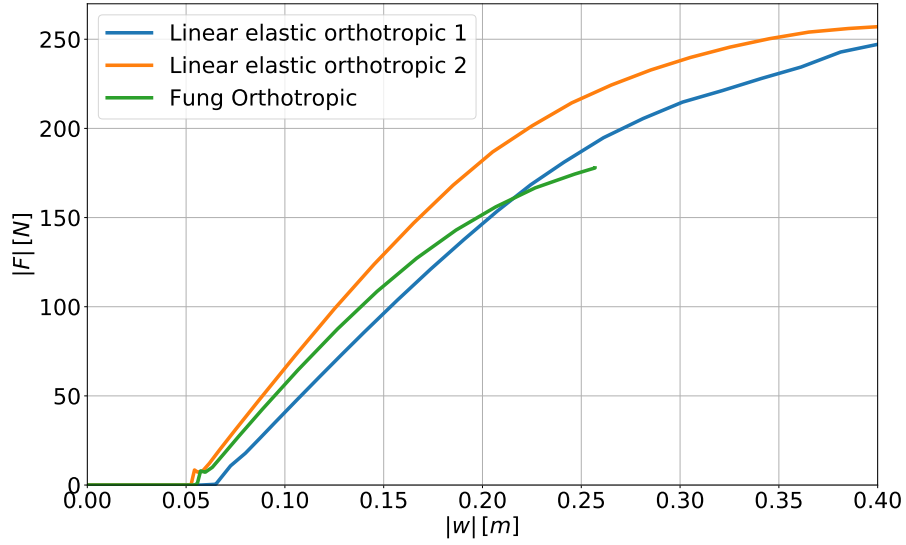
Figure 6.21: Force-displacement curves of strip model's load beam with a $\delta_{yarn} = 30$ mm, $t_{face} = 0.7$ mm and $P = 15$ kPa for different material models.

6.2.6 Validation

The experiments of chapter 4 are used to validate the numerical model. The strip model has been used with a yarn spacing of 6 mm, face sheet thickness of 0.7 mm, air pressure of 15 kPa and linear elastic orthotropic 2 material model. The dimensions are used are based on the geometry shown in figure 4.1. Figure 6.22 shows the numerical model used for validation.
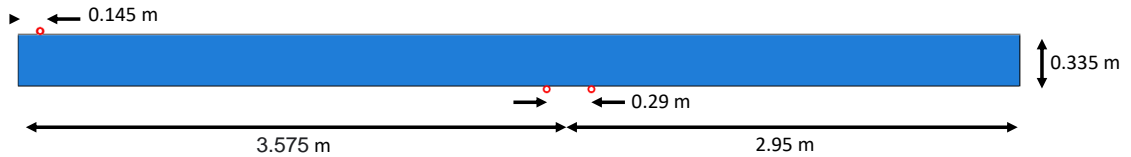
Figure 6.22: Geometry of the numerical model used compare with the experiments of chapter 4 based on the geometry depicted in figure 4.1

As mentioned in chapter 4, the tangential friction might have influenced the results. The model with tangential friction and without tangential friction has been compared with each other. The tangential friction is dependent on the strain rate, contact materials, pressure and temperature [123]. The strain rate in a quasi-static load case is close to zero, so the friction is independent of the strain rate. Friction might also be direction dependent [124]. The PVC layer of the face sheets is in contact with the trusses, which results in a friction between a steel and PVC layer. The tangential friction behaviour depends on the type of PVC and steel used [125]. Since the exact materials are unknown, a exact tangential friction model can not be implemented in the FE model. So, a tangential friction $\mu = 0.5$ has been assumed comparable with the values of Xinwu et al. [125].

The comparison between the experimental and numerical results for $P = 15$ kPa is shown in figure

6.23. The slope force-displacement of the strip model with $\mu = 0.5$ shows good agreement. The slope of the force-displacement without tangential friction is slightly lower than the measurements. This means that the bending stiffness pre-failure is similar to the experiments. The initial deflection of the strip model differs from the experiments. The initial deflection of the experiments was influenced by the tangential friction as discussed in chapter 4. A difference of ± 4 cm is observed during the hysteresis assessment, which is comparable to the difference in initial deflection in figure 6.23. This implies that depending on how the drop-stitch panel is placed on the support trusses, the initial deflection differs. The maximum load applied during the experiments was close to the failure load. The strip model did not wrinkle around 0.5 m displacement, which suggests that the stiffness overestimated.
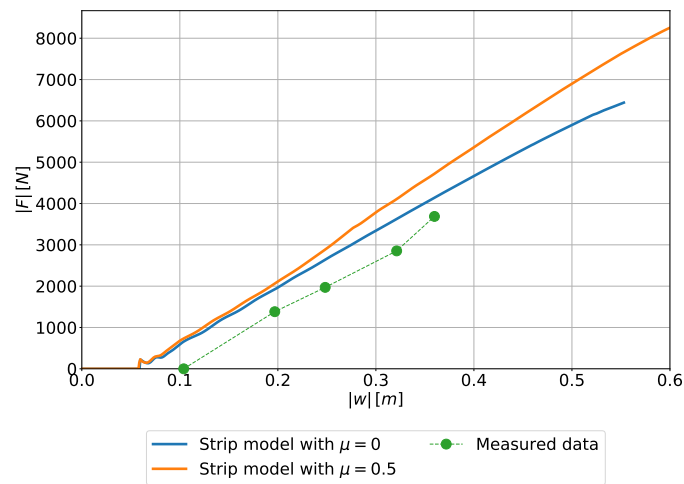
Figure 6.23: The experimental and numerical force-displacement behaviour for $P = 15$ kPa. The strip model with $\mu = 0$ is aborted preliminary.

The force-displacement curve for $P = 10$ kPa and $\mu = 0.5$ is shown in figure 6.24. It shows that the drop-stitch floater of the FEA collapses at a higher displacement than the measurements, which suggests that the pretension or stiffness is overestimated.
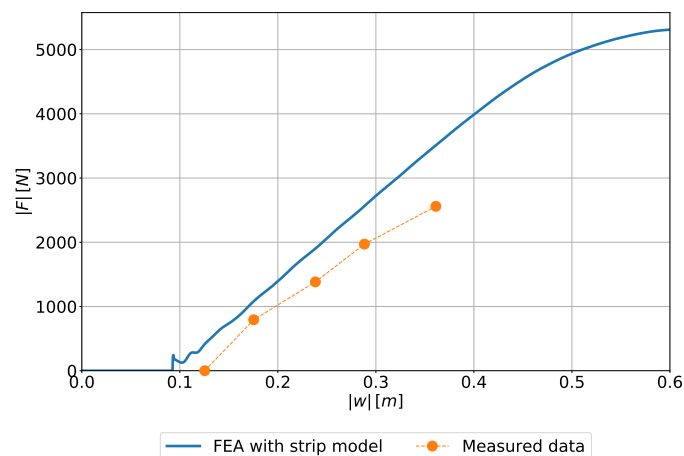
Figure 6.24: The experimental and numerical force-displacement behaviour for $P = 10$ kPa and $\mu = 0.5$.

6.3 Conclusions

A three point bending test on a drop-stitch panel has been conducted using FEA. The yarn spacing, face sheet thickness, material model and internal air pressure have been adjusted to gain insight in the bending characteristics and structural response. Two types of models has been evaluated: a strip and a quarter model. The quarter model assumes the drop-stitch panel has two symmetry planes in the xz- and yz-plane in a three point bending load case, which results in the assumption that only a quarter has to be modelled. The strip model is a simplification of the quarter model. It consists of an upper and lower face sheet with the width of one yarn spacing. The influence of the closing edges of the drop-stitch panel and non-uniform response over the width is neglected. Good correlation between both models is found.

The FEA showed that there are two failure modes for a three point bending test: a global wrinkling and a local folding failure mode. Both failure modes shows distinct behaviour. The global wrinkling failure mode has a wrinkling length of one yarn spacing and the folding failure mode of one or multiple multiple yarn spacings. The folding failure mode is initiated at low air pressures, large thicknesses and small yarn spacings. This suggest that the pretension, compressibility of the fluid, bending stiffness and characteristic length of the face sheets is significant for the initiation of the failure modes.

The bending stiffness of the face sheets is important. Especially, the initiation of failure modes is dependent on the face sheets' bending stiffness. Neglecting the bending stiffness by assuming membrane elements, would be incorrect. For very large yarn spacing and small thicknesses, membrane elements might suffice, if it appears that the bending stiffness is negligible for the global wrinkling failure mode. The influence of membrane elements is not evaluated during this research.

The yarn stiffness is scaled with the yarn distance to ensure that the drop-stitch panel maintains approximately the same thickness. It can be noticed that at small yarn spacings, the stiffness of the yarn spacings decreases and the length of the folds is more than one yarn spacing. This shows that the yarn stiffness might influence the results as the wrinkling amplitude is dependent on the yarn stiffness. An evaluation of the material properties of the yarns should be performed to ensure a realistic wrinkling behaviour. For the global wrinkling failure mode, it is not expected to have a significant influence on the wrinkling amplitude as the wrinkling length is equal to one yarn distance. A change in yarn stiffness affects the thickness of the panel, which might influence the initiation of the global wrinkling failure mode.

The correction factor N_{ratio} to correlate the results of the strip model to the quarter model differs per failure mode. A correction factor is established based on the difference in bending stiffness. For the global wrinkling failure mode, a correction factor is established based on the assumption that the bending stiffness is solely dependent on the contribution of the face sheets. The strip model showed similar force-displacement behaviour for the global wrinkling failure mode using this correction factor. For the folding failure mode, the bending stiffness contribution of the edges is taken into account, which gives a better correlation between the strip and quarter model. However, this has only been verified for one case, which is for 20 mm yarn spacing, 15 kPa internal air pressure and LEO1 material model. As mentioned in this load case, the load beam first contacts the edges instead of the face sheets, so this could have influenced the results. More cases should be investigated whether this assumption is true and/or more accurate correction factors can be established.

The material models showed a significant influence on the structural response. The assumption of a maximum of 2.5% strain of chapter 5 is too strict, since locally higher strains around 3.4% are observed. Using LEO2 material model for the validation resulted in a good agreement with the measurements for the pre-failure region of the force-displacement curves. The failure

force-displacement behaviour has not been measured, so it is not possible to validate the failure region.

The stiffness of the FE model shows a good agreement with the experiments performed in chapter 4. A difference in initial deflection is observed, which is probably due to the tangential friction of the supports. The way the drop-stitch floater is placed on the supports might have influenced the initial deflection. Also, the face sheets in the FEA are too stiffly implemented, since they do not wrinkle around the maximum load applied during the experiment. Increasing the initial perturbation might give more realistic result. Changing the yarn distance, could be a methodology to increase the initial perturbation. This behaviour is similar to column buckling simulations. If one would perform a column buckling analysis, an initial deflection needs to be applied to obtain realistic results as shown in figure 6.25.
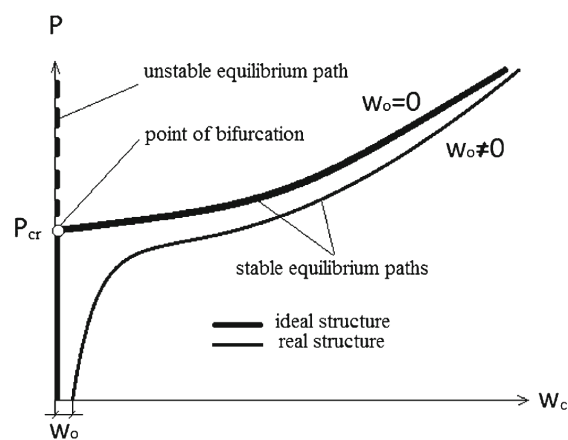
Figure 6.25: Typical equilibrium paths of a column without initial imperfections and of a real structure with initial imperfections [126].

Chapter 7

Conclusions

In this research, the bending characteristics of drop-stitch floaters are analysed. It provides more insight in the bending response of drop-stitch floaters. The amount of research performed on the structural characteristics of drop-stitch floaters is is limited. Especially, low pressurised drop-stitch floaters has not been researched yet to the best of the author's knowledge. This results in the main question of this research:

What are the relevant bending characteristics of a low pressurised drop-stitch panel?

The bending stiffness is influenced by four types of non-linearities: a load, geometrical, deformation and material non-linearity. This research mainly focused on obtaining insight in the material non-linearity due to hyperelasticity and geometrical due to wrinkling. A structural analysis of a drop-stitch panel subjected by a three point bending load case has been performed using an experimental and FE analysis. Following, the subquestions are answered, which are needed to answer the main questions:

1. **How could a drop-stitch panel be modelled using 3D FEM?**

   A drop-stitch panel is modelled as a quarter and a strip. The strip model does not take into account the effects of the edges of the panel and assumes an uniform response over the width of the panel. The results of the strip model corresponds with the quarter model, which suggest that for a uniaxial bending load case the strip model suffices. To incorporate wrinkling effects, the initial air pressure combined with the yarns provide enough perturbation to initiate wrinkling. It has been shown that the bending stiffness of the face sheets is significant for the wrinkling initiation and propagation, so the usage of membrane elements is incorrect and shell elements should be used. A tension field theory has not been investigated to model the influence of wrinkling. The force-displacement of the FE model shows good agreement with the experiments. A difference in the initial deflection has been observed. It is expected that this is mostly due to the tangential friction of the support trusses during the experiments. Also, the FE model did not fail around the maximum load of the experiments, which suggests that the FE model is too stiffly model. Applying a larger initial perturbation could give more realistic results.

2. **What is the influence of internal air pressure, thickness of the face sheet and yarn distance on the bending and wrinkling response of a drop-stitch panel?**

   The internal air pressure, thickness of the face sheet and yarn distance influences the bending stiffness and wrinkling behaviour. Highly pressurised drop-stitch panels have a larger bending stiffness and collapse with a global wrinkling failure mode. Lower internal air pressures tend to have a lower bending stiffness and a folding failure mode. The internal air pressure influences the pretension in the face sheets and the work required to compress the internal air volume. The higher the internal air pressure, the higher pretension and work required to compress the internal air volume.

   An increase in the thickness of the face sheets, increases the bending stiffness of the face sheets predominantly. This results in a higher global stiffness, but also in a difference in failure mode. At larger face sheet thicknesses, the face sheet is able to withstand the internal air pressure and initiate a downwards fold.

The yarn distance changes the characteristic length and yarn properties in the FE model. At larger yarn distances, more work is required to withstand the internal air pressure and initiate a downwards fold.

3. **What is material behaviour of the face sheets?**

   The stress-strain behaviour of polyester fiber coated with PVC has shown to be an orthotropic hyperelastic material. Different material models (linear elastic and hyperelastic) have been evaluated. Better fits can be obtained, but would require establishing and implementing a new material model or a different fitting procedure. The FEA showed a good agreement with a linear elastic orthotropic material model, so whether hyperelasticity is significant for the global response can be argued. It slightly influences the global bending stiffness, but for engineering purposes a linear orthotropic material model might suffice for low pressurised drop-stitch panels.

4. **What is the mechanism behind the bending behaviour?**

   The bending stiffness of a drop-stitch panels is influenced by four non-linearities: hyperelasticity, pressure-volume work, hyperelasticity and a displacement non-linearity at large deflections. Pressure-volume work and the displacement non-linearity has shown to be significant by prior research. Hyperelasticity does not influence the bending stiffness significantly, so a linear stiffness approximation might suffice. Wrinkling has already been shown to be a significant non-linearity in prior research. A clear distinction between wrinkling pattern has not been made yet. This research has shown that two different types of wrinkling initiate a different failure mode: a local folding and a global wrinkling failure mode. In the local folding failure mode a downward fold is initiated and in the global wrinkling failure mode the initial perturbations due to the internal air pressure are increased.

So, the relevant bending characteristics of a low pressurised drop-stitch panel are dependent on the bending stiffness of the face sheets, yarn spacing, internal air pressure and material model. These parameters have shown to influence the eventual bending behaviour. A low pressurised drop-stitch panel has shown to have a non-linear elastic bending stiffness at large displacements due to wrinkling, pressure-volume work and large deflections. Hyperelasticity has not shown to have a significant influence on the global response in a three point bending load case and a linear approximation of the material stiffness might suffice. Two different failure modes are possible in a pure bending load case: a local folding and a global wrinkling failure mode. The initiation of the two failure modes depends on the bending stiffness of the face sheets, yarn spacing and internal air pressure.

Recommendations

In this chapter, recommendations for future research are suggested. The recommendations are subdivided into fundamental research, which focuses on gaining knowledge on a topic, and applied research, which covers research into the practical usage of drop-stitch panels in an offshore environment.

8.1 Fundamental research

During this research, a knowledge gap has been observed on the following topics: the material behaviour, limit states and scaling laws, structural models and fluid-structure interaction (FSI).

8.1.1 Material behaviour

The material behaviour of polyester fibers coated with PVC is very complex to describe, since it is orthotropic and hyperelastic at low strains. This research did not investigate the interaction in stress-strain behaviour in different directions, which should be measured to accurately analyse the material behaviour. Performing a biaxial tensile test provides more information about the multiaxial stress-strain behaviour. Digital image correlation could be useful to analyse the full strain field. Applying strain gauges is difficult at large strains and does not provide the full strain field.

Current material models can not describe the stress-strain relation in different directions exact. A combination material models might be able to model the material stiffness more accurate. However, this a blunt approach, since one would lose the physical meaning of the variables of the material models. Also, the interaction between stress-strain in different directions might be difficult to accurately fit, if one would use a combination of different material models. The Ogden model does model higher order non-linear stress-strain relations accurately, but it lacks a directional dependence and interaction. On the other hand, the HGO and FO model models the directional dependence properly, but lacks the higher order non-linear stress-strain relations. Establishing a higher order material model with directional dependence should be further investigated. Probably, this does create extra variables, which makes the fitting procedure more difficult. The least squares fitting procedure might become insufficient, since the found minimum is highly dependent on the boundary conditions variables. So, the found minimum does not have to be global minimum. An exact optimisation technique such as the Newton's or gradient method should be used to guarantee finding the global minimum [127].

8.1.2 Limit states and scaling laws

Obtaining more insight in the limit states is needed to ensure the reliability of drop-stitch floaters in offshore conditions. In this research, a folding and global wrinkling failure mode has been observed. A combination of energy formulations used to analyse folds in membranes supported by a fluid and wrinkling in membranes subjected by an uniaxial load might be usable [55, 56, 58]:

$$U = U_s + U_b + U_p$$

with U_s is the strain energy, U_b the bending energy and U_p the potential energy of the fluid. It has been shown in this research that these three energy components might be influential for the failure mode. The potential energy of the yarns might also need to be included in this formulation.

A non-dimensionalised pressure-bending energy ratio C_{pb} might be used to predict the eventual failure mode. The usage of scaling laws can be a methodology to evaluate the initiation of failure modes. A possible methodology to establish C_{pb} is shown in appendix F. This resulted in:

$$C_{pb} = \frac{P\lambda^{3\frac{1}{2}}}{E_{xx}t_{face}^3\sqrt{H}}$$

with P is the internal air pressure, λ the wrinkling length, E_{xx} the Young's modulus in the xx-direction, t_{face} the face sheet thickness and H the height of the panel. This already shows that the global wrinkling failure mode is initiated at $C_{pb} \geq 1.12$ and the folding failure mode at $C_{pb} \leq 1.08$ as shown in figure 8.1. Between 1.08 and 1.12 there might be a transition of failure modes.
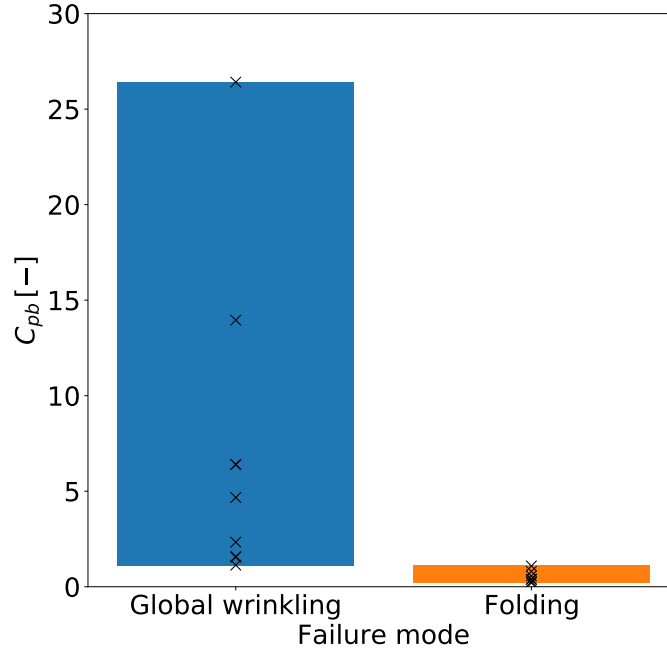
Figure 8.1: The non-dimensional pressure-bending energy ratio C_{pb} for the global wrinkling and folding failure mode.

Figure 8.1 shows that it has a potential interesting result. Whether this scaling law holds for all cases and is correct, should be further evaluated. Especially, the influence of the height of the panel has not been investigated in this research, so it is not clear whether C_{pb} should scale with $1/\sqrt{H}$ and $\lambda^{3\frac{1}{2}}$. There are different possibilities to establish a pressure-bending energy ratio. Developing a C_{pb} which is correct for all cases, creates a better understanding in the initiation of the failure modes.

The force of the load beam seems to scale with the wrinkling length among other things by $F \sim \sqrt{\lambda}$ as shown in figure 8.2 with λ is the wrinkling length, which is equal to the yarn distances for $\delta_{yarn} \geq 20$ mm in the cases investigated in this research. The exact derivation, reason and correctness for this scaling should be further evaluated. This scaling might be usable to establish a limit state of the drop-stitch panel. The limit state might be a function of the initial perturbation,

which can be easily estimated with methodology described in appendix E. It seems that there are two different limit states for both failure modes according to figure 8.2. For the global wrinkling failure mode (30 mm $\leq \delta_{yarn} \leq$ 60 mm), there seems to be one limit for $F\sqrt{\lambda}$, which does not differ for the different yarn spacings. For the folding failure mode, a change of w at which the drop-stitch floater collapses and a slight change of maximum $F\sqrt{\lambda}$ is observed.
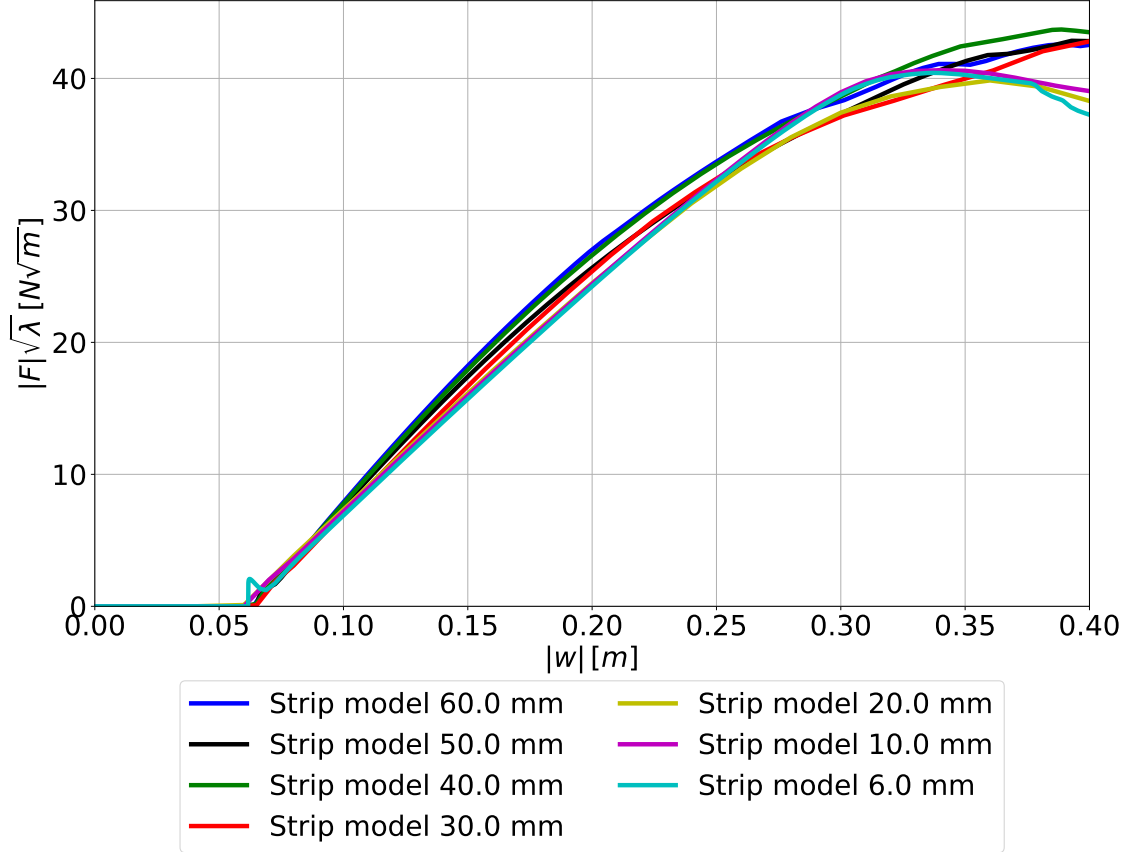
Figure 8.2: The force displacement curves for different yarn using the strip model with data of figure 6.11 and the force multiplied with λ^α with λ is the wrinkling length and α is a coefficient

8.1.3 Structural models

Establishing a structural model that is able to model the non-linear bending stiffness of a drop-stitch panel creates a fundamental understanding of the response in load cases and can greatly reduce calculation times. Davids et al. [32] made an FE model based on a modified version of the Timoshenko beam model, which is able to capture the response in uniaxial load cases of high pressurised drop-stitch panels. Their assumptions regarding wrinkling effects might difficult to extrapolate to a plate model. They assumed a tension only material property, integrated over a constant cross sectional area to determine the stress distribution over the thickness and establish a moment-curvature relation. Assuming a constant cross sectional area, might not suffice in multiaxial load conditions. More research should be performed to formulate structural models usable for drop-stitch panels.

Davids et al. [32] acquired a good agreement with experiments for the force-displacement behaviour by assuming a Timoshenko beam. However, assuming a homogeneous beam/plate might underestimate the stresses occurring in the face sheets, since the stress is distributed over

the full height of the panel instead of solely the face sheets' thickness. A possibility to establish a structural model of the drop-stitch floater might be adopting the classical laminate theory (CLT). The original CLT is evaluated in section 2.5. Especially for small yarn distances (6 and 10 mm), internal air volume and yarns seems to act as a core material, since they give a certain height to drop-stitch panel, an additional stiffness and a flat shape. For large yarn spacings, it might be difficult to use the CLT, since a flat shape can not be assumed anymore. A modified CLT might be established to take into account transverse shear, wrinkling, pressure-volume work and the influence of the yarns. Following, a few suggestions for the modified CLT are elaborated. Note that these suggestions are not verified/validated, so it is unknown whether they will work out.

First of all, transverse shear should be taken into account by modifying the kinematics of the original CLT model. Yang et al. [128] established a two dimensional linear theory for heterogeneous plates, which has been further investigated by Whitney and Pagano [129]. Reddy et al. [130] took into account a parabolic shear strain distribution. Whether a parabolic shear strain distribution generates significantly more accurate results, is unknown for a drop-stitch floater. For the suggestions, a linear shear strain distribution is assumed. The transverse shear stress is added to the constitutive equation of each layer [129]:

$$
\begin{bmatrix} \sigma_x \\ \sigma_y \\ \tau_{xy} \end{bmatrix} = \begin{bmatrix} c_{11} & c_{12} & c_{16} \\ c_{12} & c_{22} & c_{26} \\ c_{16} & c_{26} & c_{66} \end{bmatrix} \begin{bmatrix} \epsilon_x \\ \epsilon_y \\ \gamma_{xy} \end{bmatrix}
$$
$$
\begin{bmatrix} \tau_{yz} \\ \tau_{xz} \end{bmatrix} = \begin{bmatrix} c_{44} & c_{45} \\ c_{45} & c_{55} \end{bmatrix} \begin{bmatrix} \gamma_{yz} \\ \gamma_{xz} \end{bmatrix}
$$

where c_{ij} are the elastic stiffness components in the global direction of a ply. The kinematics are as described according the Mindlin plate theory as [128]:

$$
u = u^0(x, y, t) + z\psi_x(x, y, t)
$$
$$
v = v^0(x, y, t) + z\psi_y(x, y, t)
$$
$$
w = w(x, y, t)
$$

The ABD-matrix is modified by including the transverse shear stiffness components:

$$
\begin{bmatrix} N_x \\ N_y \\ Q_y \\ Q_x \\ N_{xy} \\ M_x \\ M_y \\ M_{xy} \end{bmatrix} = \begin{bmatrix} A_{11} & A_{12} & A_{14} & A_{15} & A_{16} & B_{11} & B_{12} & B_{16} \\ & A_{22} & A_{24} & A_{25} & A_{26} & B_{12} & B_{22} & B_{26} \\ & & A_{44} & A_{45} & A_{46} & B_{14} & B_{24} & B_{46} \\ & & & A_{55} & A_{56} & B_{15} & B_{25} & B_{56} \\ & & & & A_{66} & B_{16} & B_{26} & B_{66} \\ & & & & & D_{11} & D_{12} & D_{16} \\ & Sym. & & & & & D_{22} & D_{26} \\ & & & & & & & D_{66} \end{bmatrix} \begin{bmatrix} \varepsilon_x^0 \\ \varepsilon_y^0 \\ \varepsilon_{yz}^0 \\ \varepsilon_{xz}^0 \\ \varepsilon_{xy}^0 \\ \kappa_x \\ \kappa_y \\ \kappa_{xy} \end{bmatrix}
$$

The contribution of the face sheets in the pre-wrinkling phase to the ABD-matrix can be derived by equations 2.14-2.20 except for the transverse shear stiffness components. It is expected that the internal air pressure and yarns do not provide any in-plane stiffness in the underformed state. However, if shear arises in the drop-stitch panel, the yarns might influence the in-plane stresses as shown in figure 2.18, since an inplane stress component arises, which is transmitted to the face sheets. Also, the yarns do contribute to the transverse shear stiffness. It is expected that the transverse shear stiffness is mainly dependent on the yarn's Young's modulus, cross sectional area and spacing.

Wrinkling might be incorporated in a structural model by assuming the tension field theory for the face sheets. Davids et al. [32, 88] assumes that a wrinkled face sheet does not contribute to the stiffness and causes a shift of the neutral axis. Determining the shift of the neutral axis

caused by the wrinkled face sheet in a plate model is more difficult than in a beam model, since the stress/strain state differs over the width/cross-sectional area. How to determine the change in neutral axis in a 2D model, should be further investigated. It might be possible to incorporate wrinkling without the implementation of a shift of the neutral axis by decreasing the stiffness contribution of the wrinkled face sheet to the ABD-matrix. This would require a further analysis of the bending response of drop-stitch panels and establish non-linear moment-curvature and force-strain relations, which could be implemented in the ABD-matrix.

The internal air creates a pretension in the face sheets and causes a pressure-volume work contribution in the virtual work balance. The pretension might be added as a residual stress in the constitutive equation of the face sheets as:

$$
\begin{bmatrix} \sigma_x \\ \sigma_y \\ \tau_{xy} \end{bmatrix} = \begin{bmatrix} \sigma_{x,1} + \sigma_{x,0} \\ \sigma_{y,1} + \sigma_{y,0} \\ \tau_{xy,1} + \tau_{xy,0} \end{bmatrix}
$$

where $\sigma_{x,0}$, $\sigma_{y,0}$, $\tau_{xy,0}$ are the stresses in the initial state caused by the pretension and $\sigma_{x,1}$, $\sigma_{y,1}$, $\tau_{xy,1}$ the stresses induced by a load case. The pressure-volume work should be included in the virtual energy work balance. The virtual pressure-volume work as described by Davids et al. [32, 88] and discussed in section 2.5 might be extrapolated to 2D by including the shear in the yz-plane and curvature in the y-direction.

8.1.4 FSI

A fluid-structure interaction analysis will provide more information on the response of drop-stitch floaters in wave conditions. It gives more knowledge about the load conditions and deformations in offshore conditions. This might be used to evaluate the limits in an offshore environment of drop-stitch floaters. Also, the interaction between multiple drop-stitch floaters, mooring and slamming effects should be analysed.

Xu et al. established an FSI model based on a Euler Bernoulli-von Kármán beam model and potential flow fluid to model large scale scale FPVs [131]. However, their assumption of an Euler Bernoulli beam is not applicable for drop-stitch floaters, since shear deformations can be significant and wrinkling effects should be incorporated at larger deformations for low pressurised drop-stitch panels. Also, they have assumed a membrane type structure, which is not applicable for drop-stitch floaters, since the bending stiffness is significant.

A coupled CFD-FEM simulation is possible, but it is expected to be computationally intensive. Especially if one is interested in analysing the response of a drop-stitch floater in multi-axial wave conditions, it is expected to very computationally intensive, since it is not possible to analyse the response using the strip method used in this research. Structural plate models as described in this chapter could reduce the computation times.

8.2 Applied research

The applied research recommendations focuses on the practical application drop-stitch floaters in an offshore environment as an FPV. The following recommendations are discussed: experiments in an offshore environment, influence of solar panels and engineering approaches.

8.2.1 Experiments in offshore environment

The performance of drop-stitch panels in an offshore environment are currently unknown. Drop-stitch floaters are expected to be a very efficient structure, since their stiffness mostly generated by air, which has a low density. Also, the transportation of drop-stitch floaters is

expected to be very efficient, since they can be transported in a deflated state. So, it is a very promising structure for the usage as FPV. The response of drop-stitch floaters in offshore conditions is not tested yet and should be evaluated to ensure the reliability. Also, the efficiency of the solar panels needs to be investigated in an offshore condition using drop-stitch floaters. Water provides a cooling effect to the PV system, which increases the efficiency of an FPV compared to a land based PV system [132]. The influence of this cooling effect for drop-stitch floaters is unknown. Also, the influence of accretion and heat generated by the PV system should be investigated on the structural response and PV system. The PV system influences the stiffness of the face sheets and also adds mass to the drop-stitch floaters. This might influence the bending response.

8.2.2 Regulations and engineering approaches

Current regulations provided by DNV for FPV systems do not suffice for drop-stitch floaters, since it assumes a rigid FPV system [30]. Low pressurised drop-stitch floaters are flexible floaters, so the regulations have to be revised to ensure the reliability of the FPVs. This is usable for engineers to evaluate whether their drop-stitch floater design is considered to be safe and reliable for the usage as FPV. To accomplish new regulations, engineering approaches might help to quickly perform a feasibility study on a concept design. Engineering approaches can be analytical, empirical or a simplified FEA. The strip model has proven to be an accurate simplified FE model, but it might be further simplified. Applying a tension field theory might result in shorter calculation times, since coarser meshes can be used. However, low convergence rates are observed using the `*NO COMPRESSION` material property in `ABAQUS`, so this was not investigated in this research.

Bibliography

[1]   Saipem. *The New Frontiers of Renewables: Floating Solar*. 2020. URL: https://www.saipem.com/en/blog/new-frontiers-renewables-floating-solar (visited on 05/25/2021).

[2]   IPCC. *Climate Change 2007: Synthesis Report. Contribution of Working Groups I, II and III to the Fourth Assessment Report of the Intergovernmental Panel on Climate Change.* Ed. by Core Writing Team, R.K. Pachauri, and A. Reisinger. Geneva, Switzerland: IPCC, 2007.

[3]   IPCC. *Climate Change 2021: The Physical Science Basis. Contribution of Working Group I to the Sixth Assessment Report of the Intergovernmental Panel on Climate Change.* Ed. by V. Masson-Delmotte et al. United Kingdom and New York, NY, USA.: Cambridge University Press, 2021.

[4]   *Paris Agreement*. UNTC XXVII 7.d. Dec. 12, 2015.

[5]   IPCC. *Global Warming of 1.5° C.An IPCC Special Report on the impacts of global warming of 1.5° C above pre-industrial levels and related global greenhouse gas emission pathways, in the context of strengthening the global response to the threat of climate change, sustainable development, and efforts to eradicate poverty.* Ed. by V. Masson-Delmotte et al. 2018.

[6]   Rijksoverheid. *Klimaatakkoord.* Den Haag, Netherlands: Rijksoverheid, 2019. URL: https://www.klimaatakkoord.nl/binaries/klimaatakkoord/documenten/publicaties/2019/06/28/klimaatakkoord/klimaatakkoord.pdf (visited on 05/28/2021).

[7]   T. Bruckner et al. *Climate Change 2014: Mitigation of Climate Change. Contribution of Working Group III to the Fifth Assessment Report of the Intergovernmental Panel on Climate Change.* Ed. by O. Edenhofer et al. United Kingdom and New York, NY, USA.: Cambridge University Press, 2014.

[8]   World Bank Group, ESMAP, and SERIS. *Where Sun Meets Water: Floating Solar Market Report.* Washington, DC: World Bank Group, 2018. DOI: 10.1596/32804.

[9]   Alok S., Neha Y., and K. S. "Floating photovoltaic power plant: A review". In: *Renewable and Sustainable Energy Reviews* 66 (2016), pp. 815–824. DOI: 10.1016/j.rser.2016.08.051.

[10] H. Cleijne et al. *North Sea Energy Outlook (NEO).* Arnhem, Netherlands: DNV, 2020.

[11] Vijay Devabhaktuni et al. "Solar energy: Trends and enabling technologies". In: *Renewable and Sustainable Energy Reviews* 19 (2013), pp. 555–564. DOI: 10.1016/j.rser.2012.11.024.

[12] S. Z. Golroodbari and W. van Sark. "Simulation of performance differences between offshore and land-based photovoltaic systems". In: *Progress in Photovoltaics: Research and Applications* 28.9 (2020), pp. 873–886. DOI: 10.1002/pip.3276.

[13] A. van Hoeken. *First high-wave offshore solar farm system since 2019 on the North Sea.* [Webinar]. Topsector Energie. Apr. 2021. URL: https://www.topsectorenergie.nl/agenda/webinar-zon-op-water (visited on 04/23/2021).

[14] T. Hooper, A. Armstrong, and B. Vlaswinkel. "Environmental impacts and benefits of marine floating solar". In: *Solar Energy* October (2020). DOI: 10.1016/j.solener.2020.10.010.

[15] T. Karpouzoglou, B. Vlaswinkel, and J. Van Der Molen. "Effects of large-scale floating (solar photovoltaic) platforms on hydrodynamics and primary production in a coastal sea from a water column model". In: *Ocean Science* 16.1 (2020), pp. 195–208. DOI: 10.5194/os-16-195-2020.

[16] M. Redón Santafé et al. "Theoretical and experimental analysis of a floating photovoltaic cover for water irrigation reservoirs". In: *Energy* 67 (2014), pp. 246–255. DOI: 10.1016/j.energy.2014.01.083.

[17] Kyocera. *Kyocera TCL Solar begins operation of Japan's largest 13.7MW Floating Solar Power Plant.* 2018. URL: https://global.kyocera.com/news-archive/2018/0301%5C_wvfh.html (visited on 04/10/2021).

[18] M. Mesbahi. *Top 100 Floating Solar Projects.* 2019. URL: https://www.solarplaza.com/channels/markets/11968/top-100-floating-solar-projects/ (visited on 04/08/2021).

[19] C. Campbell. *China: Builds Massive Floating Solar Panel Farm.* URL: https://time.com/china-massive-floating-solar-field/ (visited on 04/08/2021).

[20] C. Naschert. *With ambitions offshore, floating solar makes its first splashes in Europe.* 2020. URL: https://www.spglobal.com/marketintelligence/en/news-insights/latest-news-headlines/with-ambitions-offshore-floating-solar-makes-its-first-splashes-in-europe-59512639 (visited on 04/08/2021).

[21] Oceans of Energy. *A world's first: offshore floating solar farm installed at the Dutch North Sea.* 2019. URL: https://oceansofenergy.blue/2019/12/11/a-worlds-first-offshore-floating-solar-farm-installed-at-the-dutch-north-sea/ (visited on 04/08/2021).

[22] M. Willuhn. *The weekend read: Don't throw caution to the wind.* 2020. URL: https://www.pv-magazine.com/2020/02/22/the-weekend-read-dont-throw-caution-to-the-wind/ (visited on 04/08/2020).

[23] Topsector Energie. *Solar@Sea II.* URL: https://projecten.topsectorenergie.nl/projecten/solar-at-sea-ii-00033518 (visited on 03/23/2021).

[24] P. V. Cavallaro, C. J. Hart, and A. M. Sadegh. "Mechanics of air-inflated drop-stitch fabric panels subject to bending loads". In: *ASME International Mechanical Engineering Congress and Exposition, Proceedings (IMECE).* Vol. 9. American Society of Mechanical Engineers (ASME), 2013. DOI: 10.1115/IMECE2013-63839.

[25] World Bank Group, ESMAP, and SERIS. *Where Sun Meets Water: Floating Solar Handbook for Practitioners.* Washington, DC: World Bank, 2019. URL: http://documents.worldbank.org/curated/en/418961572293438109/Where-Sun-Meets-Water-Floating-Solar-Handbook-for-Practitioners.

[26] W. Otto. *Hydroelastic analysis of the Solar@Sea-II concept: Report No. 32510-1-RD.* [Unpublished]. Wageningen: MARIN, 2020.

[27] S. van Hoof. "Hydroelastic wave deformation of Very Flexible Floating Structures". MSc. Technische Universiteit Delft, 2020.

[28] 12Springs. *12SPRINGS Trampoline.* URL: https://www.12springstrampolines.nl/ (visited on 04/06/2021).

[29] SUP Planet. *Wat is drop-stitch? - Uitgebreide Uitleg.* 2020. URL: https://www.supplanet.nl/wat-is-drop-stitch/ (visited on 04/06/2021).

[30] DNV. *Design , development and operation of floating solar photovoltaic systems.* Tech. rep. Baerum: DNV, 2021.

[31] A. W. Hulton, P. V. Cavallaro, and C. J. Hart. "Modal analysis and experimental testing of air-inflated drop-stitch fabric structures used in marine applications". In: *ASME International Mechanical Engineering Congress and Exposition, Proceedings (IMECE).* Vol. 9. American Society of Mechanical Engineers (ASME), 2017. DOI: 10.1115/IMECE2017-72097.

[32] W. G. Davids, E. Waugh, and S. Vel. "Experimental and computational assessment of the bending behavior of inflatable drop-stitch fabric panels". In: *Thin-Walled Structures* 167 (2021), p. 108178. DOI: 10.1016/j.tws.2021.108178.

[33] T. McDaniel. *Flying Machine. U.S. Patent No. 1,905,298*: Washington, DC: U.S. Patent and Trademark Office. 1933.

[34] Goodyear Aircraft. *Engineering Report on the Development of a One-Place Inflatoplane*. AD-134 572. Arlington, VA: United States Department of Defense, 1957.

[35] J. Bowling. *The Weird Tale Of The Crash-Proof Inflatable Airplane*. 2020. URL: https://medium.com/focus-on-history/the-weird-tale-of-the-crash-proof-inflatable-airplane-24437a0fe556 (visited on 04/06/2021).

[36] S. Klare et al. "VacuuAir-A New Technology for High Performance Inflatable SUPs". In: *Procedia Engineering*. Vol. 147. Elsevier Ltd, 2016, pp. 556–561. DOI: 10.1016/j.proeng.2016.06.238.

[37] K. L. Apedo et al. "Nonlinear finite element analysis of inflatable beams made from orthotropic woven fabric". In: *International Journal of Solids and Structures* 47.16 (2010), pp. 2017–2033. DOI: 10.1016/j.ijsolstr.2010.03.030.

[38] W. G. Davids and H. Zhang. "Beam finite element for nonlinear analysis of pressurized fabric beam-columns". In: *Engineering Structures* 30.7 (2008), pp. 1969–1980. DOI: 10.1016/j.engstruct.2007.12.020.

[39] J. Loughlan et al. "Mechanics of Inflatable Fabric Beams". In: *4th International Conference on Thin Walled Structures*. Loughborough, United Kingdom, 2004, pp. 225–232. DOI: 10.1201/9781351077309-23.

[40] A. W. Turner, M. L. Peterson, and W. G. Davids. "Experimental methods to determine the constitutive properties of fabric inflatable structures". In: *American Society of Mechanical Engineers, Nondestructive Evaluation Engineering Division (Publication) NDE*. Chicago, Illinois, USA: ASME, 2006, pp. 1–4.

[41] C. G Malm et al. "Finite Element Analysis of Woven Airbeams". In: *ASME International Mechanical Engineering Congress and Exposition*. Chicago, Illinois, USA: ASME, 2006, pp. 5–7.

[42] J.A Main, S.W. Peterson, and A.M. Strauss. "LOAD-DEFLECTION BEHAVIOUR OF SPACE-BASED INFLATABLE FABRIC BEAMS". In: *Journal of Aerospace Engineering* 7.2 (1994), pp. 225–238.

[43] P. V. Cavallaro, A. M. Sadegh, and C. J. Quigley. "Contributions of Strain Energy and PV-work on the Bending Behavior of Uncoated Plain-woven Fabric Air Beams". In: *Journal of Engineered Fibers and Fabrics* 2.1 (2007). DOI: 10.1177/155892500700200102.

[44] J. K. Paik and A. K. Thayamballi. *Ultimate Limit State Analysis and Design of Plated Structures*. 2nd ed. Hoboken, NJ: John Wiley & Sons, Incorporated, 2018, pp. 7–17.

[45] Y. Liu et al. "The interactive bending wrinkling behaviour of inflated beams". In: *Proceedings of The Royal Society A* 472 (Sept. 2016), p. 20160504. DOI: 10.1098/rspa.2016.0504.

[46] S. L. Veldman. "Design and Analysis Methodologies for Inflated Beams". PhD thesis. Delft University of Technology, 2005.

[47] W. B. Fichter. *NASA Technical Note: A Theory for Inflated Thin-Wall Cylindrical Beams*. Tech. rep. MSU-CSE-06-2. Hampton, Virginia: Langley Research Center, June 1966.

[48] X. Li et al. "Review and perspective of materials for flexible solar cells". In: *Materials Reports: Energy* 1.1 (2020). DOI: 10.1016/j.matre.2020.09.001.

[49] MiaSolé. *Brochure: The Leader In Flexible, Powerful, Lightweight Thin-Film Solar*. 2018. URL: http://miasole.com/wp-content/uploads/2015/05/MiaSole_brochure_final.pdf (visited on 03/09/2021).

[50] C. Lungenschmied et al. "Flexible encapsulation for organic solar cells". In: *Photonics for Solar Energy Systems* 6197.May (2006). DOI: 10.1117/12.662829.

[51] X. Chen and S. Liu. "Mechanical testing and analysis of polymer based flexible solar cell and full cell packaging". In: *ICEPT-HDP 2011 Proceedings - 2011 International Conference on Electronic Packaging Technology and High Density Packaging* (2011), pp. 1138–1142. DOI: 10.1109/ICEPT.2011.6067028.

[52] A. L. Adler, M. M. Mikulas, and J. M. Hedgepeth. "Static and dynamic analysis of partially wrinkled membrane structures". In: *Collection of Technical Papers - AIAA/ASME/ASCE/AHS/ASC Structures, Structural Dynamics and Materials Conference* 4 (2000), pp. 158–171. DOI: 10.2514/6.2000-1810.

[53] F. Liu, F. Xu, and C. Fu. "Orientable wrinkles in stretched orthotropic films". In: *Extreme Mechanics Letters* 33 (2019), p. 100579. DOI: 10.1016/j.eml.2019.100579.

[54] M. Taylor et al. "Finite elastic wrinkling deformations of incompressible fiber-reinforced plates". In: *International Journal of Engineering Science* 144 (2019), p. 103138. DOI: 10.1016/j.ijengsci.2019.103138.

[55] L. Pocivavsek et al. "Stress and fold localization in thin elastic membranes". In: *Science* (2008). DOI: 10.1126/science.1154069.

[56] E. Jambon-Puillet, D. Vella, and S. Protière. "The compression of a heavy floating elastic film". In: *Soft Matter* 12.46 (Nov. 2016), pp. 9289–9296. DOI: 10.1039/C6SM00945J.

[57] E. Cerda, K. Ravi-Chandar, and L. Mahadevan. "Wrinkling of an elastic sheet under tension". In: *Nature* 419.6907 (2002), pp. 579–580. DOI: 10.1038/419579b.

[58] E. Cerda and L. Mahadevan. "Geometry and Physics of Wrinkling". In: *Physical Review Letters* (2003). DOI: 10.1103/PhysRevLett.90.074302.

[59] R. K. Miller et al. "Finite element analysis of partly wrinkled membranes". In: *Computers and Structures* 20.1-3 (1985), pp. 631–639. DOI: 10.1016/0045-7949(85)90111-7.

[60] D. G. Roddeman et al. "The Wrinkling of Thin Membranes: Part I—Theory". In: *Journal of Applied Mechanics* 54.4 (Dec. 1987), pp. 884–887. DOI: 10.1115/1.3173133.

[61] S. Kang and S. Im. "Finite element analysis of dynamic response of wrinkling membranes". In: *Computer Methods in Applied Mechanics and Engineering* 173.1 (1999), pp. 227–240. DOI: 10.1016/S0045-7825(98)00271-0.

[62] X. Wang et al. "Numerical analysis of wrinkle-influencing factors of thin membranes". In: *International Journal of Solids and Structures* 97_98 (2016), pp. 458–474. DOI: 10.1016/j.ijsolstr.2016.07.004.

[63] Y. Wong, S. Pellegrino, and K. Park. "Prediction of winkle amplitudes in square solar sails". In: *44th AIAA/ASME/ASCE/AHS/ASC Structures, Structural Dynamics, and Materials Conference*. 2003, p. 1982.

[64] Y. W. Wong and S. Pellegrino. "Computation of wrinkle amplitudes in thin membrane". In: *43rd AIAA/ASME/ASCE/AHS/ASC Structures, Structural Dynamics, and Materials Conference*. 2002, p. 1369.

[65] K. Nakashino, A. Nordmark, and A. Eriksson. "Geometrically nonlinear isogeometric analysis of a partly wrinkled membrane structure". In: *Computers and Structures* 239 (2020), p. 106302. DOI: 10.1016/j.compstruc.2020.106302.

[66] T. Iwasa, M. C. Natori, and K. Higuchi. "Evaluation of Tension Field Theory for Wrinkling Analysis With Respect to the Post-Buckling Study ". In: *Journal of Applied Mechanics* 71.4 (Sept. 2004), pp. 532–540. DOI: 10.1115/1.1767171.

[67] Y. W. Wong and S. Pellegrino. "Wrinkled membranes part III: Numerical simulations". In: *Journal of Mechanics of Materials and Structures* 1.1 (2006), pp. 63–95. DOI: 10.2140/jomms.2006.1.63.

[68]   T. J. Healey, Q. Li, and R. B. Cheng. "Wrinkling Behavior of Highly Stretched Rectangular Elastic Films via Parametric Global Bifurcation". In: *Journal of Nonlinear Science* 23.5 (2013), pp. 777–805. DOI: 10.1007/s00332-013-9168-3.

[69]   R. Bouzidi and Y. Lecieux. "Experimental analysis on membrane wrinkling under biaxial load - Comparison with bifurcation analysis". In: *International Journal of Solids and Structures* 47.18-19 (2010), pp. 2459–2475. DOI: 10.1016/j.ijsolstr.2010.05.005.

[70]   M. Taylor, K. Bertoldi, and D. J. Steigmann. "Spatial resolution of wrinkle patterns in thin elastic sheets at finite strain". In: *Journal of the Mechanics and Physics of Solids* 62.1 (2014), pp. 163–180. DOI: 10.1016/j.jmps.2013.09.024.

[71]   A. Panaitescu et al. "Birth and decay of tensional wrinkles in hyperelastic sheets". In: *Physical Review E* (2019). DOI: 10.1103/PhysRevE.100.053003.

[72]   E. Lavaerts. "Framework to research and design wrinkle free very large flexible offshore solar platforms by adding permeability". MA thesis. Delft University of Technology, 2020.

[73]   ASME. "Vessels of Noncircular Cross Section". In: *American Society of Mechanical Engineers Boiler and Pressure Vessel Code*. New York, New York: ASME Publications, 1986. Chap. Section VIII, Division 1, Appendix 13, pp. 385–430.

[74]   W. C Young and R. G Budynas. *Roark's Formulas for Stress and Strain*. New York, NY: McGraw-Hill, 2002. DOI: 10.1016/B978-0-444-41899-9.50020-3.

[75]   M. Taffetani and D. Vella. "Regimes of wrinkling in pressurized elastic shells". In: *Philosophical Transactions of the Royal Society A: Mathematical, Physical and Engineering Sciences* 375.2093 (2017), p. 20160330. DOI: 10.1098/rsta.2016.0330.

[76]   Dassault Systemes Simulia. "ABAQUS Documentation". In: (2017). URL: https://abaqus-docs.mit.edu/2017/English/SIMACAEEXCRefMap/simaexc-c-docproc.htm (visited on 09/30/2021).

[77]   M.J. Moran et al. *Fundamentals of Engineering Thermodynamics, 8th Edition*. Hoboken, NJ: Wiley, 2014.

[78]   C.M. Wang, J.N. Reddy, and K.H. Lee. *Shear Deformable Beams and Plates : Relationships with Classical Solutions*. Amsterdam: Elsevier Science & Technology, 2000.

[79]   J. N. Reddy. *Theory and Analysis of Elastic Plates and Shells*. 2nd. Boca Raton, FL: Taylor & Francis Group, 2007.

[80]   S.P. Timoshenko. "LXVI. On the correction for shear of the differential equation for transverse vibrations of prismatic bars". In: *The London, Edinburgh, and Dublin Philosophical Magazine and Journal of Science* 41.245 (1921), pp. 744–746. DOI: 10.1080/14786442108636264.

[81]   M. M. Shokrieh and S. M.Kamali Shahri. *Modeling residual stresses in composite materials*. Woodhead Publishing Limited, 2014, pp. 173–193. DOI: 10.1533/9780857098597.1.173.

[82]   I. M. Daniel and O. Ishai. *Engineering Mechanics of Composite Materials*. 2nd ed. New York, NY: Oxford University Press, 2006.

[83]   A. Liew, L. Gardner, and P. Block. "Moment-Curvature-Thrust Relationships for Beam-Columns". In: *Structures* 11 (2017), pp. 146–154. DOI: 10.1016/j.istruc.2017.05.005.

[84]   A. M. Ibrahim. "Linear And Nonlinear Flexural Stiffness Models For Concrete Walls In High-rise Building". PhD thesis. British Colombia, 2000.

[85]   X. Wang et al. "Effective bending modulus of carbon nanotubes with rippling deformation". In: *International Journal of Solids and Structures* 41.22-23 (2004), pp. 6429–6439. DOI: 10.1016/j.ijsolstr.2004.04.038.

[86]   X. Wang, X. Y. Wang, and J. Xiao. "A non-linear analysis of the bending modulus of carbon nanotubes with rippling deformations". In: *Composite Structures* 69.3 (2005), pp. 315–321. DOI: 10.1016/j.compstruct.2004.07.009.

[87] C. Wielgosz and J. C. Thomas. "Deflections of inflatable fabric panels at high pressure". In: *Thin-Walled Structures* 40.6 (2002), pp. 523–536. DOI: 10.1016/S0263-8231(02)00010-1.

[88] W. G. Davids. "Finite-element analysis of tubular fabric beams including pressure effects and local fabric wrinkling". In: *Finite Elements in Analysis and Design* 44.1 (2007), pp. 24–33. DOI: 10.1016/j.finel.2007.08.002.

[89] Y. Lecieux and R. Bouzidi. "Experimental analysis on membrane wrinkling under biaxial load – Comparison with bifurcation analysis". In: *International Journal of Solids and Structures* 47.18 (2010), pp. 2459–2475. DOI: 10.1016/j.ijsolstr.2010.05.005.

[90] Qingdu Li and Timothy J. Healey. "Stability boundaries for wrinkling in highly stretched elastic sheets". In: *Journal of the Mechanics and Physics of Solids* 97 (2016), pp. 260–274. DOI: 10.1016/j.jmps.2015.12.001.

[91] D. P. Flanagan and T. Belytschko. "A uniform strain hexahedron and quadrilateral with orthogonal hourglass control". In: *International Journal for Numerical Methods in Engineering* 17.5 (1981), pp. 679–706. DOI: 10.1002/nme.1620170504.

[92] R. C. Averill and J. N. Reddy. "Behaviour of plate elements based on the first-order shear deformation theory". In: *Engineering Computations* 7.1 (Jan. 1990), pp. 57–74. DOI: 10.1108/eb023794.

[93] King H. Yang. "Chapter 8 - Modal and Transient Dynamic Analysis". In: *Basic Finite Element Method as Applied to Injury Biomechanics*. Ed. by K. H. Yang. Academic Press, 2018, pp. 309–382. DOI: 10.1016/B978-0-12-809831-8.00008-8.

[94] T. Belytschko. "A survey of numerical methods and computer programs for dynamic structural analysis". In: *Nuclear Engineering and Design* 37.1 (1976), pp. 23–34. DOI: 10.1016/0029-5493(76)90050-9.

[95] H. D. Hibbitt and B. I. Karlsson. "Analysis of pipe whip (EPRI-NP–1208)." In: (Nov. 1979). DOI: 10.2172/5713659.

[96] H. M. Hilber, T. J. R. Hughes, and R. L. Taylor. "Improved numerical dissipation for time integration algorithms in structural dynamics". In: *Earthquake Engineering & Structural Dynamics* 5.3 (1977), pp. 283–292. DOI: 10.1002/eqe.4290050306.

[97] H. M. Hilber and T. J. R. Hughes. "Collocation, dissipation and [overshoot] for time integration schemes in structural dynamics". In: *Earthquake Engineering & Structural Dynamics* 6.1 (1978), pp. 99–117. DOI: 10.1002/eqe.4290060111.

[98] ASTM D 3039/D 3039M − $00^{\epsilon 1}$. *Standard Test Method for Tensile Properties of Polymer Matrix Composite Materials*. Standard. West Conshohocken, PA: ASTM International, Dec. 2002.

[99] ASTM. *Standard Test Method for In-Plane Shear Response of Polymer Matrix Composite Materials by Tensile Test of a +/- 45° Laminate*. Tech. rep. West Conshohocken, PA: ASTM International, 2017.

[100] P. Beccarelli. *Biaxial Testing for Fabrics and Foils Optimizing Devices and Procedures*. 1st ed. Cham: Springer International Publishing AG Switzerland, 2015.

[101] A. W. Zaal. "Feasibility evaluation of a non-destructive estimation of material properties of FRC structures using ultrasonic guided waves". MSc. Delft University of Technology, 2021.

[102] The SciPy community. *scipy.signal.savgol_filter*. URL: https://docs.scipy.org/doc/scipy/reference/generated/scipy.signal.savgol_filter.html (visited on 09/21/2021).

[103] A. Savitzky and M. J. E. Golay. "Smoothing and Differentiation of Data by Simplified Least Squares Procedures." In: *Analytical Chemistry* 36.8 (1964), pp. 1627–1639. DOI: 10.1021/ac60214a047.

[104] Y. Yao et al. "Tensile Behaviors of Basalt, Carbon, Glass, and Aramid Fabrics under Various Strain Rates". In: *Journal of Materials in Civil Engineering* 28 (2016). DOI: `10.1061/(asce)mt.1943-5533.0001587`.

[105] ASTM. *Standard Test Method for Tensile Properties of Plastics*. Tech. rep. West Conshohocken, PA: ASTM international, 2006.

[106] "Effect of material and stitching on tensile properties of woven fabrics". In: *IOP Conference Series: Materials Science and Engineering* 414.1 (2018). DOI: `10.1088/1757-899X/414/1/012049`.

[107] G. Chagnon et al. "Hyperelasticity Modeling for Incompressible Passive Biological Tissues". In: *Biomechanics of Living Organs* (2017), pp. 3–30. DOI: `10.1016/B978-0-12-804009-6.00001-8`.

[108] H. M. Verhelst. "Modelling the Wrinkling Behaviour of Large Floating Thin Structures: An Application of Isogeometric Structural Analysis and Arc-Length Methods". MA thesis. Delft University of Technology, 2020.

[109] Y. Başar and D. Weichert. *Nonlinear continuum mechanics of solids: fundamental mathematical and physical concepts*. 1st ed. Berlin: Springer, 2000. DOI: `10.1007/978-3-662-04299-1`.

[110] R. S. Rivlin. "Large Elastic Deformations of Isotropic Materials. I. Fundamental Concepts". In: *Philosophical Transactions of the Royal Society of London. Series A, Mathematical and Physical Sciences* 240.822 (1948), pp. 459–490.

[111] M. Mooney. "A Theory of Large Elastic Deformations". In: *Journal of Applied Physics* 11 (1940), pp. 582–592.

[112] R.W. Ogden. *Non-Linear Elastic Deformations*. Mineola, New York: Dover Publications, 2013.

[113] L. D. Peel. "Response of fiber-reinforced elastomers under simple tension". PhD thesis. Brigham Young University, 1998.

[114] Y. C. Fung, K. Fronek, and P. Patitucci. "Pseudoelasticity of arteries and the choice of its mathematical expression". In: *American Journal of Physiology - Heart and Circulatory Physiology* 6.5 (1979). DOI: `10.1152/ajpheart.1979.237.5.h620`.

[115] M. S. Sirry et al. "Identification of orthotropic material parameters for acute, necrotic, fibrotic and remodelling myocardial infarcts in the rat". In: *bioRxiv* (2019). DOI: `10.1101/754754`.

[116] G. A. Holzapfel, T. C. Gasser, and R. W. Ogden. "A new constitutive framework for arterial wall mechanics and a comparative study of material models". In: *Journal of Elasticity* 61.1-3 (2000), pp. 1–48. DOI: `10.1023/A:1010835316564`.

[117] T. C. Gasser, R. W. Ogden, and G. A. Holzapfel. "Hyperelastic modelling of arterial layers with distributed collagen fibre orientations". In: *Journal of the Royal Society Interface* 3.6 (2006), pp. 15–35. DOI: `10.1098/rsif.2005.0073`.

[118] J. Bergström. "5 - Elasticity/Hyperelasticity". In: *Mechanics of Solid Polymers*. Ed. by J. Bergström. William Andrew Publishing, 2015, pp. 209–307. DOI: `10.1016/B978-0-323-31150-2.00005-4`.

[119] C.M Roland. "Chapter 6 - Rheological Behavior and Processing of Unvulcanized Rubber". In: *The Science and Technology of Rubber (Fourth Edition)*. Ed. by J. E. Mark, B. Erman, and C. M. Roland. Fourth Edition. Boston: Academic Press, 2013, pp. 285–336. DOI: `10.1016/B978-0-12-394584-6.00006-6`.

[120] Z. Hou, R. J. Okamoto, and P. V. Bayly. "Shear Wave Propagation and Estimation of Material Parameters in a Nonlinear, Fibrous Material". In: *Journal of Biomechanical Engineering* 142.5 (2020), pp. 1–10. DOI: `10.1115/1.4044504`.

[121] The SciPy community. *scipy.optimize.least_squares*. URL: https://docs.scipy.org/doc/scipy/reference/generated/scipy.optimize.least_squares.html (visited on 09/21/2021).

[122] J. Chen, W. Chen, and D. Zhang. "Experimental study on uniaxial and biaxial tensile properties of coated fabric for airship envelopes". In: *Journal of Reinforced Plastics and Composites* 33.7 (2014), pp. 630–647. DOI: 10.1177/0731684413515540.

[123] C. R. Siviour and Jennifer L. Jordan. "High Strain Rate Mechanics of Polymers: A Review". In: *Journal of Dynamic Behavior of Materials* 2.1 (Mar. 2016), pp. 15–32. DOI: 10.1007/s40870-016-0052-8.

[124] H. T. Tramsen et al. "Inversion of friction anisotropy in a bio-inspired asymmetrically structured surface". In: *Journal of The Royal Society Interface* 15.138 (2018), p. 20170629. DOI: 10.1098/rsif.2017.0629.

[125] X. Huang et al. "Friction and wear properties of NBR/PVC composites". In: *Journal of Applied Polymer Science* 106.4 (2007), pp. 2565–2570. DOI: 10.1002/app.25316.

[126] P. Rozylo et al. "Experimental and Numerical Study of the Buckling of Composite Profiles with Open Cross Section under Axial Compression". In: *Applied Composite Materials* 24 (2017), pp. 1251–1264. DOI: 10.1007/s10443-017-9583-y.

[127] J. Toutouh. "Metaheuristics for Optimal Transfer of P2P Information in Vehicular Networks". MSc. Massachusetts Institute of Technology, June 2010. DOI: 10.13140/RG.2.1.5011.6969.

[128] P. C. Yang, C. H. Norris, and Y. Stavsky. "Elastic wave propagation in heterogeneous plates". en. In: *Int. J. Solids Struct.* 2.4 (Oct. 1966), pp. 665–684.

[129] J. M. Whitney and N. J. Pagano. "Shear deformation in heterogeneous anisotropic plates". In: *J. Appl. Mech.* 37.4 (Dec. 1970), pp. 1031–1036.

[130] J. N. Reddy. "A simple higher-order theory for laminated composite plates". In: *J. Appl. Mech.* 51.4 (Dec. 1984).

[131] P. Xu and P. R. Wellens. "Fully nonlinear hydroelastic modeling and analytic solution of large-scale floating photovoltaics in waves". In: *Journal of Fluids and Structures* 109 (2022). DOI: 10.1016/j.jfluidstructs.2021.103446.

[132] M. Padilha Campos Lopes et al. "Technical potential of floating photovoltaic systems on artificial water bodies in Brazil". In: *Renewable Energy* 181 (2022), pp. 1023–1033. DOI: 10.1016/j.renene.2021.09.104.

[133] The SciPy community. *scipy.optimize.newton*. URL: https://docs.scipy.org/doc/scipy/reference/generated/scipy.optimize.newton.html (visited on 02/24/2021).

Appendix A

Performed measurements and resulting deflection three point bending experiments

Figure A.1: A photograph of the test setup showing the gauge rods (courtesy of TNO).

Table A.1: Performed measurements three point bending test

Measurement nr.	Pressure [kPa]	Load [N]	Measurement nr.	Pressure [kPa]	Load [N]
1	7	0	21	20	0
2	7	499	22	20	1382
3	7	1088	23	20	1971
4	7	1677	24	20	2854
5	7	1971	25	20	3688
6	10	0	21	20	0
7	10	794	22	20	1382
8	10	1383	23	20	1971
9	10	1971	24	20	2854
10	10	2559	25	20	3688
11	12	0	26	10	794
12	12	1088	27	10	1382
13	12	1677	28	10	1971
14	12	2559	29	10	2559
15	12	3050	30	10	2854
16	15	0	31	10	2559
17	15	1382	32	10	1971
18	15	1971	33	10	1382
19	15	2854	34	10	794
20	15	3688			
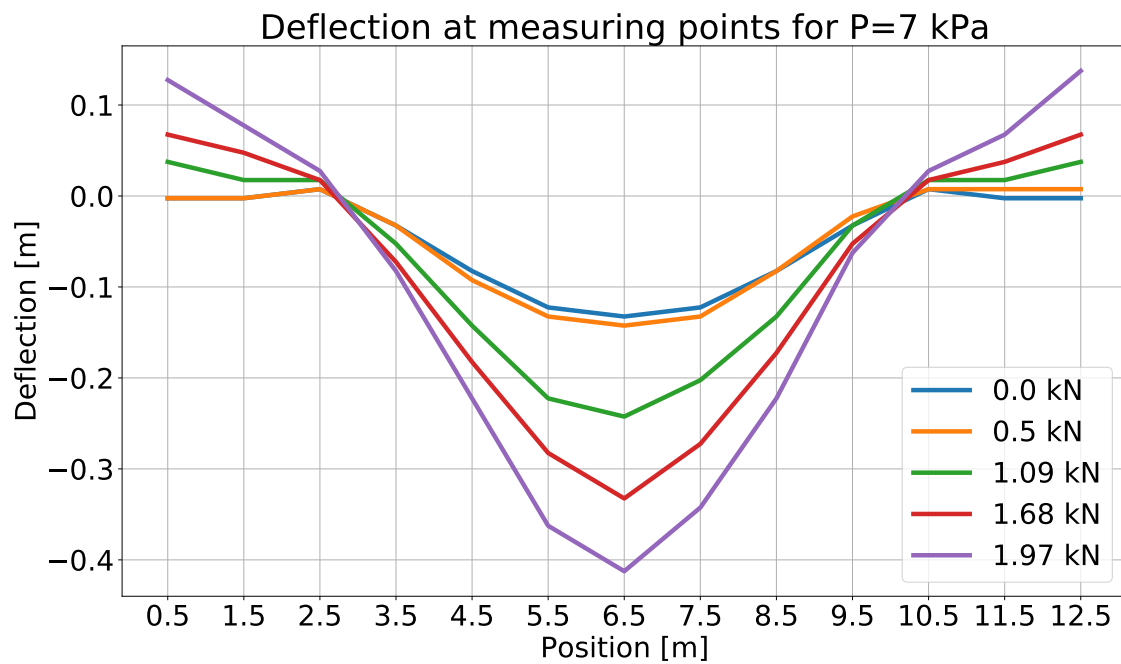
Figure A.2: Measured deflection of the three point bending test at different longitudinal coordinates for an internal air pressure of 7 kPa
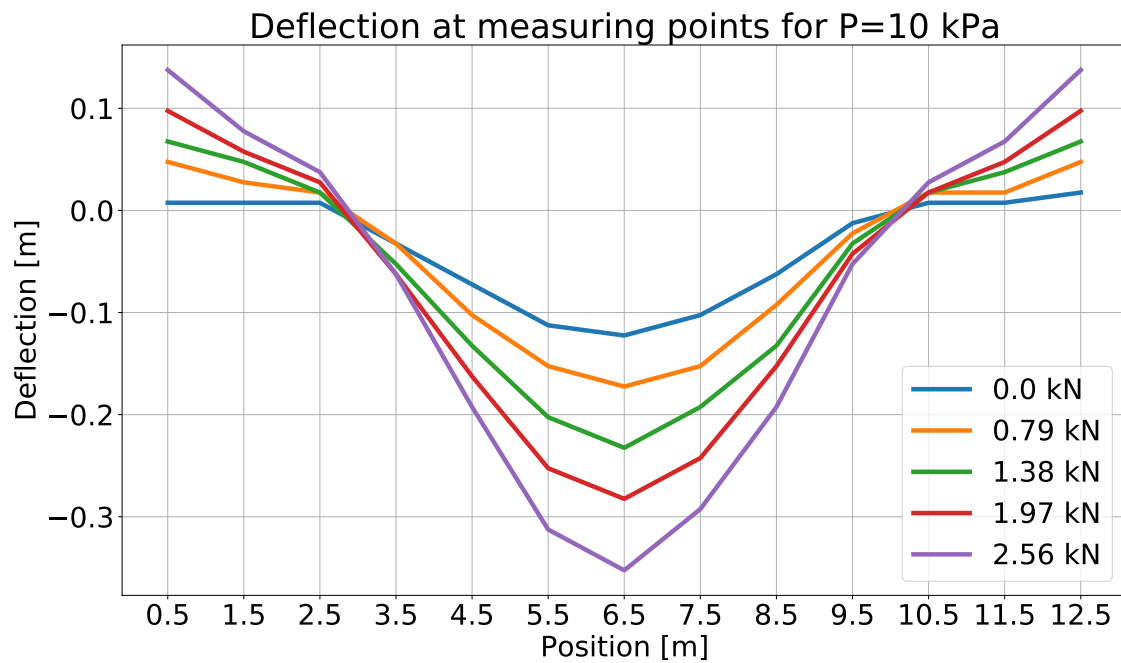
Figure A.3: Measured deflection of the three point bending test at different longitudinal coordinates for an internal air pressure of 10 kPa
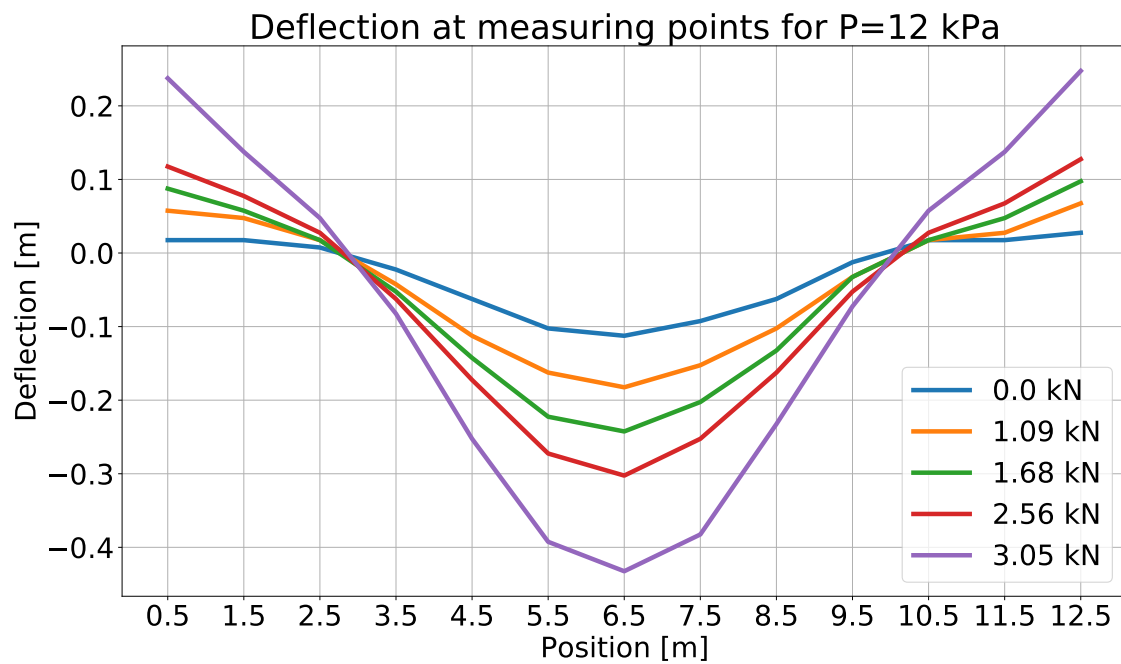
Figure A.4: Measured deflection of the three point bending test at different longitudinal coordinates for an internal air pressure of 12 kPa
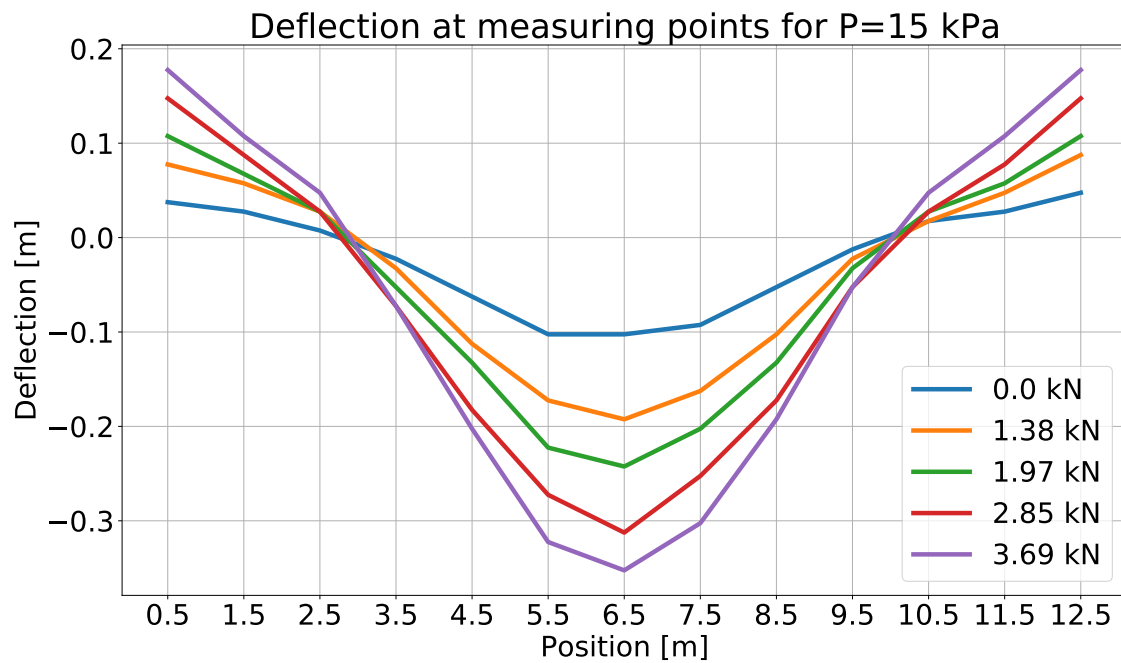
Figure A.5: Measured deflection of the three point bending test at different longitudinal coordinates for an internal air pressure of 15 kPa
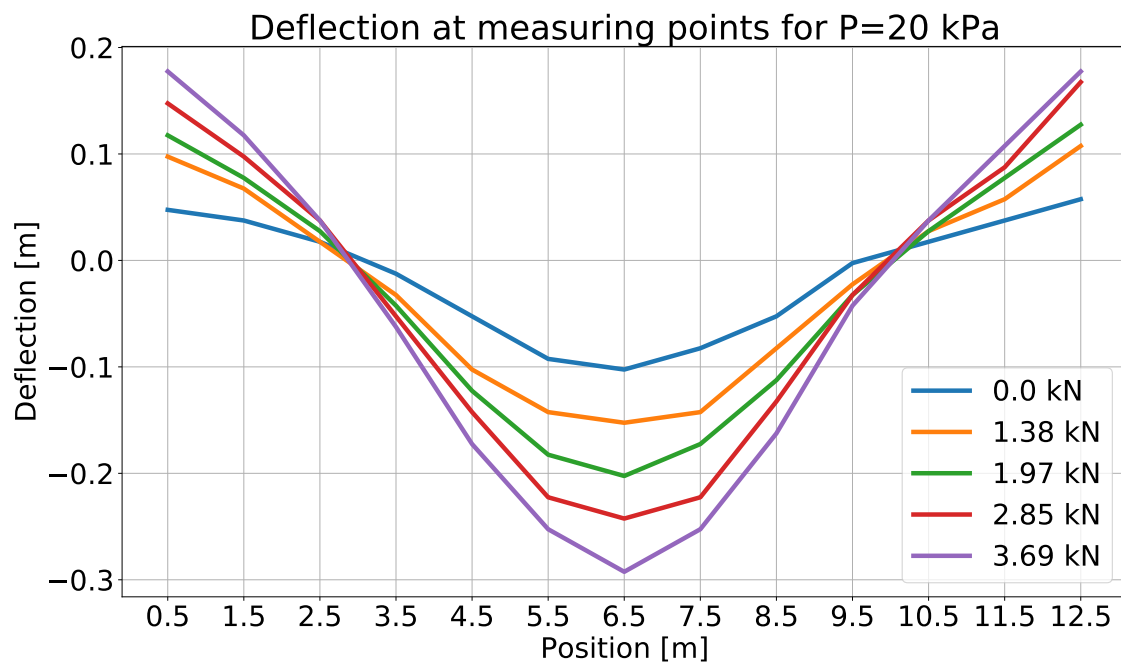
Figure A.6: Measured deflection of the three point bending test at different longitudinal coordinates for an internal air pressure of 20 kPa

Results tensile test

B.1   Measurements

Table B.1: Specimen numbers with their respective fiber direction and material.

Fiber direction [deg]	0	45	90
Face sheet	[16, 17, 18, 19, 21]	[27, 70, 71, 72, 73]	[2, 3, 4, 7, 9]
Edge	[33, 34, 36, 37, 40]	[65, 66, 67, 68, 69]	[46, 48, 50, 52, 53]
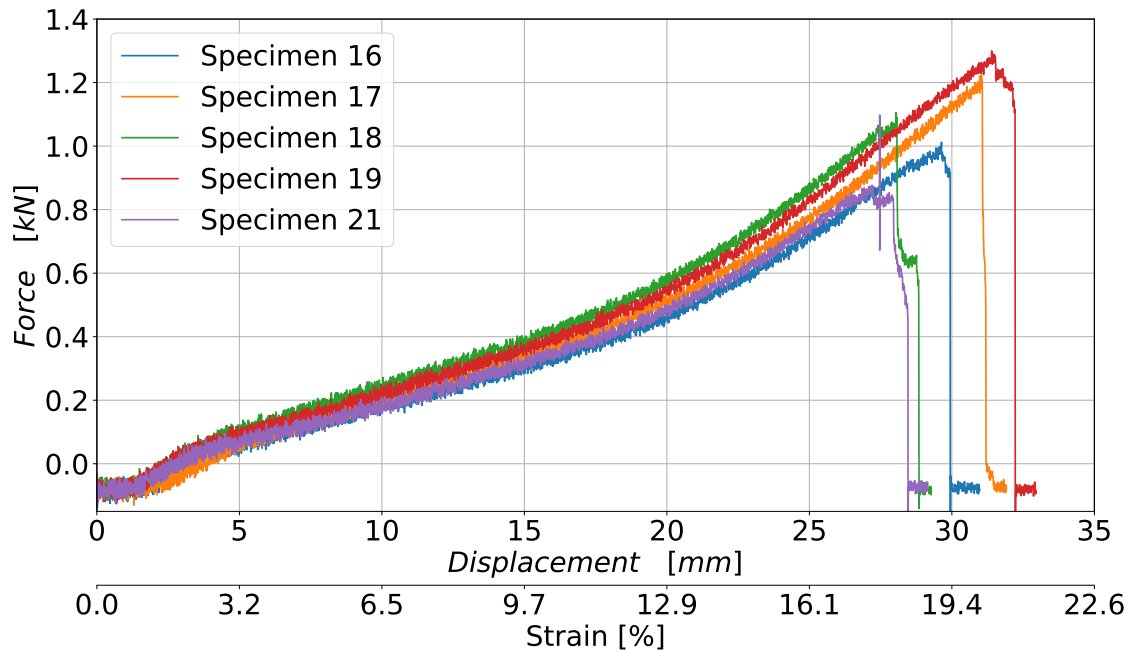
Figure B.1: Raw force-displacement results for the face sheet fabric in 0° fiber direction. The respective filtered force-displacement results are shown in figure 5.4a
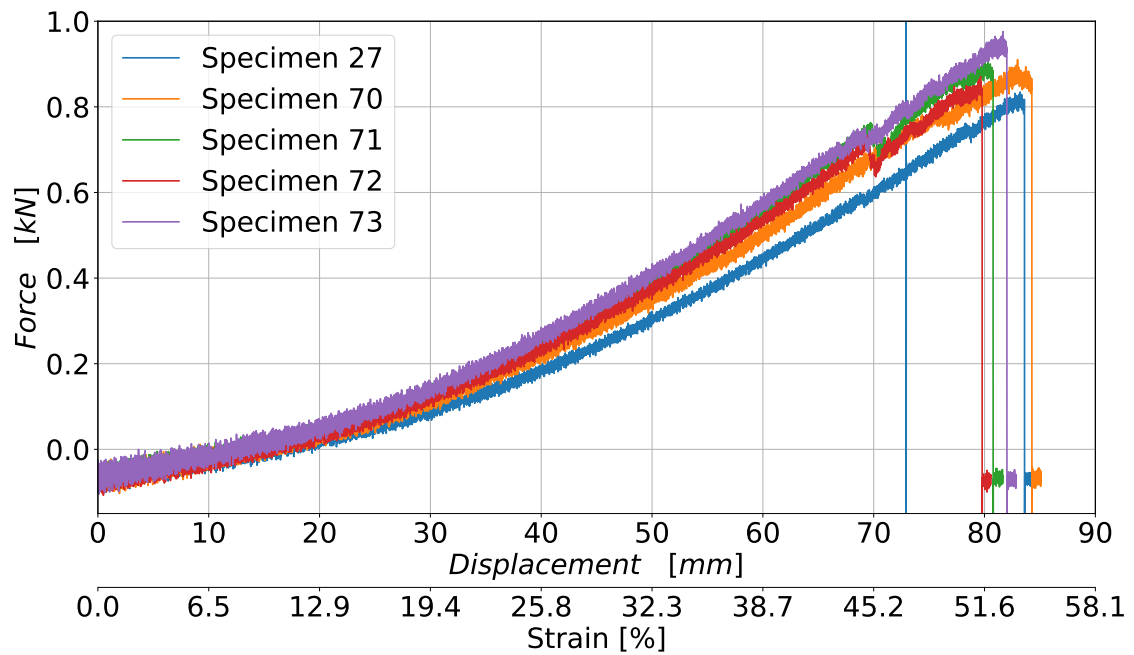
Figure B.2: Raw force-displacement results for the face sheet fabric in 45° fiber direction. The respective filtered force-displacement results are shown in figure 5.4b
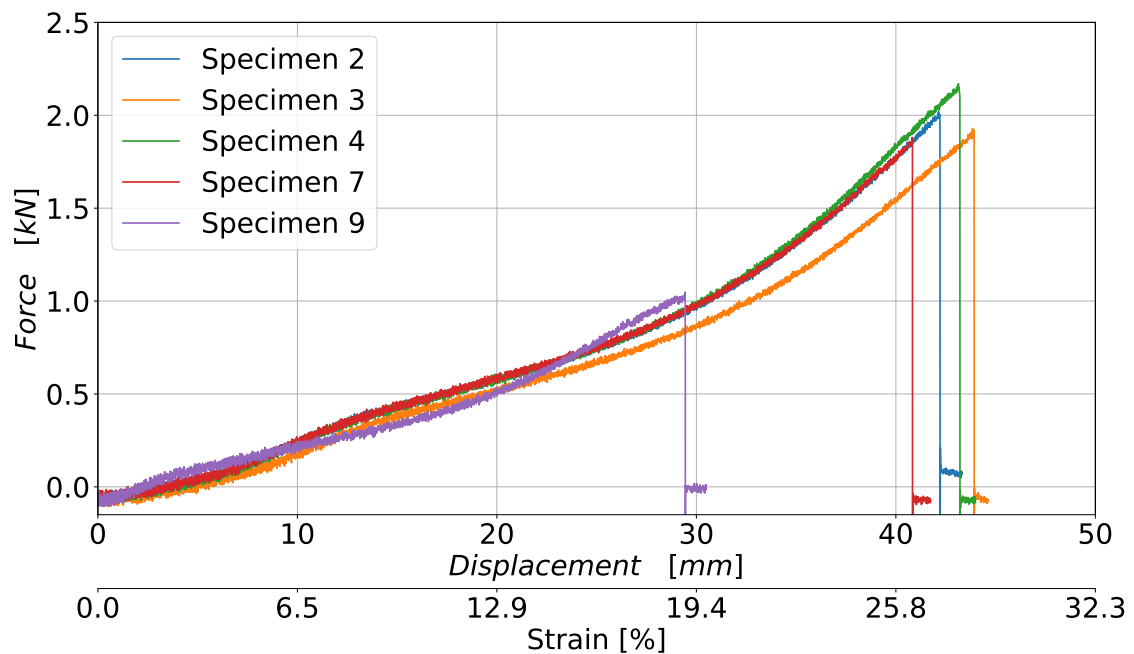
Figure B.3: Raw force-displacement results for the face sheet fabric in 90° fiber direction. The respective filtered force-displacement results are shown in figure 5.4c. Specimen 9 shows different stress-strain behaviour and is considered to an outlier.
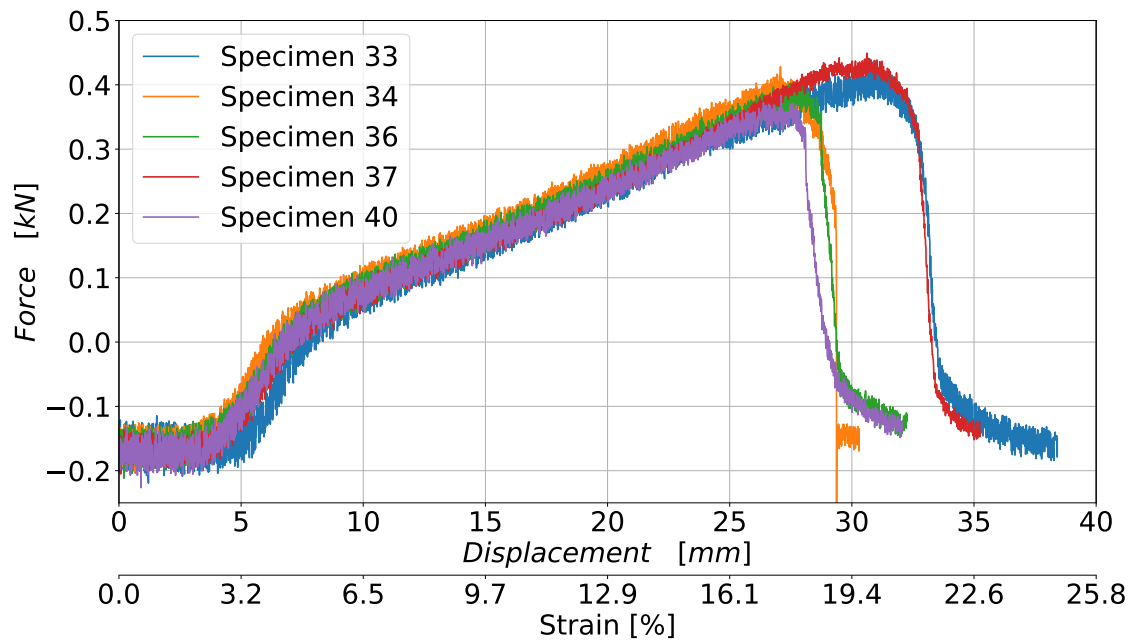
Figure B.4: Raw force-displacement results for the edge sheet fabric in 0° fiber direction. The respective filtered force-displacement results are shown in figure 5.4d
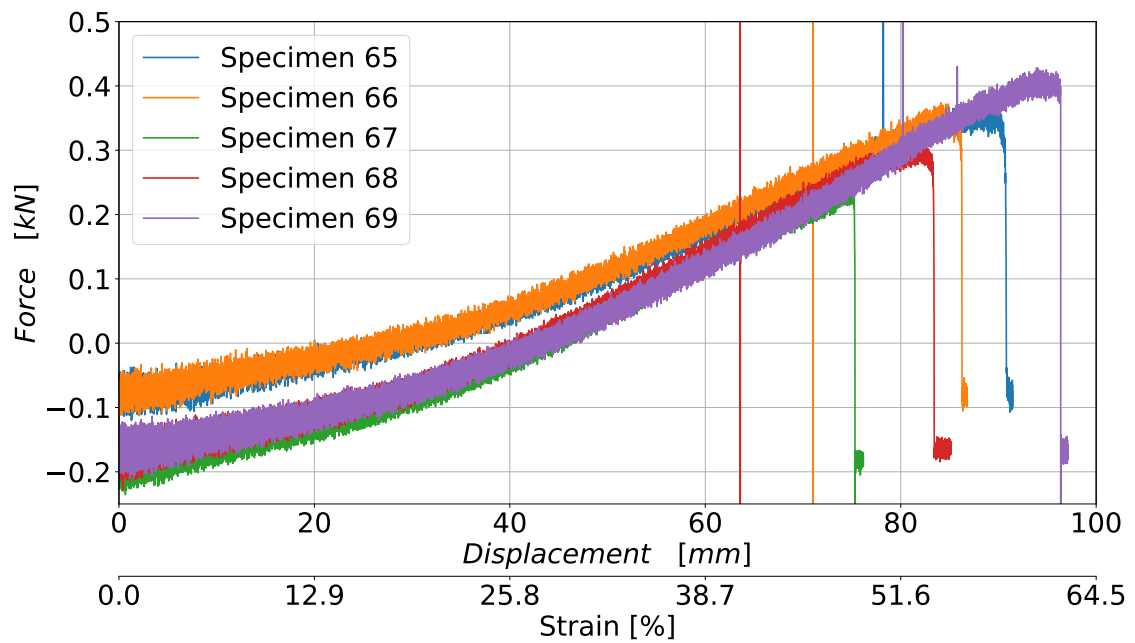
Figure B.5: Raw force-displacement results for the edge sheet fabric in 45° fiber direction. The respective filtered force-displacement results are shown in figure 5.4e
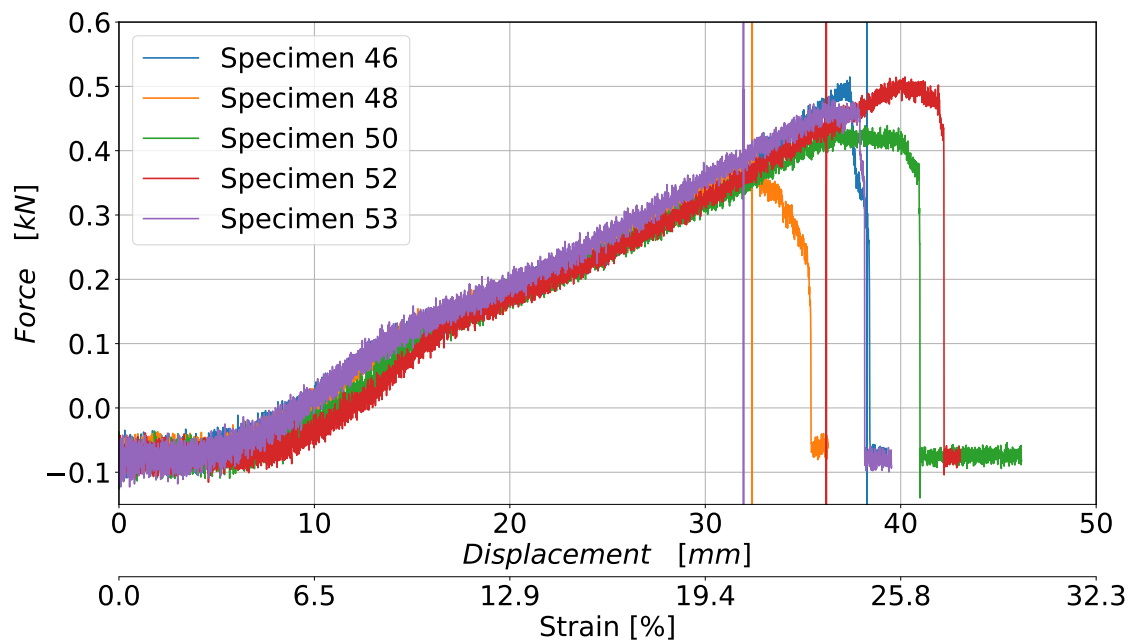
Figure B.6: Raw force-displacement results for the edge sheet fabric in 90° fiber direction. The respective filtered force-displacement results are shown in figure 5.4f

B.2 Material models

Table B.2: Fitted variables of LEO1 material model

Fabric	E_1 [MPa]	E_2 [MPa]	$\nu_{12}[-]$	G_{12} [MPa]	G_{13} [MPa]	G_{23} [MPa]
Face	202	111	0.29	12	1	1
Edge	213	105	0.29	7.5	1	1

Table B.3: Fitted variables of LEO2 material model

Fabric	E_1 [MPa]	E_2 [MPa]	$\nu_{12}[-]$	G_{12} [MPa]	G_{13} [MPa]	G_{23} [MPa]
Face	300	144	0.29	11.6	1	1
Edge	390	129	0.29	8.4	1	1

Table B.4: Fitted variables of HGO model

Fabric	Ply nr. [-]	Fiber direction [deg]	C_{10} [Pa]	D [Pa]	κ [-]	k_1 [MPa]	k_2 [Pa]
Face	1	0	10	0	0	99.6	268
	2	90	10	0	0	51.1	133
Edge	1	0	10	0	0	104.9	265
	2	90	10	0	0	44	161.2

Table B.5: Fitted variables of FO model

Fabric	b_{1111} [Pa]	b_{1122} [Pa]	b_{2222} [Pa]	b_{1212} [Pa]	c	D
Face	703	-124	330	31	319651	0
Edge	628.91	-115.487	240.667	19	388964	0

Analytical Wrinkling Onset Load

The wrinkling onset load is determined, which gives an estimation from which load the bending stiffness becomes non-linear. Drop-stitch panels can be considered as a pretensioned structure. Cavallaro et al [43] determined the wrinkling onset moment as mentioned in section 2.3, which did not include the mass. For low pressurised drop-stitch panels, it is expected that the bending stiffness decreases and the initial deflection resulting from the gravity becomes more significant. Cavallaro et al [43] found good correlation between the experimental and analytical wrinkling onset load. To determine the wrinkling onset load of a three point bending test, the wrinkling onset moment should be equal to the internal bending moment created by the mass m and wrinkling onset load F_{onset}:

$$M_{onset} = M_{int}\left(m, F_{onset}\right) \tag{C.1}$$

The wrinkling onset moment M_{onset} is the moment needed to nullify the pretension created by the internal air pressure. The longitudinal tension load in the face sheets is determined by multiplying the internal air pressure with the transverse projected area, equation C.2 with P is the pressure, B the width and H the thickness of the drop-stitch panel. Dividing F_x by the circumferential area, results in the longitudinal stress, equation C.3 with t_{face} is the thickness of the face sheets. The section modulus is determined by assuming the face sheet is very thin, so that the moment of inertia of the edges is $I_{yy,edge} \approx \pi \left(\frac{H}{2}\right)^3 t_{face}$ and the upper and lower facesheets $I_{yy,face} \approx 2(B - H)t_{face}\left(\frac{H}{2}\right)^2$. Dividing the moment of inertia with the outer fiber distance results in the section modulus, equation C.4.

$$F_x = P\left(\left(B - H\right)H + \frac{\pi H^2}{4}\right) \tag{C.2}$$

$$\sigma_x = \frac{F_x}{t_{face}\left(2\left(B - H\right) + \pi H\right)} = P\frac{H}{4}\frac{\left(\left(4B - 4H\right) + \pi H\right)}{t_{face}\left(2\left(B - H\right) + \pi H\right)} \tag{C.3}$$

$$W = \frac{H t_{face}}{4}\left(\left(4B - 4H\right) + \pi H\right) \tag{C.4}$$

The shear force, V, as function of x for the three point bending test load case of the experiments as described in chapter 4 is shown in equation C.5 for $0 < x < \frac{1}{2}L$. Since the load condition is symmetric, only the distribution within the range $0 < x < \frac{1}{2}L$ is established. The result moment and shear force diagram is shown in figure C.2.

$$V_{int}(x) = \begin{cases} -\dfrac{mg}{L}x & \forall \quad x \in [0, L_{sup}] \\ -\dfrac{mg}{L}x + \dfrac{mg + F_{mid}}{2} & \forall \quad x \in [L_{sup}, \frac{L}{2}] \end{cases} \tag{C.5}$$

$$M_{int}(x) = \int V_{int}(x)dx = \begin{cases} -\dfrac{mg}{2L}x^2 & \forall \quad x \in [0, L_{sup}] \\ -\dfrac{mg}{2L}x^2 + \dfrac{mg + F_{mid}}{2}(x - L_{sup}) & \forall \quad x \in [L_{sup}, \frac{L}{2}] \end{cases} \tag{C.6}$$

Solving the maximum mid span load F_{mid} at which the internal bending moment is equal to the wrinkling onset bending moment, equation C.1, results in the wrinkling onset load F_{onset}. Figure C.1 shows the maximum applied during the experiments in chapter 4 for different air pressure and the analytical wrinkling onset load. It shows a linear relation between the wrinkling onset and internal air pressure.
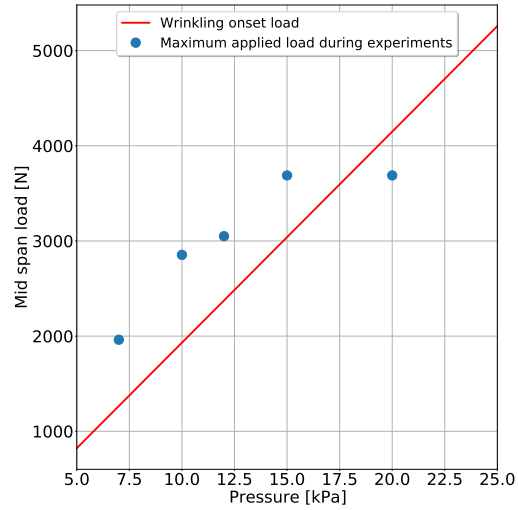
Figure C.1: Experimental maximum load and the wrinkling onset load. Note that the maximum applied load of the 20 kPa is not close the failure load as discussed in chapter 4. For the other measurement points, the maximum applied load is close to the failure load.
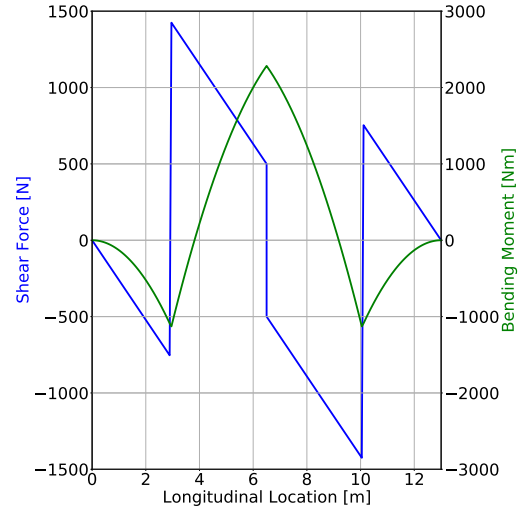
Figure C.2: Internal bending moment and shear force diagram for the three point bending test performed in chapter 4 with a midspan load of 1 kN.

Appendix D

Stress in xx-direction for 20 and 30 mm yarn spacing of FEA
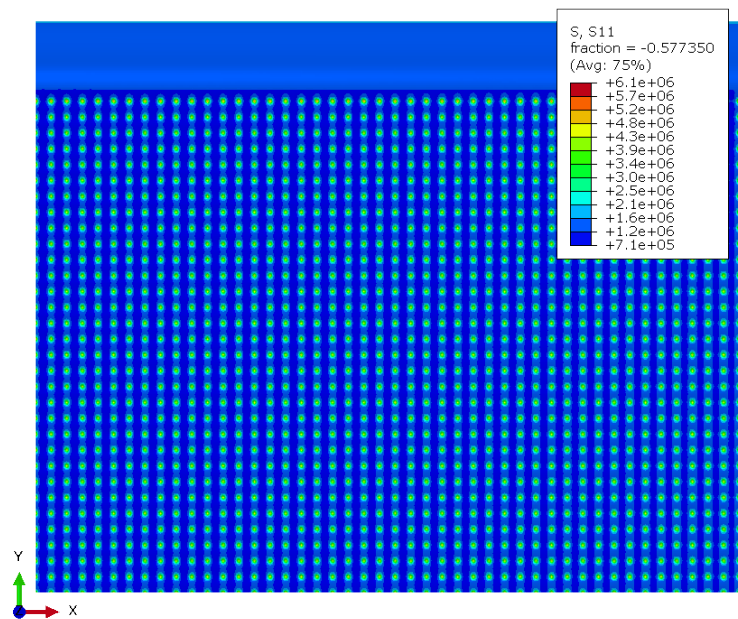
Figure D.1: Stress in xx-direction of the quarter model with a yarn spacing of 20 mm at the initial displacement (with gravity included). Note that the load beam is on the left edge as depicted in figure 6.2.
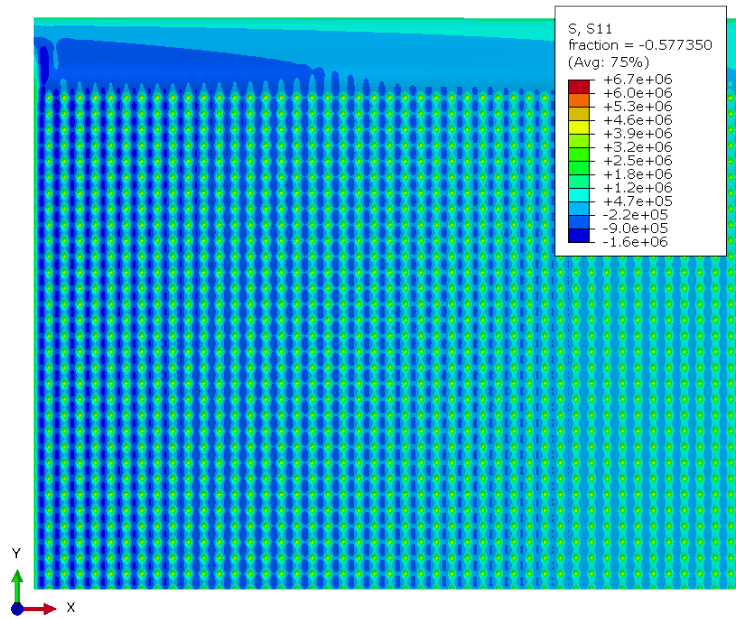
Figure D.2: Stress in xx-direction of the quarter model with a yarn spacing of 20 mm at a displacement of 0.23m. Note that the load beam is on the left edge as depicted in figure 6.2.
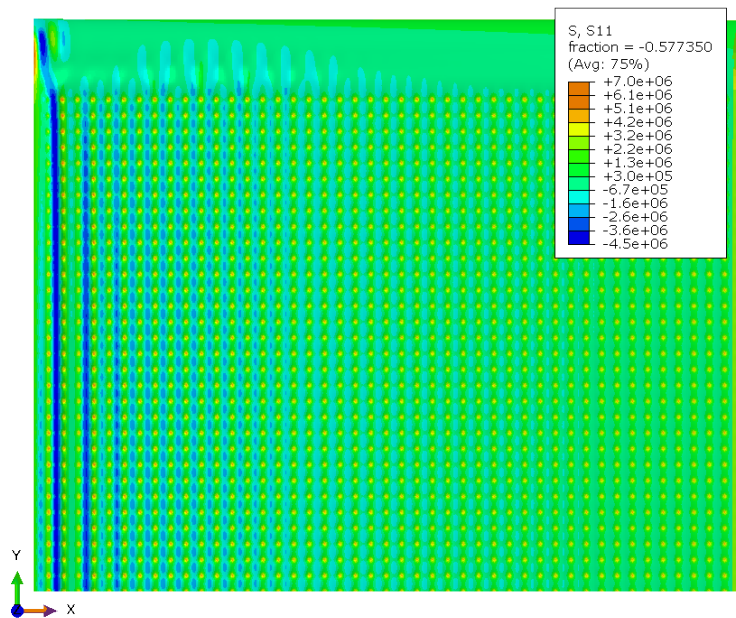
Figure D.3: Stress in xx-direction of the quarter model with a yarn spacing of 20 mm at a displacement of 0.32m. Note that the load beam is on the left edge as depicted in figure 6.2.
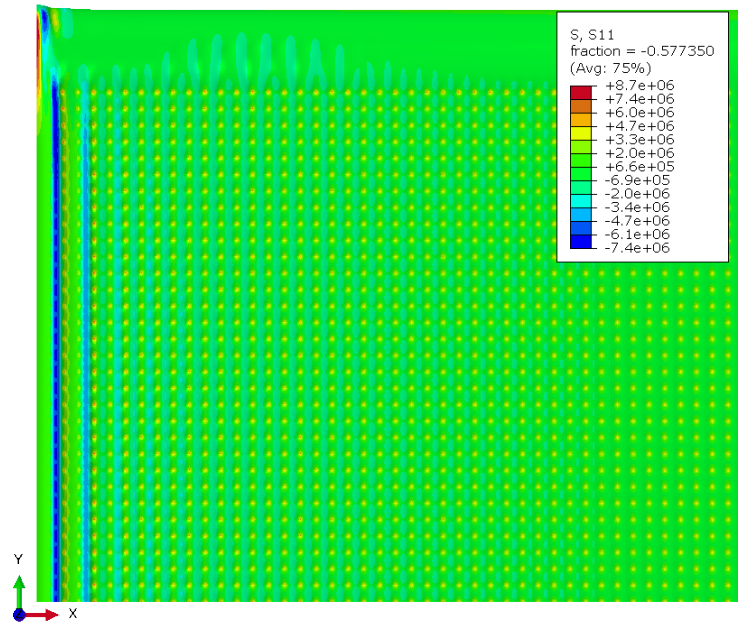
Figure D.4: Stress in xx-direction of the quarter model with a yarn spacing of 20 mm at a displacement of 0.4m. Note that the load beam is on the left edge as depicted in figure 6.2.
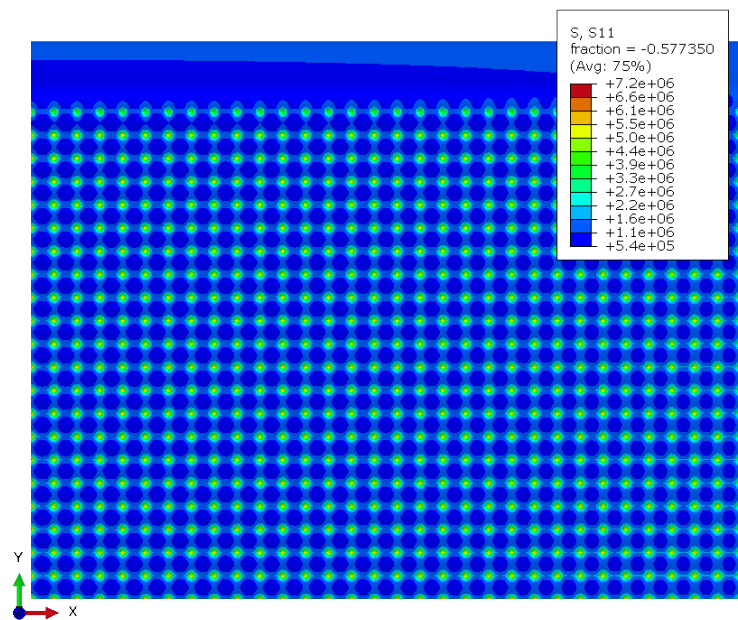
Figure D.5: Stress in xx-direction of the quarter model with a yarn spacing of 30 mm at the initial displacement (with gravity included). Note that the load beam is on the left edge as depicted in figure 6.2.
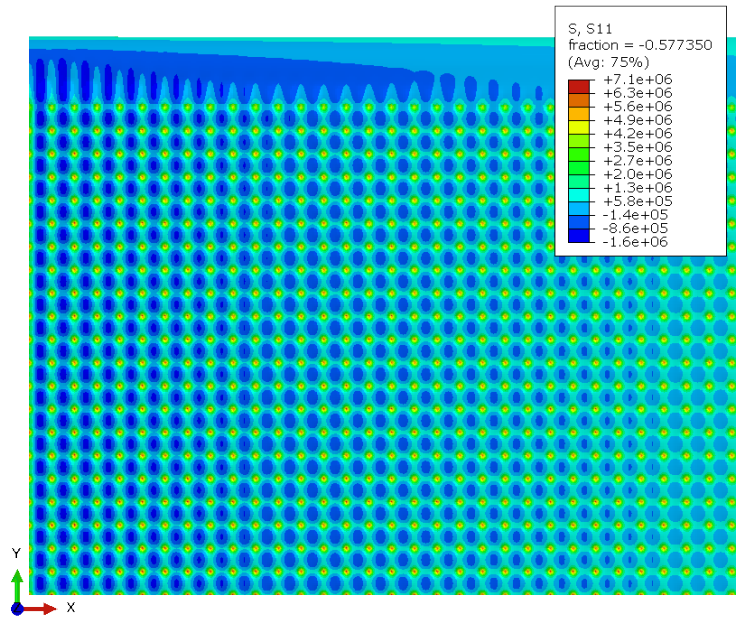
Figure D.6: Stress in xx-direction of the quarter model with a yarn spacing of 30 mm at a displacement of 0.21m. Note that the load beam is on the left edge as depicted in figure 6.2.
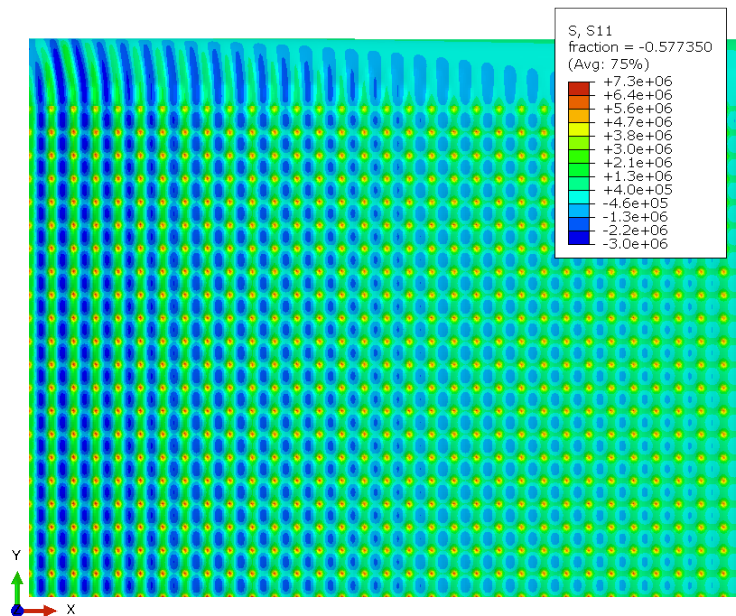
Figure D.7: Stress in xx-direction of the quarter model with a yarn spacing of 30 mm at a displacement of 0.324m. Note that the load beam is on the left edge as depicted in figure 6.2.
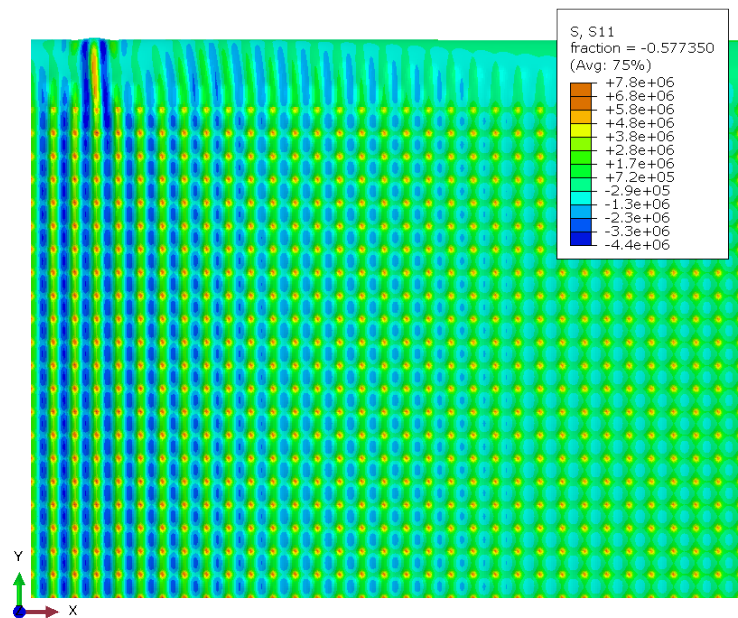
Figure D.8: Stress in xx-direction of the quarter model with a yarn spacing of 30 mm at a displacement of 0.4m. Note that the load beam is on the left edge as depicted in figure 6.2.

Appendix E

Analytical perturbation model

The initial perturbation due to the inflation is analytically derived as discussed in section 6.2.2. A one-dimensional beam has been assumed, which inflates in a circular shape as shown in figure E.1.
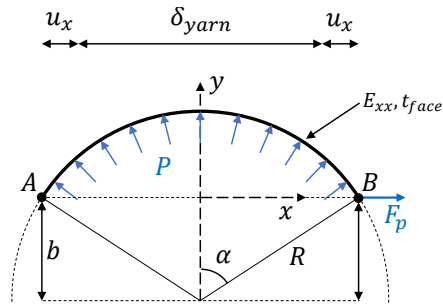
Figure E.1: A sketch of the model used to determine the perturbation analytically. It is assumed that the face sheets inflate with a circular shape that can be described with the function $y(x) = \sqrt{R^2 - x^2} - b$. R is the radius of the circle, P the internal air pressure, F_p the tension load, b the distance between the centre of the circle and chord of the circle, α the half central angle of the circle segment, E_{xx} the Young's modulus in the longitudinal direction, t_{face} the thickness of the face sheets, δ_{yarn} the yarn distance and u_x the horizontal displacement. The face sheet is hinged supported in points A and B.

An energy balance between external and internal energy is formulated as a function of the angle α and displacement u_x. The minimisation energy function is divided into four components:

$$U = U_m + U_b - U_P - U_{F_p} = 0$$

with U_m is the internal membrane strain, U_b the internal bending strain, U_P the external distributed pressure load and U_{F_p} the pretension load energy. U has been minimised by using the fact that:

$$\frac{\partial U}{\partial \alpha} = 0 \text{ and } \frac{\partial U}{\partial u_x} = 0$$

The Newton-Raphson solver of the `SciPy` Python package has been used [133]. The degrees of freedom α and u_x are bounded by the values $[0, \frac{1}{2}\pi]$ rad and $[-0.04, 0.04]$ m respectively. By solving the minimisation energy function, the initial perturbation can be determined with $w_0 = R - b$. Following the energy components are derived.

Internal membrane strain

For the internal membrane strain energy U_m, an isotropic linear elastic material model without Poisson's effect is used. U_m can be derived by:

$$U_m = E_{xx} t_{face} \int_0^L \varepsilon^2 ds = E_{xx} t_{face} \varepsilon^2 \delta_{yarn}$$

100

with ε is the strain in the face sheet and L the initial length of the face sheet is equal to δ_{yarn}. The strain in the face sheets is determined by assuming the face sheet is flat with a length equal to δ_{yarn} in the initial state and circular in the final state. This results in a change in length, which can be expressed in an analytical strain function as:

$$\varepsilon = \frac{2R\alpha - \delta_{yarn}}{\delta_{yarn}}$$

with

$$R = \frac{2u_x + \delta_{yarn}}{2\cos(\alpha)}$$

Internal bending strain

Due to the constant curvature of the face sheet over the length in the analytical model, the integration of the bending strain energy is simple. It is derived by:

$$U_b = E_{xx}I_{zz} \int_0^L \kappa^2 dl = E_{xx}I_{zz} \int_0^L \left(\frac{1}{R}\right)^2 dl$$

with κ is the curvature and I_{zz} is the moment of inertia of the face sheet, which is $I_{zz} = \frac{t^3}{12}$.

External distributed pressure load

The distributed pressure generates a deformation, which is described by the function y(x) as shown in figure E.1. This can be described as:

$$U_p = P \int_0^L y(x)dx = PA$$

with A is the area of the circle segment as shown in figure E.1. The area of the circle segment can be determined by:

$$A = 2R^2\alpha - b(\delta_{yarn} + 2u_x)$$

with

$$b = \frac{\delta_{yarn} + 2u_x}{2\tan(\alpha)}$$

External pretension load

The internal air pressure generates a pretension in the face sheets, which can be described with:

$$F_p = \frac{PH}{2}$$

with H is the height of the drop-stitch panel. Only one face sheet is considered in the analytical perturbation model, so this results in a division by two. The pretension introduces a energy component in the x-direction:

$$U_{F_p} = F_p u_x = \frac{PHu_x}{2}$$

Derivation of the pressure-bending energy ratio

The derivation of the scaling law used in section 8.1.2 is based on the methodology proposed by Pocivavsek et al [55]. It is based on an energy balance of the potential energy of a fluid U_k and internal bending energy of a membrane U_b to analyse localised folds.

$$U_b \approx \frac{B}{2} \int_0^L dl \ddot{y}^2 \sim BL(A/\lambda^2)^2$$

with B is the bending stiffness $B = E_{xx}t_{face}^3/12$, L the length of the membrane, $\ddot{y}$ the second derivative of the displacement, A the amplitude of the wrinkle and λ the length of the wrinkle. The potential energy of the fluid is different from Pocivavsek et al, since the pressure of the internal air volume is relatively constant and does not increase linearly with increasing draft as a liquid fluid. It can be described as:

$$U_p = P \int_0^L dl y \sim PAL$$

Using the inextensibility constraint of Pocivavsek et al [55], which assumes that the length of a folded membrane stays constant, the scaling of the wrinkling amplitude can be derived:

$$\Delta = \int_0^L dl \dot{y}^2 \sim L(A/\lambda)^2 \rightarrow A \sim \lambda\sqrt{\Delta/L}$$

with Δ is the compressive displacement of the membrane. In a pure bending load case, Δ scales with the height. Assuming a linear strain distribution over the height, the scaling for Δ becomes:

$$\Delta \sim H\phi$$

with H is the height of the panel and ϕ is the angle of the linear displacement distribution as discussed in section 2.5, which denotes the rotation of the cross section [78]. The scaling law for the pressure-bending energy ratio can now be derived by:

$$\frac{U_p}{U_b} \sim \frac{P\lambda^3\sqrt{L}}{E_{xx}t_{face}^3\sqrt{H}}\sqrt{\phi}$$

The non-dimensional pressure-bending energy ratio C_{bp} can now be derived. It is assumed that the length of the membrane scales with the wrinkling length, so $L \sim \lambda$. Also it is independent of the load case, so the angle ϕ is not taken into account. This results in:

$$C_{pb} = \frac{P\lambda^{3\frac{1}{2}}}{E_{xx}t_{face}^3\sqrt{H}}$$